

Distribution Agreement

In presenting this thesis or dissertation as a partial fulfillment of the requirements for an advanced degree from Emory University, I hereby grant to Emory University and its agents the non-exclusive license to archive, make accessible, and display my thesis or dissertation in whole or in part in all forms of media, now or hereafter known, including display on the world wide web. I understand that I may select some access restrictions as part of the online submission of this thesis or dissertation. I retain all ownership rights to the copyright of the thesis or dissertation. I also retain the right to use in future works (such as articles or books) all or part of this thesis or dissertation.

Signature:

Drew P. Kise

Date

Development of Microfluidic Mixing Techniques to study Enzyme Dynamics

By

Drew P. Kise

Doctor of Philosophy

Chemistry

R. Brian Dyer, Ph.D.

Advisor

James T. Kindt, Ph.D.

Committee Member

Emily Weinert, Ph.D.

Committee Member

Accepted:

Lisa A. Tedesco, Ph.D.

Dean of the James T. Laney School of Graduate Studies

Date

Development of Microfluidic Mixing Techniques to study Enzyme Dynamics

By

Drew P. Kise

B.S., University of Pittsburgh, 2010

Advisor: R. Brian Dyer, PhD

An abstract of

A dissertation submitted to the Faculty

of the James T. Laney School of Graduate Studies of Emory University

in partial fulfillment of the requirements for the degree of

Doctor of Philosophy

in Chemistry

2016

Abstract

Development of Microfluidic Mixing Techniques to study Enzyme Dynamics

By Drew P. Kise

Enzymes are biological catalysts with far-reaching implications to the sustaining of biological processes and life as we know it. However, even after many years of extensive research on enzymes, scientists still have questions as to how enzymes are able to do what they do. It is now known that dynamics, in fact, play a role ranging from molecular vibrations to large conformational changes. Therefore, technologies are needed that can be used to study the dynamic processes in enzymes. Microfluidic mixing has been continually developed over the past couple of decades to become one such technique used for enzymatic studies. In this dissertation, developments in both microfluidic mixers, the instruments utilizing the mixers, and applications to enzymatic reactions are discussed. New fabrication methods for microfluidic mixers have been created that can produce mixers in a cost-efficient manner. Also, an infrared imaging system has been developed to apply microfluidic mixing with infrared spectroscopy. Finally, the developments are applied to biological systems. The newly developed infrared imaging was used a sandwich-format microfluidic mixer to study a pH jump experiment with adenosine monophosphate, which both proved the utility of the instrument and established the fast mixing time, defining the timescale of reaction kinetics that can be viably studied. Next, fast mixing was employed to study reaction kinetics in the catalytic cycle of the enzyme dihydrofolate reductase. A common model among enzymatic studies, the hydride step of DHFR catalysis was resolved in mixing experiments by following the intrinsic emission of the cofactor, NADPH. Along with resolving the kinetics of the pH dependent hydride transfer step, a second process was also resolved that was attributed to a pH independent conformational change in DHFR to ready itself for the transfer of a hydride from NADPH to substrate, dihydrofolate. Finally, the implications and future directions of the developed technologies are then discussed.

Development of Microfluidic Mixing Techniques to study Enzyme Dynamics

By

Drew P. Kise

B.S., University of Pittsburgh, 2010

Advisor: R. Brian Dyer, PhD

A dissertation submitted to the Faculty
of the James T. Laney School of Graduate Studies of Emory University
in partial fulfillment of the requirements for the degree of
Doctor of Philosophy
in Chemistry
2016

Acknowledgements

To Casey, for giving me the support and push I needed to get over each graduate school hurdle.

To Michael and Donny, for being my daily in-lab guidance throughout this entire process.

To Rachel and Brooke, for making progress in my last year of graduate school at all possible.

And to Brian Dyer, who supported me every step of the way in not only my research, but more importantly in following my passion, even though it may have led to an unorthodox tenure as a graduate student.

Contents

Chapter 1: Introduction.....	1
Chapter 2. Microfluidic mixer design and optimization.....	10
Section 2.1 Introduction to microfluidic mixer design.....	10
Section 2.2 The 2D fast microfluidic mixer design and calibration.....	15
Section 2.3 Optimization of 2D mixer design	21
Section 2.4 Other production methods for 2D microfluidic mixers.....	26
Section 2.5 Advances in 3D capillary mixer	47
Chapter 3. Development of an infrared imaging system to follow submillisecond mixing reactions.....	52
Section 3.1 Introduction	52
Section 3.2 The sandwich-style mixer.....	53
Section 3.3 Development of Homemade Infrared Imaging System.....	58
Section 3.4 Application of infrared imaging system	67
Section 3.5 Modifications to infrared imaging system.....	81
Chapter 4: Applications of microfluidic mixing to biological systems.....	85
Section 4.1: Introduction to biological kinetics methodology from micro- to milliseconds.....	85
Section 4.2: Introduction to DHFR catalysis.....	88
Section 4.3: DHFR microfluidic mixing experiments	92
Chapter 5: Conclusions.....	105
References.....	109

Figures

Figure 1.1: Common timescales for different dynamic events occurring in enzymes.....	4
Figure 1.2: A schematic of simple parallel lamination mixers	7
Figure 2.1: Etching process to create microfluidic channels	12
Figure 2.2: Procedure to fabricate microfluidic channels out of PDMS elastomer	13
Figure 2.3: A magnified visible image of the mixer	16
Figure 2.4: Images displaying the focused laser line used to excite the Eu nanospheres for mixer calibration.	17
Figure 2.5: IR microfluidic mixer calibration data	19
Figure 2.6: Optimization of the angle at which the sheath channels meet with the sample	23
Figure 2.7: Optimization of channel diameters.....	24
Figure 2.8: 3D printed mixers.....	30
Figure 2.9: Absorbance (solid) and fluorescence (dashed) spectrum of fluorescein.....	32
Figure 2.10: Droplet mixer with fluorescence detection.	34
Figure 2.11: Absorbance of dye methyl yellow in the visible region.	36
Figure 2.12: Serpentine mixer with UV/visible absorbance detection.	38
Figure 2.13: The absorbance spectrum of H ₂ O (solid line) and D ₂ O (dashed line).....	39
Figure 2.14: Cross mixer with mid-infrared detection.....	40
Figure 2.15: Cross mixer with UV/visible absorbance detection	42
Figure 2.16: The same cross mixer as figure 2.14, applied to another probe technique...	43
Figure 2.17: Bright field microscope images of the polymer gaskets from Dolomite Microfluidics.....	46
Figure 2.18: The updated capillary mixer.....	48
Figure 2.19: Calibration results for the new capillary mixer.....	50

Figure 3.1: The differences in microchannel geometry due to the laser cutting.....	55
Figure 3.2: Fully assembled original microfluidic mixer	57
Figure 3.3: The left image is the assembled mixer without the tubing connected.....	57
Figure 3.4: Schematic of the optical design of the infrared imaging system.....	59
Figure 3.5: An example of what an ideal sample jet looks.....	62
Figure 3.6: Custom-made optics box housing all optics for the infrared imaging system	64
Figure 3.7: Images from the infrared array detector exemplifying the etalon effect	66
Figure 3.8: Equilibrium FTIR spectra of AMP.....	69
Figure 3.9: Experimental data of absorbance versus detector pixel number	71
Figure 3.10: AMP pD jump experiment	73
Figure 3.11: Comparison of experimental results and simulation of H ₂ O/D ₂ O mixing..	78
Figure 3.12: Simulated concentration decays versus time computed with COMSOL.	80
Figure 4.1: Schematic of a stopped-flow instrument	85
Figure 4.2: Accessible timescales for relaxation methods, stopped-flow, and microfluidic mixing	87
Figure 4.3: Crystal structure of DHFR.	88
Figure 4.4: DHFR catalyzed reaction of DHF to THF with the cofactor NADPH.	89
Figure 4.5: Catalytic cycle of DHFR	90
Figure 4.6: Equilibrium fluorescence spectra of DHFR cofactors and substrate.	91
Figure 4.7: pH dependence of NADPH fluorescence in the DHFR:NADPH binary complex.....	95
Figure 4.8: Background and sample images for DHFR flow studies at pH 4.5.	96
Figure 4.9: Background and sample images for DHFR flow studies at pH 7.0	97
Figure 4.10: Background and sample images for DHFR flow studies at pH 9.0.	98
Figure 4.11: NADPH fluorescence decay transients and exponential fits for all pH values	99

Figure 4.12: Resolved rates from the biexponential fit versus pH of complex. 102

Tables

Table 2.1: Printer parameters for producing single layer microfluidic mixers.....	28
Table 3.1: Parameters for theoretical modeling in COMSOL	76
Table 4.1: Kinetic data for pH biexponential fits of DHFR transients	101

Chapter 1: Introduction

Microfluidics has emerged as an incredibly useful research discipline over the past two to three decades. The miniaturization of reaction platforms allows for small sample and reagent consumption, less time consumption, lower cost, and high throughput. Because of these advantages, the field has grown to cover a wide range of topics including, but not limited to, protein folding,¹⁻³ DNA sequencing,^{4,6} single cell analysis,⁷⁻⁹ synthesis,¹⁰⁻¹² and reaction kinetics.¹³⁻¹⁹ Along with the increasing importance of microfluidics in today's research landscape, several journals have been created that focus solely on microfluidics, like Lab on a Chip, and thus research articles that deal with the topic have been increasing almost exponentially ever since.²⁰

One particular line of research that has benefitted from the advances in microfluidics deals with biochemistry, and specifically the study of proteins and enzymatic reactions. Enzymes are a class of proteins that catalyze specific reactions. The function of an enzymes is to simply increase the rate of a reaction when compared to the uncatalyzed reaction. Rate enhancements of reactions occurring with enzymes have been reported up to 10^7 - 10^{19} times faster than without the enzyme.²¹ These increases in rates of reactions are impressive especially due to the fact that enzymes usually must operate in aqueous solutions at low concentrations and moderate pH and temperature conditions. Synthetic catalysts, on the other hand, often can handle more extreme conditions like high or low pH, high temperatures, and high concentrations that optimize their function. Because of their utility in biochemical reactions, the study of enzymes is a wide and deep field of research.

Even so, there still does not exist a full molecular understanding of how enzymes do what they do. This is especially evident when researchers attempted to construct non-natural *de novo* enzymes. Here, the vast knowledge of enzymatic catalysis is applied to designing a brand new enzyme to catalyze a reaction of choice. If the knowledge of enzymes that includes enzyme structure and catalytic mechanisms is known so well, then we should be able to design new enzymes that rival catalytic efficiencies of naturally occurring ones.

Siegel and coworkers attempted just that, and chose to computationally design an enzyme to catalyze a Diels-Alder reaction with high stereoselectivity and substrate specificity.²² Their computational designs were quite successful at first, designing enzyme active sites with >97% stereoselectivity for the particular reaction. However, that result was not without challenge. Of the $\sim 10^6$ computationally designed active sites, only 50 of those were able to fit into a protein backbone structure. Furthermore, only two of those 50 candidates showed any measureable catalytic activity. The best k_{cat} between the two was 2.13 hr^{-1} and the catalytic efficiency ($k_{\text{cat}}/K_{\text{M}}$) was $0.455 \text{ s}^{-1} \text{ M}^{-1}$.²² Even after further studies for backbone refinement²³ and directed evolution,²⁴ k_{cat} was only improved to 10.8 hr^{-1} and catalytic efficiency to $103 \text{ s}^{-1} \text{ M}^{-1}$.²⁴ The *de novo* enzymes do not come close to average enzyme values (k_{cat} of 10 s^{-1} and K_{M} of $\sim 10^5 \text{ s}^{-1} \text{ M}^{-1}$) which come from analysis of several thousand enzymes in the literature.²⁵ Clearly the models that were used to design these *de novo* enzymes were missing key details as to how enzymes function. And according to recent reports, Preiswerk and coworkers suggest the key detail that is missing from our understanding of enzymes is that of protein

dynamics.²⁴ Protein dynamics can be quite small phenomena, such as molecular vibrations, or large, like loop movements.

To this end, experimental techniques are needed to readily access and unlock the details of what enzymes are doing throughout their catalytic cycle and when they are doing it. Dynamics associated with enzyme catalysis are known to occur over a range of timescales²⁶⁻²⁹ and are summarized in figure 1.1. Fast timescales, pico- to nanoseconds (ps-ns), account for dynamics stemming from fast backbone and side chain motions and are commonly studied by NMR relaxation techniques.^{27,30-33} Conformational changes, ligand binding, allosteric regulation, and catalysis can occur on the μ s-ms timescale and can be studied through relaxation techniques and fast mixing techniques.²⁷ The latter of which is the main focus of the work presented here and will be dealt with in detail. There is, however, no straightforward relationship between the ps-ns and μ s-ms dynamics and therefore must be studied independently with different techniques.²⁷ Dynamics occurring on the timescale of milliseconds and slower can be studied with microfluidic mixing as well as stopped-flow.

In order to study μ s-ms timescales with fast mixing techniques, spectroscopic probes are always coupled with mixing. Depending on the events being observed, a multitude of probes are available. Commonly, mixers are limited to a single type of spectroscopy, but the types have a wide variety including emission,^{13,34-42} Raman,^{43,44} UV/visible absorption,⁴⁵ infrared,^{2,14,46-51} NMR,⁵² and circular dichroism⁵³ to name a few.

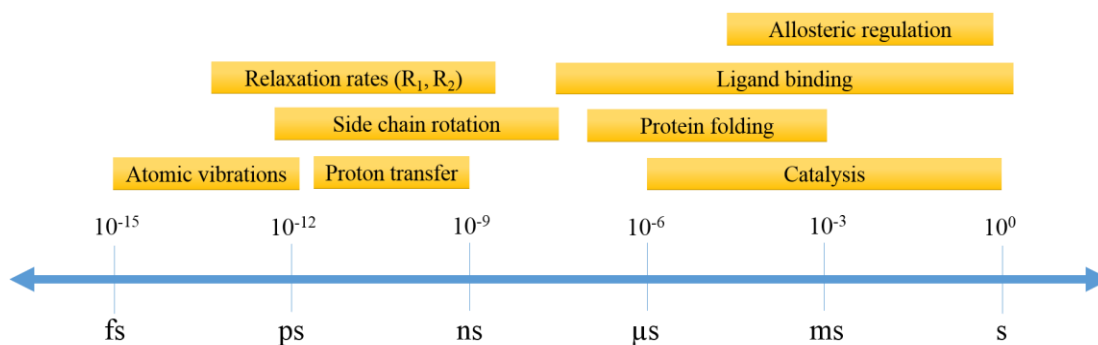


Figure 1.1: Common timescales for different dynamic events occurring in enzymes

When designing an experiment to study time dependent events like in an enzyme, a critical matter is how to initiate the event being studied. As long as all reaction conditions like concentrations of reacting species, pH values, and temperature are met, the reaction being studied will occur spontaneously and proceed as dictated by the kinetics of the particular event. However, therein lies the problem of knowing when the reaction is initiated and therefore when to observe the events taking place. The simple solution is to create control over initiating the event and therefore know exactly when to observe. There are several experimental methods that allow for reaction initiation on all timescales mentioned above and microfluidic mixing is no different. And because fast microfluidic mixing on the μ s-ms timescale is the focus of this work it will be discussed in detail.

Fast mixing is comprised of rapidly mixing solutions in order to initiate a reaction or event. The mixing process needs to be complete, or complete enough, in order for observations to start. The quicker mixing can occur, the faster the homogeneous event is initiated, and the faster the timescales able to be observed. The microfluidic mixer is arguably the most important component of a microfluidic mixing system. Not only does it dictate reaction initiation by controlling how the mixing of samples will occur, but it also

controls the types of reactions that can be studied. In the broadest sense, types of mixers can be divided into two categories, passive and active. Passive mixers use no external energy or force to mix samples in the device, relying solely on diffusion and advective mixing forces.²⁰ Active mixers on the other hand incorporate disturbances by an external field to achieve mixing. The external forces can range from pressure, to temperature, to dielectrophoretics, and electrokinetics. Active mixers tend to have more complicated designs and are more expensive to construct. Because of those disadvantages, all of the mixers used in the studies described throughout this work incorporate passive mixers, and thus will be the primary focus.

In order to discuss passive mixers, operating parameters that describe microfluidic mixing first need established. The two most important parameters for the following discussion are the Reynolds and Peclet numbers. The Reynolds number represents the ratio between momentum and viscous friction of flowing fluids and is defined as:

$$Re = \frac{UD_h}{\nu} \quad (1.1)$$

$$D_h = \frac{4A}{P} \quad (1.2)$$

where U is the fluid flow velocity, ν is the fluid viscosity and D_h is the hydraulic diameter, used in the Reynolds number calculation for the case of fluid flow in a closed channel. The hydraulic diameter accounts for the cross-sectional area and wetted perimeter of the tube or pipe carrying the fluid. A Reynolds number above the critical value of 2300 is said to be turbulent flow, whereas smaller Reynolds numbers indicate laminar flow. The Peclet number represents the ratio between the mass transport of flowing species due to convection versus diffusion and is defined as:

$$Pe = \frac{UL}{D}$$

where L is the characteristic length of the mixer and D is the diffusion coefficient of the flowing species. When $Pe \ll 1$ it is said molecular diffusion will dominate the mixing of species, whereas when $Pe \gg 1$ convection, and specifically advective forces will dominate.⁵⁴ The Reynolds number is important in microfluidics when describing the type of flow in a mixer and the Peclet number aids in describing the forces that dictate mixing within the mixer.

Due to the simplicity of the passive mixer setup with regards to the lack of external forces to aid in mixing and dominating laminar flow, mixing occurs by molecular diffusion and chaotic advection. Increasing the cross-sectional contact surface between fluids in a mixer, as well as decreasing the pathlength that species must diffuse to be considered efficiently mixed, can decrease the required time for molecular diffusion. A popular technique to accomplish the latter, is the use of hydrodynamic focusing in parallel lamination mixers, as described by Knight and coworkers.³⁷ Parallel lamination mixers have inlet substreams which are at first separate and then combine to flow in the laminar regime and initiate mixing. The simplest parallel lamination mixer has two substreams, but does not utilize hydrodynamic focusing. The basic design is a long microchannel with two inlets (arrows). It is commonly known as the T- or Y-mixer, as shown in figure 1.1a, and is one of the original microfluidic mixer designs.⁵⁵⁻⁵⁷ Mixing in the Y-mixer is dominated by molecular diffusion and therefore requires a long microchannel length to ensure complete mixing. One simple way to decrease the mixing pathlength is to make the channel more narrow, however that is not always possible. Additionally, another substream can be added to the Y-mixer and a focusing mixer

results. Here, the two side substreams (commonly called the sheath solutions) hydrodynamically focus the center substream (sample) into a narrower and narrower stream, effectively decreasing the diffusional pathlength (figure 1.1b).^{37,58,59} The width of the sample stream is dictated by adjusting the pressure ratio between the sheath and sample flows.

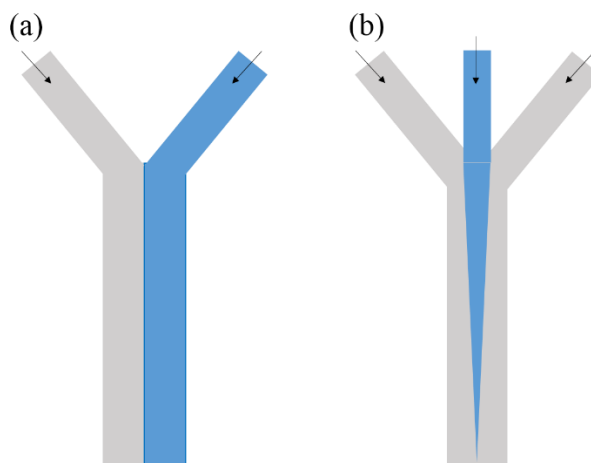


Figure 1.2: A schematic of simple parallel lamination mixers. (a) The Y-mixer which has two substreams joining in a “Y” configuration. (b) The hydrodynamic focusing mixer utilizes three substreams in parallel lamination, the two sides act to focus the middle substream into a very thin stream.

In addition to speeding up the process of molecular diffusion as described above, increasing chaotic advection within a mixer can also aid in decreasing the amount of time to mix samples. Chaotic advection will dominate mixing as long as flow is still within the laminar regime and $Pe \gg 1$. Increasing the Peclet number can be accomplished in a number of ways. Generally, chaotic advection can be generated in passive mixers by adding unique geometries to the mixer.²⁰ In a mixer with already relatively high Reynolds numbers ($Re > 100$), inserting obstacles in the flow path^{60,61} and creating zigzag-shaped channels^{62,63} are common methods to increase chaotic advection. In mixers with

intermediate Reynolds numbers ($10 < Re < 100$), variations in the shape of the channels and 3D alterations can increase the effect of chaotic advection. Channels that incorporate C-shaped⁶⁴ or L-shaped⁶⁵ serpentine segments as well as 3D twisted components^{66,67} have been successful. Finally, in mixers that inherently have low Reynolds number ($Re < 10$) other geometric techniques have been utilized. These mixers often implement subtle geometric features such as adding small grooves or ridges at an oblique angle with respect to the direction of flow in the channels.^{68,69} All of these examples exemplify the fact that slow mixing by molecular diffusion can be overcome with strategic geometric designs. The outcome of an improved design is simply the ability to mix the solutions more rapidly than before.

As described above, methods are known for ways to design mixers that will mix solutions as rapidly as possible without external forces. However, even after the design of the mixer is complete, questions still lie in what method to use to fabricate devices in a time and cost efficient manner. Then once that procedure is devised to fabricate the mixer, there are still questions as to how microfluidic mixing can be more readily applicable to various types of spectroscopy and not just a single probe. Finally, answering the question as to how the developed microfluidic mixing techniques can ultimately move the field forward in finding out novel information within enzymatic reactions. These are the questions that will be addressed throughout the following work. Chapter 2 describes the microfluidic mixer design that was utilized for many of the flow experiments described throughout this paper. The calibration of an inherited mixer is discussed first. The calibration allows for a conversion of a length scale within the mixer to time based on the linear flow velocity of the sample. Then, work that was done in order to optimize

the design of the mixer is discussed and its implications. Multiple fabrication techniques are discussed and how those techniques allow for multiple spectroscopic probes within the same mixer. Chapter 3 discusses how the need for devices that could be probed in the infrared region led to the development of an infrared imaging system used in parallel with microfluidic mixing. Further characterization of the mixer was completed with the newly developed imaging system and applications of the system are discussed. The continuous evolution of the imaging system and its components are also discussed in Chapter 3. Finally, in Chapter 4, an application of microfluidic mixing to the study of enzymatic catalysis and dynamics is discussed in detail. Mixing studies are utilized to follow the pH dependence of the hydride transfer step in the model enzyme, dihydrofolate reductase.

Chapter 2. Microfluidic mixer design and optimization

Section 2.1 Introduction to microfluidic mixer design

Microfluidic mixers that are used in order to follow the kinetics of reactions can commonly be placed into one of two categories, fast or slow mixing devices. Fast mixers are designed to be able to follow reactions on fast timescales because they mix sample solutions more rapidly than slow mixers. However, fast mixers do not mix sample solutions instantaneously and always have an amount of time associated with how long the mixer requires to create a homogeneous enough mixture between the flowing samples. This amount of time is known as the mixing time. Mixing times have a wide range in the literature according to design, but reports of mixing times on the order of 10s of microseconds are not uncommon for fast mixers.^{1,35,37}

If the goal is to design a fast mixer, there are many important factors that must be addressed. First, is whether the mixer achieves homogeneous mixtures by passive or active mixing. These concepts were discussed previously, but briefly, active mixers use external forces like pressure,⁷⁰ electrokinetic instability,^{71,72} and acoustic disturbances.^{73,74} Pressure disturbances are commonly created by starting and stopping fluid flow or by pulsing the flow velocity. Electrokinetic instability utilizes fluctuating electric fields to effect mixing, while acoustic disturbances can evoke vibrations on the samples as perturbation. Passive mixers on the other hand use no external forces to mix samples and rely solely on molecular diffusion and chaotic advection.

If a passive mixer is utilized and flow is laminar, these mixers can be subdivided into one of two categories, in-plane or out-of-plane mixers.⁷¹ In-plane, or more commonly, two dimensional (2D) mixers, utilize fluid channels that are all located in the

same plane. There is a plethora of 2D designs ranging from simply converging two fluid streams to one to incorporating many fluid streams in serial lamination with unique geometries. On the other hand, out-of-plane, or 3D mixers, can sequentially split, stack, and recombine fluid streams in elaborate 3D networks to increase mixing efficiency⁷⁵ or simply utilize all dimensions to hydrodynamically focus sample streams to narrow widths.^{34,35} 2D mixers are traditionally less intensive to fabricate whereas 3D mixers often are very intricate in their construction. Production techniques of mixers are discussed in detail elsewhere.

The next factor needing addressed when designing a mixer is the material in which the mixer is constructed. The first widely used material to produce mixers was silicon. The channels were often wet etched from a solid silicon substrate with concentrated KOH^{55,75,76} or dry etched with deep reactive ion etching.⁷⁷⁻⁷⁹ Both wet and dry etching use the same concepts in order to obtain etched channels. They both start with a solid substrate, apply a mask to the silicon to protect areas that are not to be etched, then apply the etching agent to create channels to the locations of the silicon that are not covered in the mask (figure 2.1). Wet etching uses liquids to remove material from the substrate, of which the amount can be controlled by variables like concentration of etcher, temperature, and crystalline structure of the silicon. Dry etching on the other hand utilizes high energy reactive plasma beams to remove substrate atoms. After channels are etched a glass coverslip is anodically bonded to the top of the channel which both seals the channel and provides optical access. However, silicon mixers are usually expensive to produce, require cleanroom facilities for fabrication, and are not always chemically or biochemically compatible with samples.²⁰

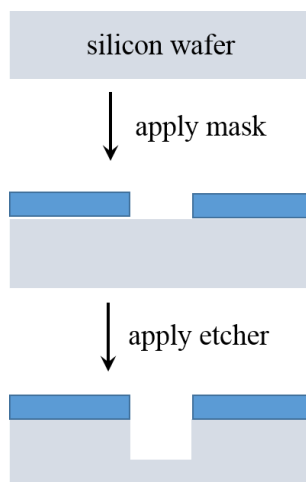


Figure 2.1: Etching process to create microfluidic channels from both wet and dry etching techniques. A silicon wafer substrate is coated with a mask through a lithographic process. The etching agent is then applied and the silicon is etched anywhere there is no mask present.

In order to combat the weaknesses presented by etching microfluidic channels into silicon, George Whitesides and coworkers at Harvard University pioneered methods of mixer fabrication with polymers.⁸⁰⁻⁸² The elastomeric material poly(dimethylsiloxane) (PDMS) became the polymer of choice and soon the industry standard. The procedure for constructing devices made from PDMS uses replica molding and is relatively simple (figure 2.2). First, a rigid master mold is made whose surface has been patterned with the relief structures of the eventual channels. The patterns on the mold are commonly made from photoresist material applied with lithography techniques.^{80,83} The liquid polymer and curing agents are then poured over the mold and cured in a short amount of time at elevated temperatures. After curing, the PDMS mixer is slowly peeled away from the mold and a glass substrate is sealed to the mixer creating sealed channels.⁸⁴ When cast against a suitable mold, PDMS can acquire features on the sub 100 nm length scale and has many chemical and physical properties suitable for microfluidic mixing. It has optical

transparency from 240-1100 nm, it is elastomeric, electrically and thermally insulating, water impermeable, stable at pH values from <1 to 12, and chemically inert.^{82,83}

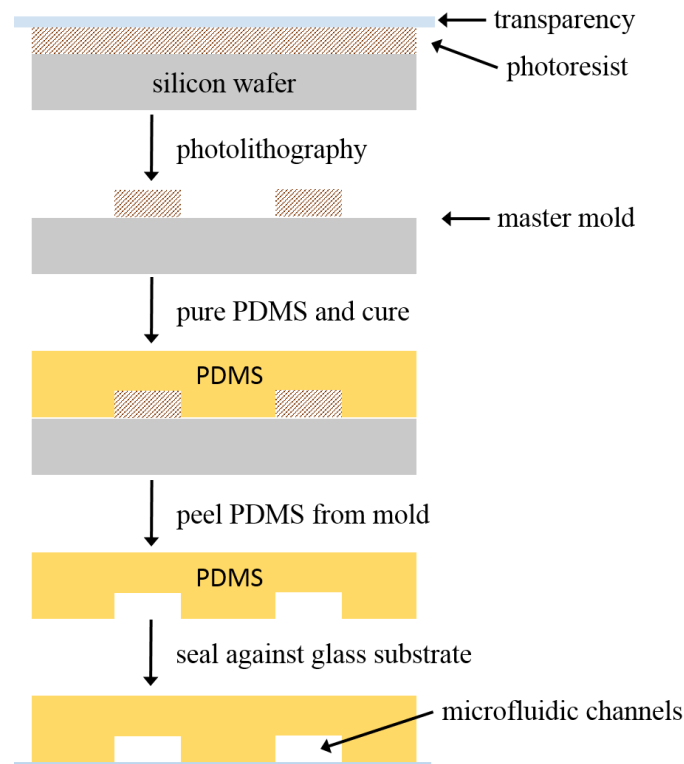


Figure 2.2: Procedure to fabricate microfluidic channels out of PDMS elastomer. Photoresist is coated on a silicon wafer on top of which is placed a transparency with the channel designs printed and used as a photomask. Light is used to cure the photoresist and the uncured photoresist is washed away. This creates the master mold with positive relief features (the same procedure could be used to produce negative relief features as well). Next, liquid PDMS is poured over the mold and cured at an elevated temperature (60-80°C) for 1 hour and then is peeled from the mold. The PDMS replica is then sealed to a flat glass substrate to create the microfluidic channels.

PDMS has become one of the most widely used materials to construct microfluidic devices for the reasons just discussed. However, there are still some drawbacks like the expensive molds and optical transparency. For researchers on a tight

budget the soft lithography method can be a large cost each time a different mixer needs to be produced. Additionally, because PDMS is only optically transparent from the UV to the near-infrared region, any spectroscopic probe outside of that range would be not be viable. Therefore, the field could benefit from a production method that is not limited by the material of the mixer. To this end, the sandwich-style mixer is a great tool. The sandwich-style mixer is discussed in detail later, but briefly, a thin polymer spacer that has channels defined in it by the lack of material is sandwiched between two optically transparent windows. Because the microfluidic channels are defined by the lack of polymer material in the spacer, the probing light is not required to travel through the polymer, and therefore eliminates altogether the question of optical transparency of the mixer itself. The only necessary optically transparent components of the mixer are the windows which sandwich the spacer. Depending on the spectroscopic probe of choice, window material can be chosen accordingly. For example, UV and visible light probes can use fused silica windows whereas infrared light probes can use CaF_2 . With the use of the sandwich-style mixer the same polymer spacer can be used while the spectroscopic probes can be varied from experiment to experiment.

Producing the polymer spacer is the largest task of this type of mixer. The microfluidic channels are defined by areas that lack in polymer material, so there are two methods to fabricate these channels. A top down method could be used in which a solid piece of polymer has material removed from it to create the channels.⁸⁵ This can be done by laser cutting the channels out of the polymer. Depending on the type of laser and the quality of the focused beam, channels can be cut from 100s to 10s of microns in diameter. A bottom up method could also be used in which the spacer could be produced from

scratch. 3D printing has recently emerged as a cost effective method to produce microfluidic mixers and mixer components.⁸⁶⁻⁹³ Commercially available printers have x-y-z-resolution of 10s of microns and can print a wide variety of polymers. 3D printing of polymer spacers has recently been implemented and will be discussed in detail in this chapter.⁹⁴

Section 2.2 The 2D fast microfluidic mixer design and calibration

The inherited mixer design from previous researchers is a two dimensional (2D) focusing mixer that uses two side sheath flows to focus a central sample stream into a thin jet (Figure 2.3). The sheath channels meet with a center sample channel at approximately a 30° angle and all fluids exit through the same channel straight ahead from the sample channel. The width of each channel is dictated by the production method, discussed in detail in Chapter 3. Briefly, the channel designs are cut out of a polymer spacer with a focused CO₂ laser. Therefore the width of the cut channels were dependent solely on how tightly focused the laser was. The channels ended up with an average width of 125 μm throughout the entire geometry, however some sections have diameters as little as 80 μm and others as large as 200 μm.

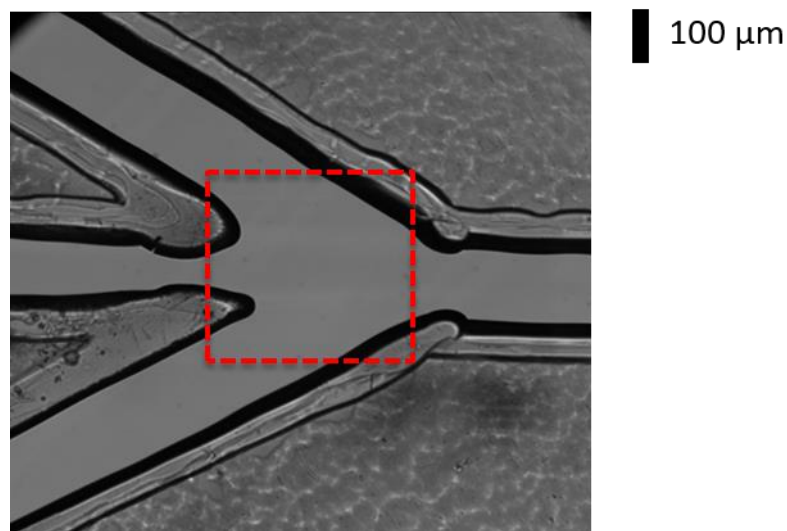


Figure 2.3: A magnified visible image of the mixer showing the three inlet channels coming together at the mixing region and the exit channel.

In order to use the mixer in a way that could relate observed chemical phenomena to a timescale, the mixer itself had to be calibrated. The main goal of the calibration was to be able to convert camera pixels from an image of a flowing sample to time. Therefore, the linear velocity of the sample needed to be determined throughout the entire mixing region. The procedure to calibrate the mixer had been done previously to calibrate another mixer in the group.³⁴ The method employs a confocal fluorescence microscope (Olympus IX81; Center Valley, PA) to image a flowing stream of 40 nm europium (Eu) carboxylate-modified fluorescent nanospheres (Life Technologies, Grand Island, NY). A 375 nm laser focused to a sharp line orthogonal to the flow direction was positioned to excite the nanospheres at a single point along the flow (figure 2.4). The beads are transiently excited as they pass through the focused laser line, and emit at 610 nm. As the beads flow away from the excitation beam, the emission decays with a known lifetime of 548 μs .³⁴ The linear flow velocity is determined by measuring the flow distance over

which the emission decays. This flow velocity is a characteristic of the mixer and is transferrable the pixels of whatever detector is imaging the mixer.

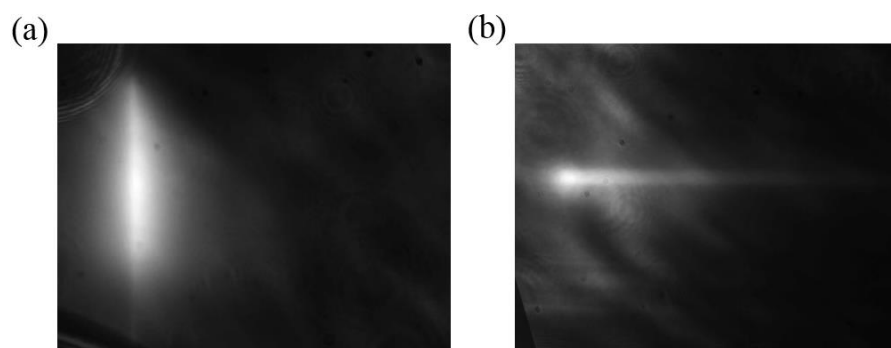


Figure 2.4: Images displaying the focused laser line used to excite the Eu nanospheres for mixer calibration. (a) Eu nanospheres flowing through the focused laser line at distance = 0 μm , corresponding to the position where the sample initially meets the sheath solutions.

At this point, the sample is moving slowly, and therefore the fluorescent decay of the nanospheres occurs in a short distance. (b) Eu nanospheres flowing through the focused laser line at distance = 280 μm , which is after the sample has accelerated greatly due to the interaction with the sheath solution. The fluorescent decay occurs over a greater distance because of its higher linear velocity compared to (a).

The linear flow velocity of the sample is not constant throughout the mixer, because it is initially significantly slower than that of the sheath flow, but it is accelerated as it flows through the mixing region, interacting with the sheath solution. Therefore, the flow calibration was obtained at multiple points along the sample flow, by varying the position of the 375 nm excitation laser line. Initially, the mixer was calibrated with the laser positioned at the start of the exit channel (Figure 2.3), a position where the sample channel is already focused to its final width and flowing at its maximum linear velocity. The mixer was calibrated at side flow rates of 15–25 $\mu\text{L min}^{-1}$ in 1 $\mu\text{L min}^{-1}$ intervals, while the sample flow was kept constant. Figure 2.5a shows that the amount of time

contained in one pixel of an image decreases exponentially with increasing flow rate. At low flow rates there is over 33 μs per one pixel whereas only about 21 μs is contained in one pixel at higher flow rates. This difference in time per pixel based on differing flow rates can drastically change the amount of total time that is contained in an entire 1024-pixel wide image, like that on the fluorescent microscope. The calibration procedure was then completed for various positions of the focused excitation laser, from the point where the three channels of the mixer initially merge (distance = 0 μm , figure 2.4a) to approximately the exit channel (distance = 320 μm) in 10 μm intervals. The side flow rates were kept constant at 20 $\mu\text{L min}^{-1}$ as the laser position was varied. This procedure established the positional dependence of the flow velocity through the usable region of the mixer. Figure 2.5b shows the sigmoidal dependence on the time contained per pixel as the distance from the merge point between sample and sheath solutions increase.

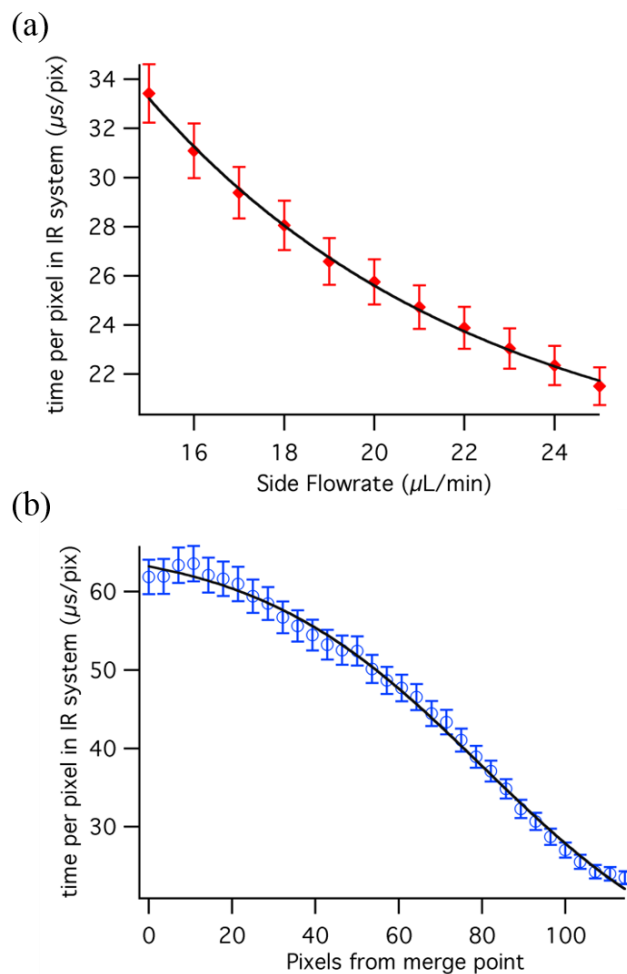


Figure 2.5: IR microfluidic mixer calibration data: (a) time per pixel, τ_{pix} versus side flow rate for the range typically used in mixing experiments (15–25 $\mu\text{L min}^{-1}$). The data fit (solid line) well to an inverse dependence on the flow rate, $\tau_{\text{pix}} \propto 1/v$. (b) τ_{pix} versus position (represented by pixels from the IR detector) downstream from the merge point at a fixed side flow rate of 20 $\mu\text{L min}^{-1}$. The experimental data are fit (solid line) to eqn (2.1).

This calibration procedure yields a value for the time per pixel (τ_{pix}) along the sample flow that can be transferred to the IR imaging system using the relative spatial resolutions of the two systems. A conversion factor of 5.5 was determined from the ratio of the spatial resolution of the fluorescence microscope ($0.50 \pm 0.01 \mu\text{m}$ per pixel) to that

of the IR microscope ($2.8 \pm 0.1 \mu\text{m}$ per pixel). Figure 2.5a plots the time per pixel, τ_{pix} , versus sheath flow rates, measured at a position near the exit channel, for which the sample stream is focused to its final width. The data fit well to an inverse dependence on the volumetric flow rate (v), $\tau_{\text{pix}} \propto 1/v$, as expected. The time per pixel values range from about 21 to 33 μs per pixel for the highest and lowest side flow rates, respectively.

Varying the flow rate across this range provides a means to control the time resolution of the detection system, the full time window accessible with the field of view observed by the array detector, and indirectly, the mixing time since the width of the jet is sensitive to the sheath flow rate (see below).

The calibration of the linear flow velocity must also account for the acceleration of the sample stream by the sheath solution. Assuming incompressible flow, when the side channels focus the sample into a small jet, the sample stretches and its velocity increases; therefore, the amount of time represented per pixel decreases.⁹⁵ The region where the jet is being focused by the side flows, denoted here as the “pre-focused region”, is characterized by slower flow. Since the flow velocity varies along the sample jet, we repeated the time per pixel calibration as a function of position through the entire pre-focused region as shown in Figure 2.5b. The position dependence of the flow velocity was mapped by moving the excitation laser line a total of 320 μm in intervals of 10 μm , from the initial merge point of the three channels (pre-focused region) to the exit channel (focused region) at a constant side flow rate of 20 $\mu\text{L min}^{-1}$. The observed behavior is sigmoidal as expected for the transition from the prefocused to the focused region, hence the data were fit to a sigmoid function in the form:

$$\tau_{\text{pix}} = \tau_{\text{max}} + \frac{\tau_{\text{min}}}{1 + \exp[(x_{\text{half}} - x)/\text{rate}]} \quad (2.1)$$

To apply this calibration to all side flow rates from 15–25 $\mu\text{L min}^{-1}$, only the τ_{min} value in eqn (2.1) is altered (τ_{max} is set by the sample flow rate, which was kept constant). The τ_{min} values for this range of flow rates was determined by the first calibration in the focused flow (Fig. 2.5a). Taken together, these calibrations enable the conversion of a spatial image to a temporal one in a straightforward manner, with numerical integration of the sigmoid fit adjusted for the τ_{min} value that corresponds to the experimental side flow rate. Finally, when converting from distance to time in the flow experiments described below, the error from the calibration fits was propagated through the calculation of the mixing times, so that the reported values account for this uncertainty.

Section 2.3 Optimization of 2D mixer design

The main goal with the design of the 2D focusing mixer was to create a microfluidic mixer with the shortest amount of time taken to adequately mix the flowing samples. This mixing time dictates the timescales of the reactions the mixer is able to follow. Ultimately, the mixer is to follow fast enzyme reactions and therefore the shorter the mixing time the better. Due to advective forces and molecular sizes of samples as described above, the mixing time is essentially dictated by how fast the sheath solution can diffuse into the sample jet. In order to design a mixer that would have the shortest mixing time, modeling software, COMSOL Multiphysics version 4.3a (COMSOL Inc., Stockholm, Sweden) was implemented in order to optimize the geometry. COMSOL includes a microfluidic flow package that is able to assess the flow dynamics and mixing behavior.

A laminar flow, stationary study using transport of dilute species was carried out in order to simulate how a sample would mix with the sheath solution. Within the mixer, the flow velocity, u , is dictated by the incompressible Navier-Stokes equation:

$$\rho(u \cdot \nabla)u = \nabla \cdot \left[-pI + \mu(\nabla u + (\nabla u)^T) \right] + F \quad (2.2)$$

where ρ is the fluid density, u is the velocity field, p is the pressure, μ is the dynamic viscosity, and F is a volume force, such as gravity. The local concentration of the reactant was the main result followed in the simulations and is governed by Fick's Law, which is described by the diffusion and convection equation:

$$\nabla \cdot (-D\nabla c) + u \cdot \nabla c = R \quad (2.3)$$

where D is the diffusion coefficient of the reactant, c is the concentration of the reactant, and R is the consumption rate of the reactant. Diffusion coefficients were chosen for both the sample and sheath solutions to reflect the coefficient for dihydrofolate reductase ($4.7 \times 10^{-10} \text{ m}^2/\text{s}$) and large molecules like dihydrofolate ($\sim 10^{-9} \text{ m}^2/\text{s}$) respectively.^{96,97}

Multiple parameters were able to be optimized with COMSOL while keeping the same general geometry of the mixer. The main parameters needing optimized were the angle at which the side channels meet with the sample channel and the diameter of all channels. Simulations were carried out to optimize each parameter independently and are summarized in figures 2.6 and 2.7. The results were analysed by following the amount of time taken for the species in the side channels, like dihydrofolate, to diffuse into the sample jet containing enzyme. The percent concentration of that species in the very middle of the sample jet was plotted versus time.

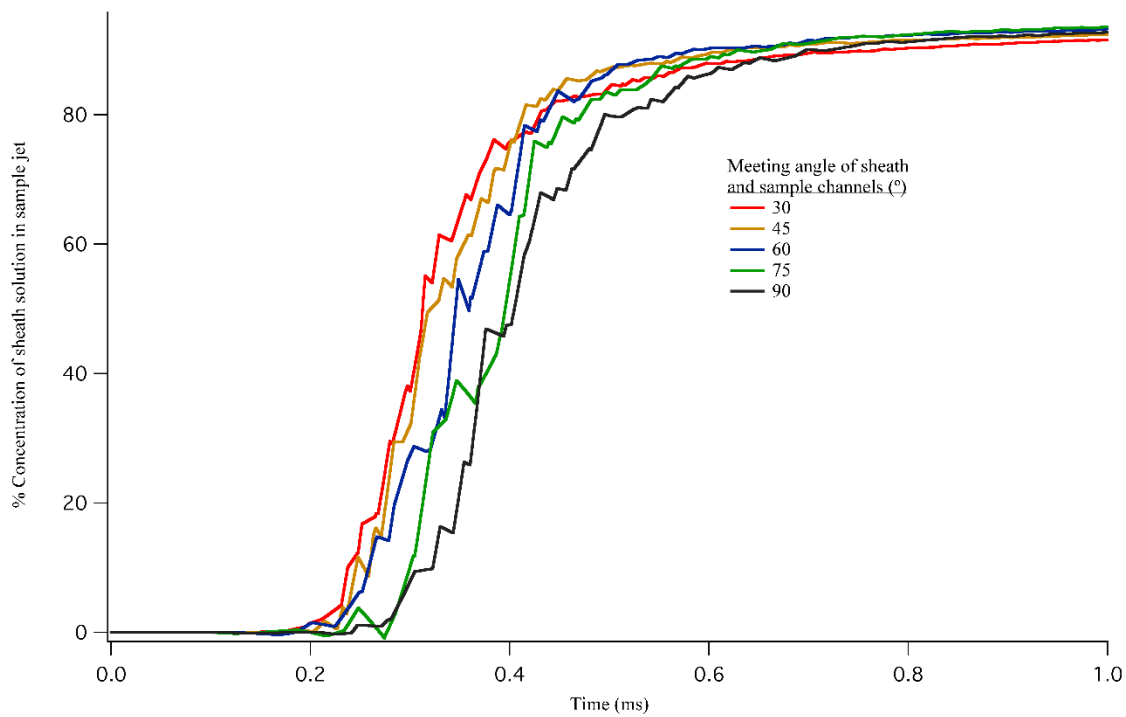


Figure 2.6: Optimization of the angle at which the sheath channels meet with the sample channel. For simplicity, all channels were held at a constant width ($25\ \mu\text{m}$).

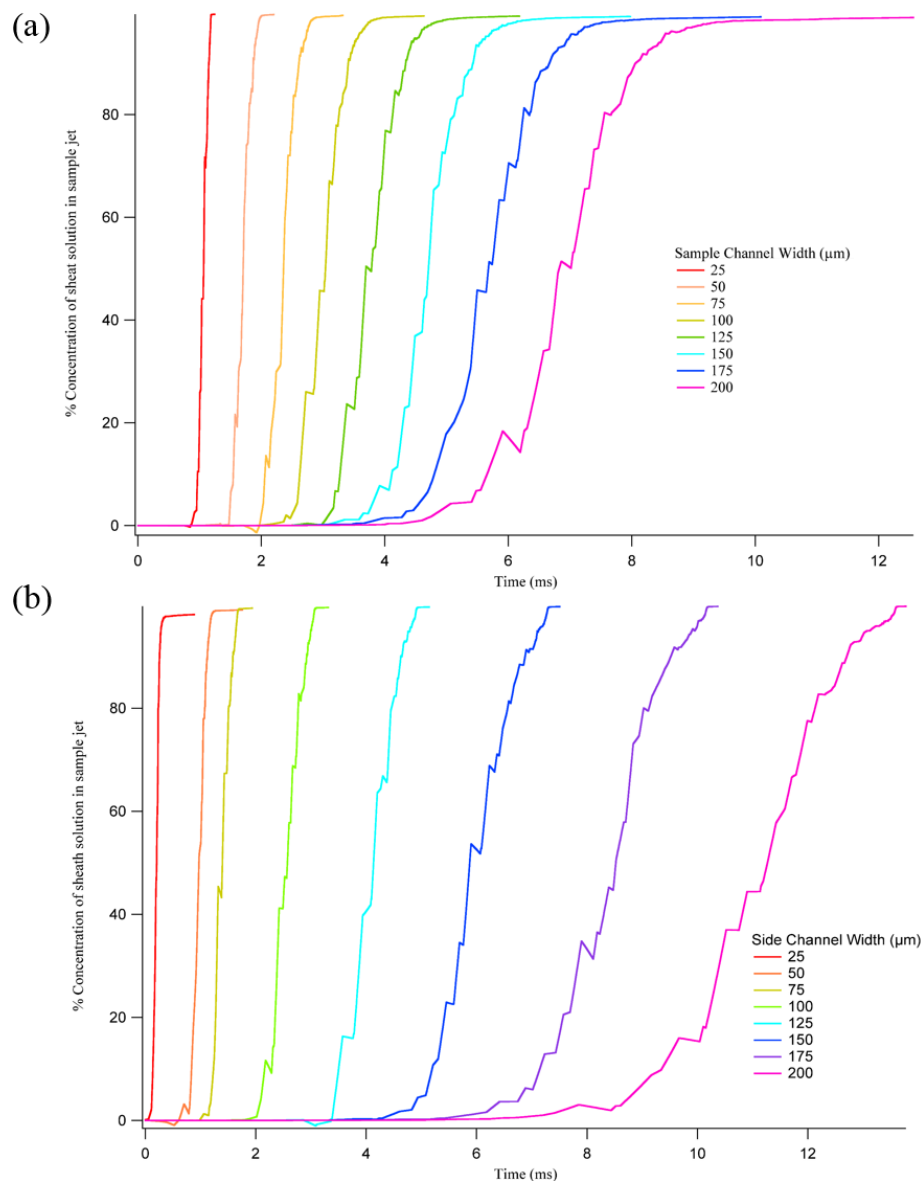


Figure 2.7: Optimization of channel diameters. (a) The sample channel diameter was varied from 25 to 200 μm . All other channels were kept at a constant diameter of 50 μm . (b) The diameter of the two side channels were then varied from 25 to 200 μm while the sample channel was fixed at a diameter of 25 μm to reflect the optimized size of previous simulations. As can be clearly observed in both simulation results, as the diameter decreases, so does the time required for the sheath solution to mix into the sample jet.

Figure 2.6 shows the simulation results for the angle optimization. This is the angle at which the sheath channels meet with the sample channel. The flow velocities for

the sample and sheath solutions were kept constant and were set to reflect the volumetric flow rates commonly used for actual experiments (sample: 0.6 $\mu\text{L}/\text{min}$, sheath: 17 $\mu\text{L}/\text{min}$). There is a slight trend in the data that suggests the more subtle of an angle the sheath channels meet with the sample, the faster mixing will occur. However, as the angle was reduced to under 25° , the trend broke down (data not shown). Due to this initial result, the 30° channels from the original design were kept the same.

The results for optimizing the sample and sheath channels are summarized in figure 2.7. The simulation results had a very clear message, the smaller the diameter of the channels, the shorter the mixing time. The spacer of the current mixer, as described previously, had channels cut with a CO_2 laser focused to the smallest possible point, and therefore narrower channels would not be possible with that method. New methods of mixer fabrication were required if the simulation optimization were to become reality.

With the simulation results along with sample flow concerns, it was decided that the optimal diameter for the mixer channels would should be approximately 10-25 μm . As is evident from COMSOL, the smaller the diameter the faster the sheath can mix with the sample. This is explained by the sample stream starting at a more narrow width and being squeezed into an even narrower jet by the side sheath solutions. The sheath solution must travel a smaller distance in order to thoroughly mix with the sample and can do so in a shorter time. However, aside from mixing time concerns, practicality of the mixer design must be accounted for and therefore channels with diameters under 10 μm were avoided. Because the mixer was being designed to flow protein samples, aggregation and viscosity of the sample must be taken into account. From time to time small protein aggregates and other particulates like dust, can be seen flowing through and getting stuck

in the channels of the mixer with channel diameters of over 100 μm . These aggregates and particulates can sometimes be cleared by using short bursts of sample at high flow rates. However, if the same clogs were to happen with channels just a fraction of the old diameter, they would not be able to be pushed through as easily. Presumably, the mixer would have to be taken apart and cleaned each time an aggregate or particulate appeared, substantially decreasing efficiency. Furthermore, if the protein samples being used have considerable concentrations (100s μM – 1 mM), which is very normal, the viscosity of the sample can become substantial.⁹⁸ With channels as narrow as, say, 10 μm , it would seemingly become a challenge to push the samples through them at desired flow rates.

Due to these concerns, the compromise at 10-25 μm diameter channels was decided. Hence thereafter the next challenge became learning new methods in order to produce the optimized mixer design.

Section 2.4 Other production methods for 2D microfluidic mixers

The main goals for the new method of spacer production was to be able to fabricate in-house and in a cost-effective manner. This led to researching an instrument normally reserved for non-scientific hobbyists but were becoming more and more useful to the scientific community, 3D printers. The recent emergence of inexpensive commercially available 3D printers had led to their application as useful tools for producing microfluidic mixers and mixer components.⁸⁷⁻⁹² Commercial desktop printers can print with x-y-z axis resolution under 100 microns and printer costs sometimes under US\$1000, potentially making 3D printing a time and cost effective technique to produce micron-sized features in mixers. Furthermore, many 3D printers have wide materials

flexibility. There are a multitude of materials on the market that are inexpensive with varied chemical and mechanical properties, including solvent compatibility and electrical conductivity. For these reasons, 3D printing had the potential to produce mixers with channels on the scale of 10s of microns. Being that the investment in a commercially available 3D printer was not a large burden, we chose to go this route.

After an exhaustive search of hobby-oriented 3D printers due to their low cost, the model HD2x from Airwolf3D (Costa Mesa, CA) was determined to have the best directional resolution, material compatibility, ease of use, and upgrade options among the others. The HD2x uses a heated extruder with a very narrow nozzle opening (350 μm) to squeeze melted polymer out in layers approximately 200 μm thick. The thermopolymer used for printing was polylactic acid (PLA) from MatterHackers (Lake Forest, CA). PLA was chosen due to its cost and ease of printing. It was compatible with biological samples but could degrade over long periods of time. It is perfectly feasible to choose another material to print with based on chemical and mechanical needs. 3D modeling was completed on COMSOL Multiphysics V4.3a (Comsol Inc., Stockholm, Sweden) and exported as a .stl file. The .stl file was prepared for slicing (repaired) with Netfabb freeware (netfabb GmbH, Parsberg, Germany). The model was sliced with Slic3r, public domain freeware used to convert a digital 3D model into printing code for 3D printers. Slic3r cut the 3D model into each individual layer the printer would print, one by one on top of each other. But because the desired spacer height was already less than the smallest height the printer could print in one layer, the design was sliced into the minimum one print layer. The printing code (.gcode file) was then loaded into Repetier-Host (Hot World GmbH & Co. KG, Willich, Germany), which read the code and translated it to the

printer. All designs were printed in one thin layer (200–250 μm) of PLA under conditions laid out in Table 2.1.

Table 2.1: Printer parameters for producing single layer microfluidic mixers

Parameter	Value
Nozzle Diameter	0.35 mm
Extruder Temperature	220 C
Print Bed Temperature	70 C
Extrusion Width	0.26 mm
Layer Height	0.20 mm
Perimeters	3
Infill	0 %
Solid Top/Bottom Layers	0
Print Speed	All 10 mm/s

After initial printing parameters were established to produce the highest quality prints with the narrowest channel diameters, three designs were chosen to further characterize and evaluate the effectiveness of the 3D printing method. The designs were all passive mixers utilizing laminar flow and diffusional mixing, although they had vastly different applications. The first mixer was a droplet-forming mixer. Droplet-forming mixers have been utilized to study many types of reactions⁹⁹⁻¹⁰¹ and work by encapsulating samples in a microdroplet which acts as a closed system and can be studied individually. These mixers have also been shown to be able to perform simple Boolean logic functions, which is a critical step towards the creation of a microfluidic computer chip.^{102,103} This method of microfluidics produces highly monodisperse droplets in the nano- to micrometer diameter range, with droplet production rates of up to twenty thousand per second.¹⁰⁴ The microdroplet is usually formed by immiscible interfaces like that between air and fluid or aqueous and organic. The second type of mixer designed was the serpentine mixer. The serpentine design has been shown to be viable following

reaction kinetics on a timescale range of milliseconds to minutes, and therefore has a wide range of applications in microfluidics.⁸⁴ The serpentine design is a convenient method to extend viewable timescales without making large mixers.¹⁰⁵ Finally, the cross-shaped mixer, which resembles the mixer described previously and was pioneered by the elegant study from Knight et al, which characterized the mixing of a microfluidic cross-shaped mixer would be the fast mixing design of the three.³⁷ The cross-shaped mixer uses side solutions to hydrodynamically focus the sample stream into a very narrow jet. Once focused, the stream remains a constant width unless broadened by sample diffusion into the side solutions or changes in flow rates occur.³⁷

Typically, a grid of 12 mixers was printed at a time (Figure 2.8a), at a cost of approximately US\$0.005 per mixer, and of the mixers that were printed, the cleanest were used and the rest discarded. In our designs, shown in Figure 2.8b, regions without printed material define the channels of the mixer, rather than printing actual channel wells. However, not all regions that are absent of material represent channels. The other regions without material (located on the outside of the perimeters that define actual channels) are due to printing with less than 100% infill. We typically use between 0–50% infill, which cuts down on material and time usage for each print. Typically, of the 12 mixers printed per batch, 4–6 mixers were useable. The others sometimes had smudged material or sealed channels. The useable mixers were collected and subjected to the annealing process, as described below, in order to smooth out the faces of the print as well as reduce the diameter of the channels.

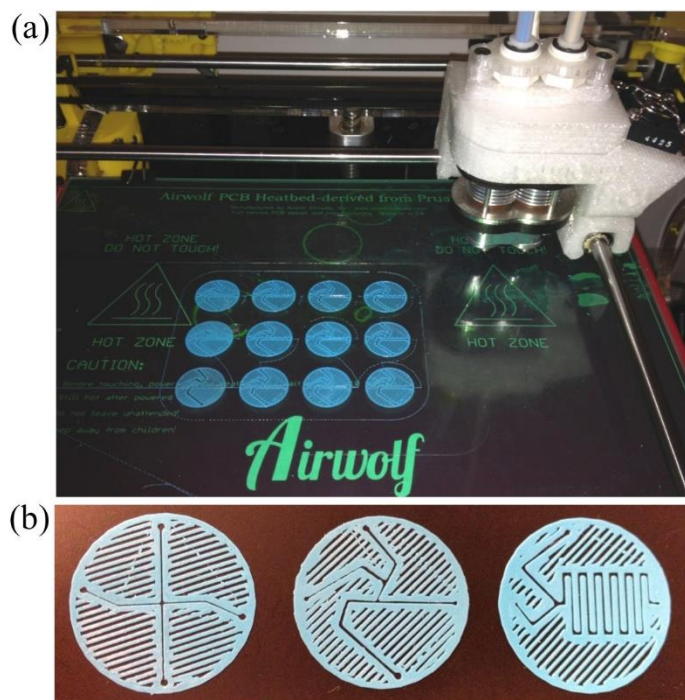


Figure 2.8: 3D printed mixers (a) grid of twelve single layer mixer prints still on the printing bed (b) images of the three mixer designs. The cross-mixer, the droplet-mixer, and the serpentine-mixer, left to right. Each circular mixer design has a 25 mm diameter.

During the annealing process, the mixers were squeezed between two glass slides, fastened with binder clips, and annealed in an oven at 170 °C for one minute increments. This treatment was used primarily to decrease both the thickness of the actual spacer (to 125–150 μm) and the width of the printed channels as well as to smooth the faces of the PLA. This also aided in creating a liquid-tight seal during mixer assembly. Once the spacer is annealed and placed into the mixer assembly (see below), there were no problems with leaking at the working flow rates described. Even when the flow rates were increased to more than two times the working flow rates described below, the mixers still had no leaks. If the printed spacers were assembled into the mixer without

first annealing, the windows did not properly seal and the mixer leaked through the polymer window interface.

Data were collected from three separate prints of the same region in the droplet mixer in order to determine the reproducibility of both the 3D printed mixer pre-annealing and post-annealing and is shown in table S3. The pre-annealed mixers had an average channel diameter of $406 \pm 38.9 \mu\text{m}$. The annealing process effectively reduced the average channel diameter to $151 \pm 29.1 \mu\text{m}$. The amount of reduction could be controlled with temperature and length of time of the annealing process. The annealed mixers with the narrowest channel diameter that still maintained the integrity of the original printed design were chosen for experimentation. Due to the resolution limitations of the printer as well as imperfect reduction in the diameter of the mixer channels during the annealing process, small aberrations were still visible in the channels. The 3D printing and annealing processes will never be able to reproduce exact copies of a specific channel design, but this was not the intention of this approach. Each assembled mixer can be independently characterized and calibrated and subsequently used multiple times with no need to replace it after each experiment or application. The final 3D printed products are shown in Figure 2.8b, with all three designs that will be discussed. From left to right are the cross-mixer, the droplet-mixer, and the serpentine-mixer.

The first mixer characterized was the droplet-forming design. Fluorescence spectroscopy was chosen as the probe and the reaction chosen to study with the droplet-forming mixer was the quenching of the dye fluorescein with iodide ions. Fluorescein sodium salt was purchased from Sigma-Aldrich (St. Louis, MO) and dissolved in deionized water at a concentration of $4 \mu\text{M}$. Potassium iodide (KI) pellets (Alfa Aesar;

Ward Hill, MA) were dissolved in deionized water to a concentration of 1 M. Hexanes (EMD Chemicals; Gibbstown, NJ) was used as the organic phase to form aqueous fluorescein/KI droplets. A fluorescence microscope (Olympus IX81; Center Valley, PA) was used to collect data for both this experiment. A 10x objective (Atlanta Microscope Service; Atlanta, GA) was used and microscope images were captured on a Hamamatsu (Bridgewater, NJ) C9100-14 ImageM-1k EM-CCD Camera. The microscope and camera were controlled by Slidebook 5.0 software (Imaging Innovations, Inc.; Denver, CO). The water soluble dye, fluorescein, was excited at 482 nm using the filtered output of a HBO mercury short-arc lamp from Osram (Danvers, MA). Emission from the sample, which peaks at 530nm as shown in Figure 2.9, was transmitted through a long-pass filter at 510 nm and directed to the camera. Separate fluorescein and KI solutions were flowed at a rate of $0.25 \mu\text{L min}^{-1}$ while the hexanes flow rate was $14 \mu\text{L min}^{-1}$ in the droplet-mixer. Fluorescence images were collected with a 50 ms integration time.

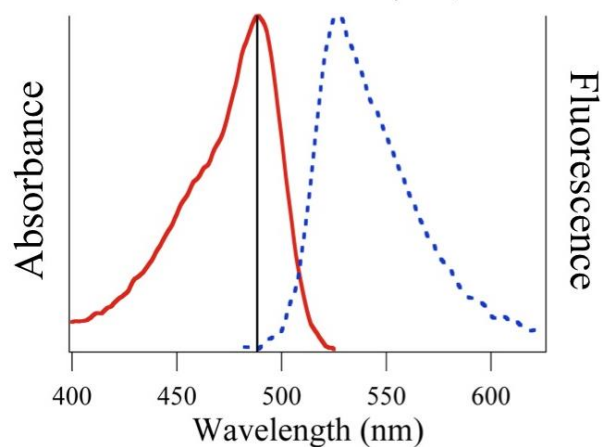


Figure 2.9: Absorbance (solid) and fluorescence (dashed) spectrum of fluorescein. The excitation filter is a bandpass filter centered at 482 ± 9 nm (solid line) and the fluorescence filter is a long-pass filter at 510 nm.

Figure 2.10 shows results obtained with the droplet-forming mixer coupled with fluorescence imaging to probe the mixing process. The entire field of view was illuminated with the 482 nm probe beam, corresponding to fluorescein absorbance and then a long-pass filter directed the resulting fluorescein emission having a wavelength of 510 nm or greater to the CCD camera. The fluorescein sample was mixed with a diffusion limited fluorescence quencher, KI, upstream from where the actual droplets were produced (figure 2.20 (a) and (b), box 1). The fluorescein and KI mixed while traveling down the channel to where the aqueous solution merged with the organic phase, in this case hexanes, and droplets were formed (figure 2.10 (a) and (b), box 2). The organic phase traveled at more than 20 times the volumetric flow rate of the total aqueous phase, and therefore soon after the fluorescein/ KI mixture protruded into the hexanes channel, it was quickly pinched off into small droplets that continued down the hexanes channel for analysis.

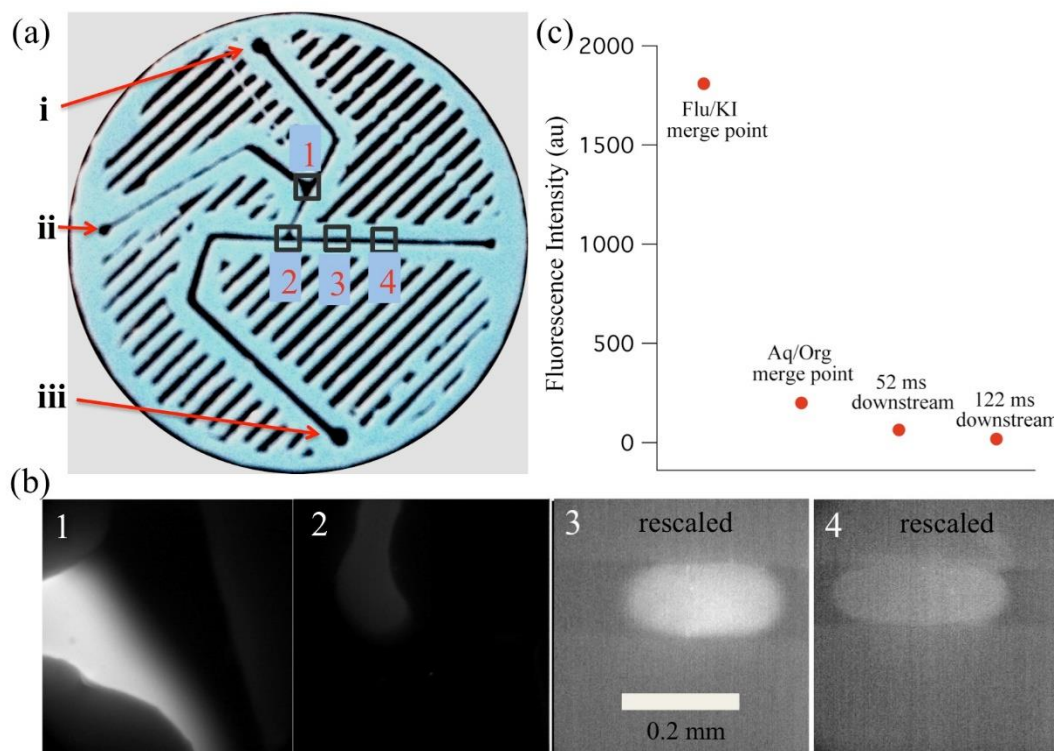


Figure 2.10: Droplet mixer with fluorescence detection. (a) Image of the droplet mixer along with numbered boxes, corresponding to the fluorescence images. (b) Box 1 shows the region where the fluorescein (from left) and KI solution (from top) streams merged. Box 2 shows the region where the aqueous fluorescein/KI solution (from top) meets the organic hexanes (from left) and the droplet is starting to form. Box 3, which has been rescaled to show contrast, shows the fluorescein/KI droplet (moving left to right) at a point equivalent to 52 ms downstream from the aqueous/organic merge point. Box 4, which has been rescaled to show contrast, shows the droplet farther downstream (moving left to right), equivalent to 122 ms from the aqueous/organic merge point. The contrast of each image was adjusted to make important details visible (the maximum intensity decreases from left to right), therefore the apparent brightness in each image does not reflect actual fluorescence intensity. (c) Plot of the average fluorescence intensity (counts) with respect to each of the imaged regions of the mixer.

In Figure 2.10a, an image of the mixer is shown with the KI, fluorescein, and hexanes inlets labelled as (i), (ii), and (iii), respectively. The fluorescence images shown

in figure 2.10b, labelled 1–4, correspond to images taken at the corresponding locations shown in figure 2.10a. Images from boxes 3 and 4 show the fluorescein/KI droplets at 52 and 122 ms downstream from droplet formation. It should be noted that the contrast of images 3 and 4 was adjusted to permit the visualization of the fluorescence, which is highly quenched at these points (nothing is visible in images 3 and 4 if they are plotted with the same contrast as 1). In image 2, the fluorescence is slightly dimmer at the interface of the forming droplet with the organic phase, which appears to be due to a difference in the focus of the image. This effect is due to the difference in refractive index of the two media, which perturbs the focus at the interface. Nevertheless, this effect is minor compared to the overall quenching of the sample. Figure 2.10c shows the actual average fluorescence intensity of the fluorescein in each image from figure 2.10b. The initial fluorescence intensity was high before mixing with KI, but was almost fully quenched by the time the droplet formed, and therefore was mixed completely in the 1.6 ms it took the aqueous solution to merge with the organic one. Changing the flow rates of the aqueous solution or altering the design of where the two aqueous solutions meet with respect to the organic can tune the amount of time from merge point to droplet formation. From the aqueous/organic merge point to further downstream, the fluorescence continued to decrease slightly, but the small decrease in intensity levels indicate that mixing was almost fully completed by droplet formation. These results showed that the droplet mixer design could be useful to follow reactions on the scale of hundreds of milliseconds to seconds.

The next mixer characterized was the serpentine design. A second spectroscopic probe, UV/visible absorbance, was used in this characterization. The experiment was

performed on the same Olympus microscope but instead used a halogen lamp source coupled with the microscope to obtain absorbance images. The dye dimethyl yellow (MY) was chosen for its strong UV/visible absorbance. MY was purchased from Sigma-Aldrich (St. Louis, MO) and dissolved in ethanol at a concentration of 50 ng mL^{-1} . The probe light was passed through a bandpass filter at $388 \pm 20 \text{ nm}$ (Semrock Inc.; Lake Forest, IL), corresponding to the peak absorbance of MY (figure 2.11). The filtered light was passed through the sample, top to bottom, collected by the objective, and directed to the EM-CCD camera. Both MY and ethanol had flow rates of $20 \text{ } \mu\text{L min}^{-1}$ in the serpentine-mixer. Absorbance images were collected with a 100 ms camera integration time.

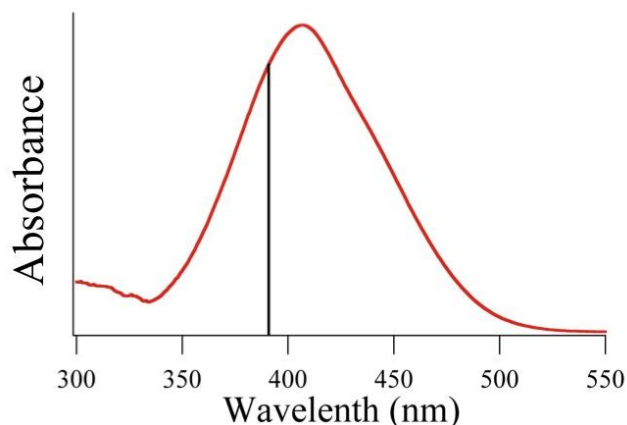


Figure 2.11: Absorbance of dye methyl yellow in the visible region. The bandpass filter used for absorbance measurements is centered at $388 \pm 20 \text{ nm}$ (solid line).

Figure 2.12 shows the results from the MY flow experiment. Figure 2.12a shows the overall geometry of the printed serpentine mixer along with labelled inlets and outlined portions that correspond to the location of the absorbance images shown below the mixer. Each absorbance image was produced by calculating the negative log of the ratio of a sample image (MY flowing) to a background image (no MY flowing, only

ethanol). Absorbance intensity is plotted in greyscale, with the lighter shade of grey corresponding to higher absorbance. From left to right, the time from the merge point of MY and water was increasing from 22 ms, to 730 ms, to 1.04 s, respectively, and therefore the distinct boundary of MY and water that exists in early time fades as slow diffusion across the channel occurs. Figure 2.12b shows the calculated absorbance level from the cross-section of the channels, defined by the dashed lines in each absorbance image. The spectral resolution of each image is limited by the width of the bandpass filter used to select the probe wavelengths, which in this case has a FWHM = 20 nm. Figure 2.12b clearly shows the gradual mixing between the MY sample and ethanol, by the smearing of the boundary. The results also demonstrate that UV/visible absorbance spectroscopy is a viable probe of mixing and more generally of reactivity in a sandwich-format mixer.

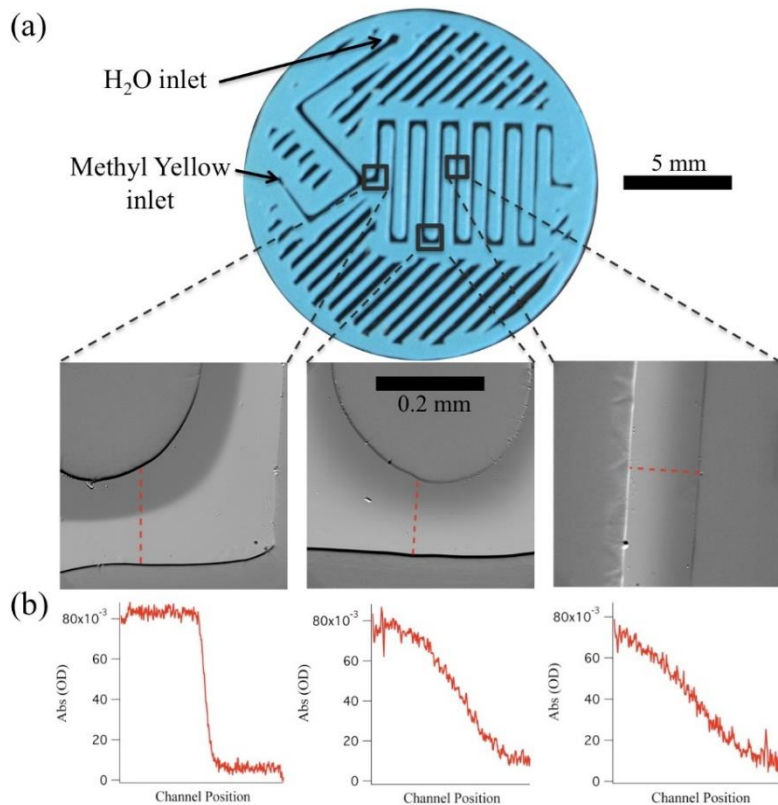


Figure 2.12: Serpentine mixer with UV/visible absorbance detection. (a) Image of the mixer; the three outlined regions represent the positions along the flow corresponding to the absorbance images below the mixer. From left to right, the images represent times of 22 ms, 730 ms, and 1.04 s after the initial merge point. Absorbance was calculated as the negative logarithm of the ratio between sample image intensity with MY/ethanol flowing through the mixer and background image intensity with only ethanol flowing through the mixer. (b) Plots of the cross-sectional absorbance of the MY sample at the designated positions shown in the absorbance images above.

For the last mixer, the cross-shaped design, the same probes were implemented as just discussed, fluorescence and visible absorbance, as well as infrared spectroscopy. Multiple probes were chosen for these studies to exemplify how versatile the sandwich-style mixer (discussed in detail in Chapter 3) can be. To complete studies with the infrared probe a Varian 600 Series FTIR Microscope (Agilent Technologies, Inc.; Santa Clara, CA) was used, with modifications. Those modifications are also discussed in detail in Chapter 3, Section 5. Briefly, an external quantum cascade laser IR source (QCL; Daylight Solutions, San Diego, CA) first travelled through a shutter (to aid in subtracting dark noise from each image) and then was fed into the microscope using its transmission optical path. After the collimated beam passed through the sample, it was magnified by a broadband infrared transmissive ZnSe objective (Edmund Optics Inc; Barrington, NJ). The objective magnified the beam onto a cooled Hg:Cd:Te focal plane array (FPA) detector for imaging. The FPA detector contains a grid of 128×128 pixels that is used to acquire an image of the transmitted IR intensity in the range of 2–12 μm . The final magnification due to the objective was 14x. The detector integration time was set to 100

μs while the detector gain, bias, and DC offset were adjusted to use the full dynamic range of the detector.

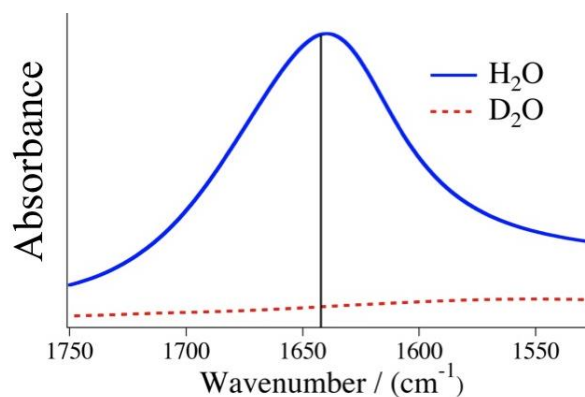


Figure 2.13: The absorbance spectrum of H_2O (solid line) and D_2O (dashed line) in the mid-infrared region. For the current study, measurements were taken at 1643 cm^{-1} (solid line), corresponding to the strong bending vibrational mode of water.

The experiment chosen for the study was the mixing of H_2O and D_2O samples. H_2O contains a strong bending vibrational mode centered at 1643 cm^{-1} (figure 2.13), while D_2O is optically silent in that region. Therefore, the QCL was tuned to 1643 cm^{-1} and an absorbance image for the $\text{H}_2\text{O}/\text{D}_2\text{O}$ flow experiment was produced by acquiring both a sample and background image and then computing absorbance as the negative log of the ratio of sample to background. Here, the sample image is acquired with a D_2O sample flow and H_2O sheath flow, whereas the background image is acquired with only D_2O flowing through the mixer. D_2O (Cambridge Isotopes, Tewksbury, MA) had a sample flow of $3\ \mu\text{L min}^{-1}$ and the H_2O (deionized and filtered) sheath had a flow of $50\ \mu\text{L min}^{-1}$ for each side in the cross-mixer.

Figure 2.14 shows the implementation of IR absorbance imaging with the cross-shaped mixer. In this case, a simple mixing experiment was conducted between a D_2O

sample stream that was hydrodynamically focused by H₂O side flows. Figure 2.14a shows the overall geometry of the cross-shaped printed mixer, along with labelled D₂O and H₂O inlets. The outlined portion of figure 2.14a represents the mixing region; a magnified IR absorbance image at 1643 cm⁻¹ of this region is shown in figure 2.14b. The absorbance was calculated from the negative log of the ratio of a sample image (D₂O sample flowing through H₂O side flow) and a background image (only D₂O flooding the mixer). Absorbance intensity is represented as a greyscale image, with light grey representing small absorbance. The dark regions are due to the strongly absorbing H₂O in the side flow. The inset on figure 2.14b plots absorbance versus time from the line profile marker out by the dotted line on the absorbance image. The absorbance level stays very close to zero at early times before the D₂O jet is focused to its final width. Once the jet is hydrodynamically focused, advective diffusion works to rapidly mix the D₂O and H₂O, causing the absorbance intensity to quickly increase.

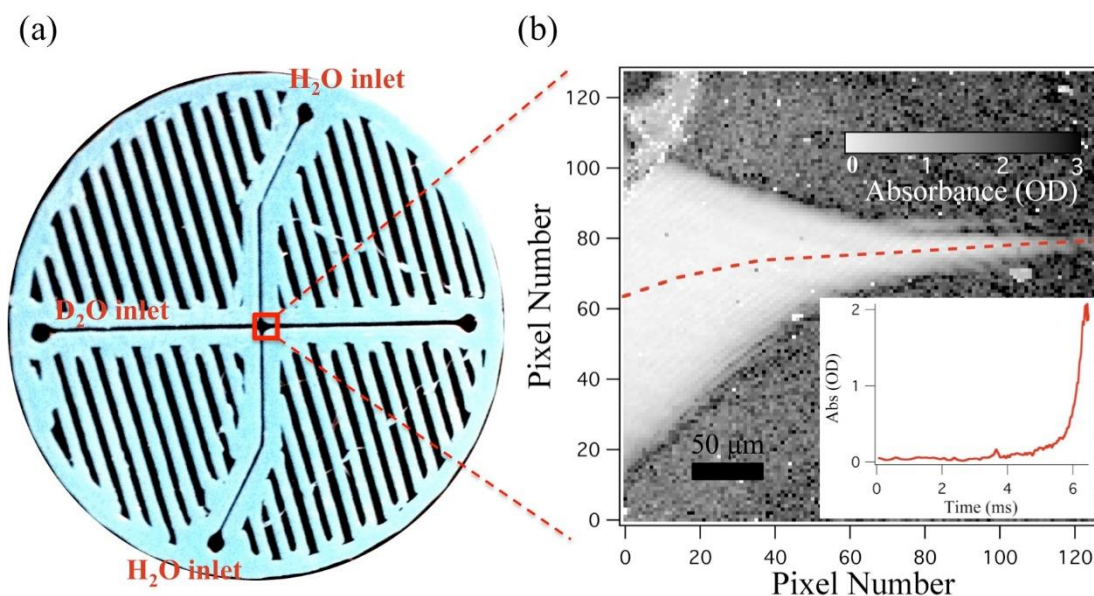


Figure 2.14: Cross mixer with mid-infrared detection. (a) Image of the cross-mixer showing the D₂O sample inlet and H₂O side flow inlets. (b) Magnified mid-infrared

absorbance image (grey scale of the mixing region) at 1643 cm^{-1} . Absorbance is calculated as the negative logarithm of the ratio of sample and background images as described in the text. The H_2O side flows squeeze the D_2O into a jet, causing mixing, and an increase in the absorbance as shown in the inset. The pixel position to time conversion was done through COMSOL simulations. D_2O had a sample flow of $3\text{ }\mu\text{L min}^{-1}$ and the H_2O sheath had a flow of $50\text{ }\mu\text{L min}^{-1}$ for each side in the cross-mixer.

The cross-shaped mixer was then integrated with UV/visible absorbance and fluorescence probes to further demonstrate the utility and versatility of the sandwich-format mixer. Figure 2.15 shows a UV/visible absorbance image of a sample stream (MY dye in ethanol solution) flowing in the cross-shaped mixer. The experiment follows the change in absorbance of the MY sample versus time (position along the jet), and thus measures the dilution caused by hydrodynamic focusing and advective mixing (dilution) of the sample stream with the ethanol side streams. The inset in figure 2.15 plots the absorbance of MY, normalized to the highest value, versus the horizontal pixel position within the detector for three different side flow rates. As the side flow rate increases, hydrodynamic focusing occurs quicker. Therefore advective diffusion mixes the MY and water sooner, and the absorbance levels decrease faster, due to dilution of the sample. Figure 2.16 shows the results of applying the third spectroscopic probe, fluorescence spectroscopy to the cross-shaped mixer. The same fluorescein sample as shown above with the droplet mixer was flowed as the sample in the cross-shaped mixer and KI solution flowing through the side channels at various flow rates. The KI quenches the emission from fluorescein at different positions along the jet, according to the magnitude of the KI flow rate. As the flow rate increases for KI, the fluorescein jet is focused to its

final width sooner and the KI molecules quench the fluorescence at earlier positions in the mixer (figure 2.16, inset).

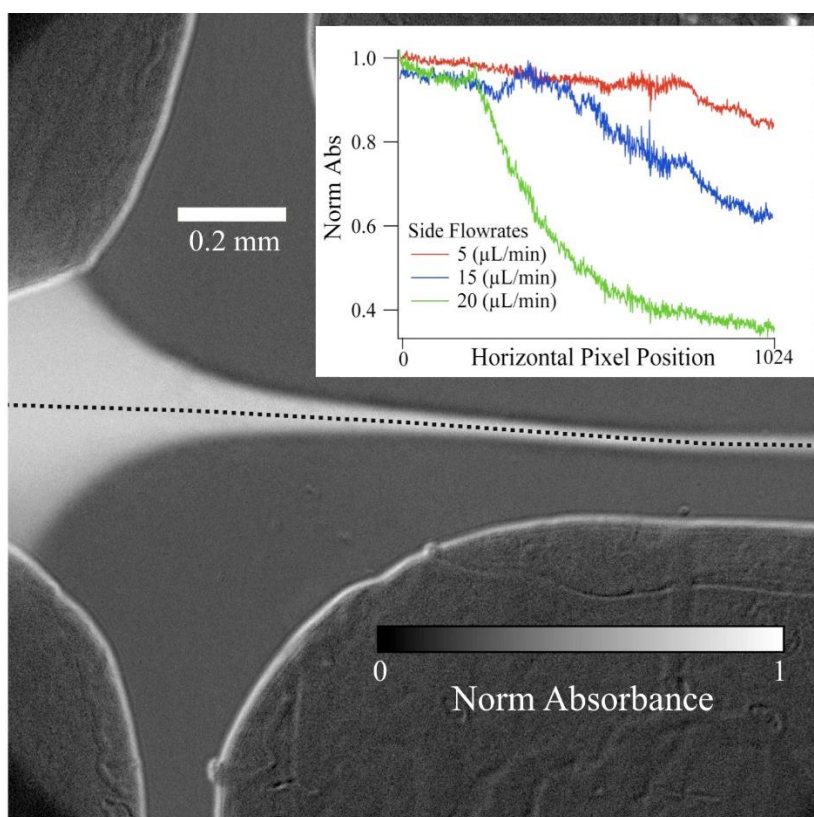


Figure 2.15: Cross mixer with UV/visible absorbance detection. An ethanol solution of MY flowed through the sample channel at $3 \mu\text{L min}^{-1}$ and was hydrodynamically focused by ethanol side flows. Inset, absorption intensity of MY jet along dashed line (in main image), normalized to its maximum value, with respect to horizontal (left to right) pixel position of the camera for three separate side flow rates. As the side flow rate increases, the amount of advective diffusion increases and the sample is diluted more rapidly, hence the faster decrease in absorbance.

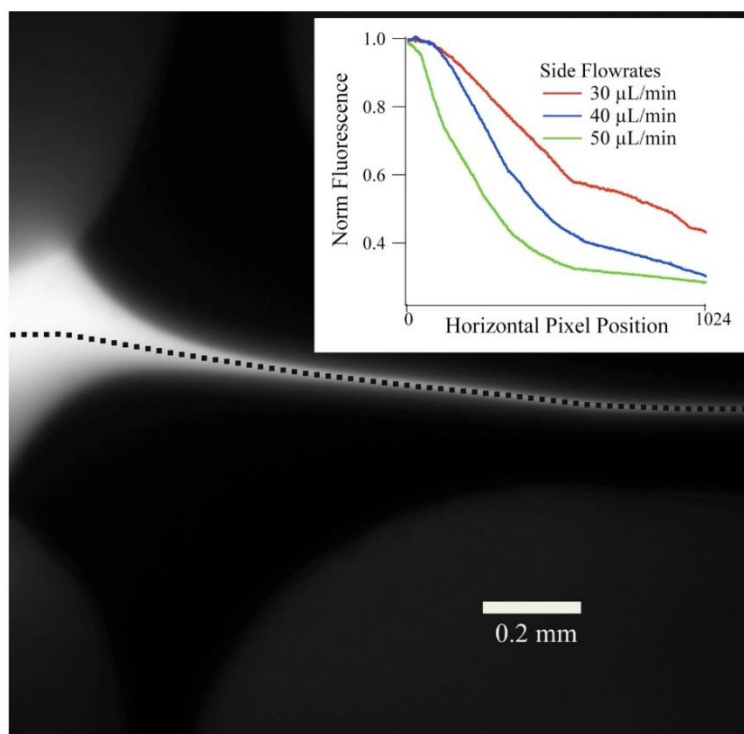


Figure 2.16: The same cross mixer as figure 2.14, applied to another probe technique. In figure 2.14, the cross mixer was used with an infrared spectroscopy probe. Here, the cross mixer is applied to fluorescence spectroscopy with the same fluorescein sample as in figure 2.10. The fluorescein is flowing at $3 \mu\text{L min}^{-1}$ and is hydrodynamically focused by the side flows. Inset, fluorescence intensity normalized to the maximum intensity along the dashed line of the jet (in main image), with respect to the horizontal (left to right) pixel position of the camera for three separate KI side flow rates.

Many conclusions were drawn from the studies utilizing 3D printed mixers. First and foremost was that even though the current commercially available hobby-oriented 3D printers had the x-y-z resolution in order to obtain printed materials with features as little as 10s of microns, these small of features were not obtainable due to the material delivery method of the printer. The printer utilizes an extruder to deliver material by simply melting the polymer and pushing it through a nozzle with a small diameter. The smallest nozzle Airwolf 3D offered for its printers had a 0.35 mm diameter, which was used for

the previous studies. While this diameter is perfectly acceptable for just about any job a hobbyist might complete, it was not sufficient in creating sharp corners or very narrow channels. Because of this limitation, producing mixers with a faster mixing time than the laser cut mixer would be impossible without further modifications to the printer.

However, not everyone who uses microfluidic mixing for research purposes is concerned with the mixing time of their mixer. Therefore, 3D printing was shown to be an extremely cost effective method to produce microfluidic devices with features as small as 100 μm . Furthermore, when printed mixers are coupled with the sandwich-style assembly (discussed in Chapter 3), the versatility of microfluidics and especially spectroscopic probes could be extended within the microfluidic mixing community and make that community more appealing to new users.

In addition to 3D printing mixers, other methods have been attempted with a lesser degree of success or are still ongoing. One method, which is still ongoing, is a piece of quartz that has the etched channels. Dolomite Microfluidics (Norwell, MA) is a company that uses hydrofluoric acid to wet etch channel designs into quartz and then typically seals the mixer with another piece of glass by irreversible heat fusion. They are able to etch channels to a diameter of 10 μm and can create sharp corners, seemingly solving all problems associated with mixer production. However, with channel diameters on the order of 10 μm , clogged channels, as discussed before, are inevitable with biological samples flowing through. This would not be a big deal to clean out of the mixer if it were able to be disassembled. Yet, with their method of sealing the channels, the etched piece of quartz cannot be separated from the solid cover glass. Therefore, a clogged channel would almost certainly put the mixer out of use and with a price

upwards of US\$1000 per mixer, it would not be an economically feasible method of mixer production.

We chose instead to purchase the etched mixers unsealed. The design of the channels resembled the original 2D mixer design with two side channels meeting the center sample channel at a 30° angle. The channels were successfully etched to a diameter of 10 μm and a depth of 15 μm . The remaining task was to determine a method to reversibly seal the channels. It needed to be sealed with a transparent window so that light probing the sample can transmit through it. This proves to be quite challenging because some sort of compressible gasket is needed in between the mixer and top window, or else leaking is inevitable. The mixer and top window are not perfectly flat enough to seal against each other due to natural imperfections in the solid surfaces. There would end up being microscopic crevices between the two solids allowing fluid to escape. Therefore, a gasket made from a compressible material was needed to create a better seal. It was also necessary to choose a material that would transmit probe light of interest, and be inert with possible biological samples because of its direct contact with all fluids in the mixer.

PDMS, as described previously, was an obvious choice. PDMS, the polymer used for the production of the vast majority of microfluidic mixers fit all parameters as well as being cheap and easy to use. PDMS is a liquid polymer that can be cured with a chemical cross-linker or with heat. Once cured, PDMS is a very durable material but can eventually be dissolved in organic solvents like toluene. With all criteria met, a method was needed in order to apply a very thin layer of PDMS to a glass cover slide and create sealed channels with the etched mixer. After much trial and error, the current method

involves spin coating a very thin layer of PDMS (100s of nanometers) onto the glass cover slide and curing it. This must be done many times until the layer of PDMS is thick enough to slightly compress and seal the channels when tightened in between the glass pieces. The layer cannot be too thick anywhere it comes into contact with the etched channels or else when the glass pieces are tightened together, the PDMS will compress too much and squeeze down into the channel well, ultimately blocking the channel. There is a lot of trial and error going into this method and it is still currently ongoing.

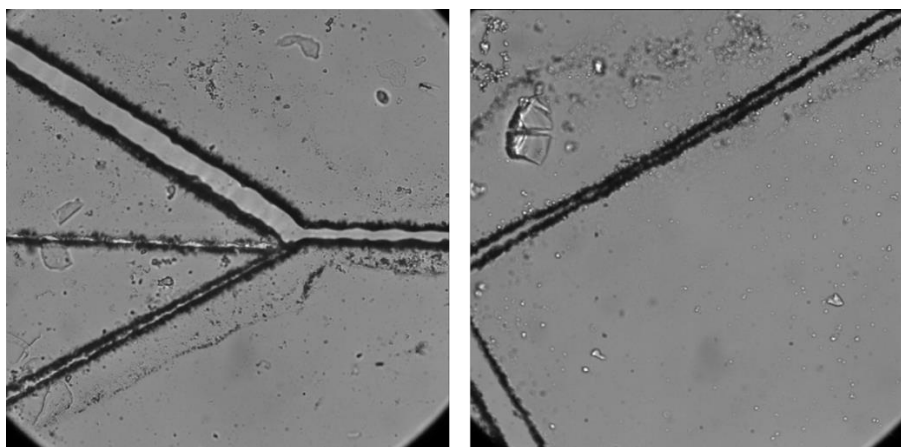


Figure 2.17: Bright field microscope images of the polymer gaskets from Dolomite Microfluidics. The channels are approximately 10 μm in diameter, however, there are obvious areas where the channels appear to be less than that and even completely closed.

Meanwhile, the same company also has a new method to produce polymer gaskets that include features on the order of 10s of microns. This method would exactly mimic the sandwich style mixer that has been discussed briefly above, and will be discussed in detail in Chapter 3. This fabricated gasket is the most promising being that no modifications to the mixer or our system are necessary in order to implement it. Images of the gaskets produced by Dolomite Microfluidics are shown in figure 2.17. In the left image, the top channel is approximately 15 μm in diameter while the exit channel

is the desired 10 μm . However, as is evident from both the left and right images, there are regions where the channels appear to be extremely narrow and even some regions that appear pinched closed. This may be due to the mixer assembly method or the channels just may be too narrow to be used. If the gasket is not assembled in the sandwich mixer with extreme precision, the fragile polymer gasket can shift slightly and cause channel dimensions to become compromised, resulting in channels that look like those in images from figure 2.17. Therefore, the ongoing task with these gaskets is to come up with a method of assembly such that the integrity of the widths of channels is not compromised.

Section 2.5 Advances in the 3D capillary mixer

In addition to the 2D mixers that have been thoroughly discussed so far, a 3D mixer is also commonly utilized in the lab. The 3D mixer has the advantage of hydrodynamically focusing the sample jet in all dimensions. The outcome is a thinner sample jet and ultimately a faster mixing time. Therefore, faster reactions can be studied. The original mixer has been described in detail by Burke et al³⁴ but modifications have been made since the original report. Briefly, the original mixer is made up of two concentric capillaries, the inner capillary carries the sample and is surrounded by the outer capillary carrying the sheath solution. The outer capillary has an outer diameter of 350 μm and an inner diameter of 200 μm , while the inner capillary has an outer diameter of 90 μm and an inner diameter of 20 μm . The end of the inner capillary was tapered using a flame pulling method to effectively decrease the diameter. To do this, the loose capillary was suspended from a support stand with a weight attached to the end, providing a pulling force on the capillary. The capillary was then briefly flamed with a

propane pencil flame burner torch which caused the capillary to melt and ultimately break into two pieces, the ends of which had tapered openings with an inner diameter of 7-8 μm .

This method effectively decreased the diameter of the capillary carrying the sample solution and therefore decreased the width of the sample jet exiting that capillary. That small initial sample jet diameter, in addition to the hydrodynamic focusing provided by the sheath solution, resulted in the capillary mixer having a very fast mixing time, well under 100 μs .³⁴ However, the pulled tips were also seemingly the cause for frequent clogs within the inner capillary. Inner capillary clogging ultimately was the main drawback of the capillary mixer as reported by Burke et al, and therefore, a method that would reduce the prevalence of clogging, but also keep the short mixing time was desired.

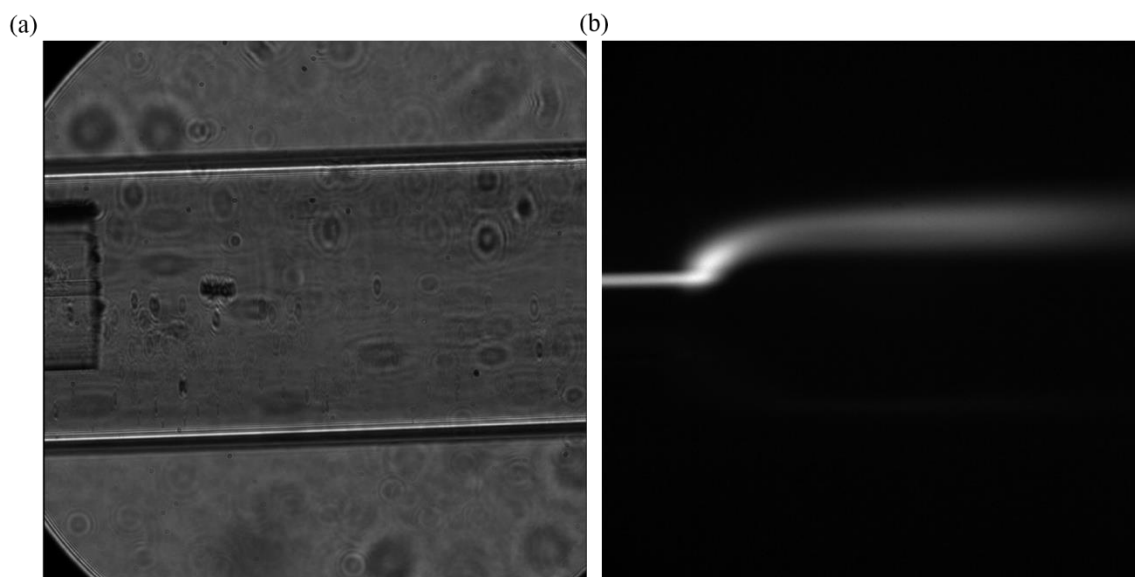


Figure 2.18: The updated capillary mixer. (a) Brightfield image of the new inner capillary inside of the outer capillary. The inner capillary shown has an outer diameter of 150 μm with an inner diameter of 10 μm . (b) An image showing the emission of a fluorescein sample flowing through the inner capillary and out into the outer capillary. This image

shows the effect on the sample stream when the inner capillary is not positioned exactly in the center of the outer capillary.

A change was made to an inner capillary that already had a very narrow inner diameter. This change made it no longer necessary to flame pull the capillary to decrease the eventual sample jet diameter. Instead, the capillaries were purchased already cut with a square edge (Polymicro Technologies, Phoenix, AZ) with an outer diameter of 150 μm and an inner diameter of 10 μm (figure 2.18a). The switch in inner capillaries seemingly solved the clogging issue but in turn created a new challenge. The new inner capillaries have an outer diameter of 150 μm , only 50 μm narrower than the inner diameter of the outer capillary. Because of this slight difference, if the inner capillary is not positioned exactly in the center of the outer capillary (which is almost always the case), the sample jet does not flow straight out of the inner capillary but rather gets pushed to one side or the other depending on uneven sheath flow pressures (figure 2.18b). If the sample jet is pushed in the z-direction, the sample jet is no longer in focus throughout the entire viewing window. To combat this problem, tedious assembly is required to ensure the inner capillary is directly centered in the outer capillary or images must be taken while operating in a confocal setting.

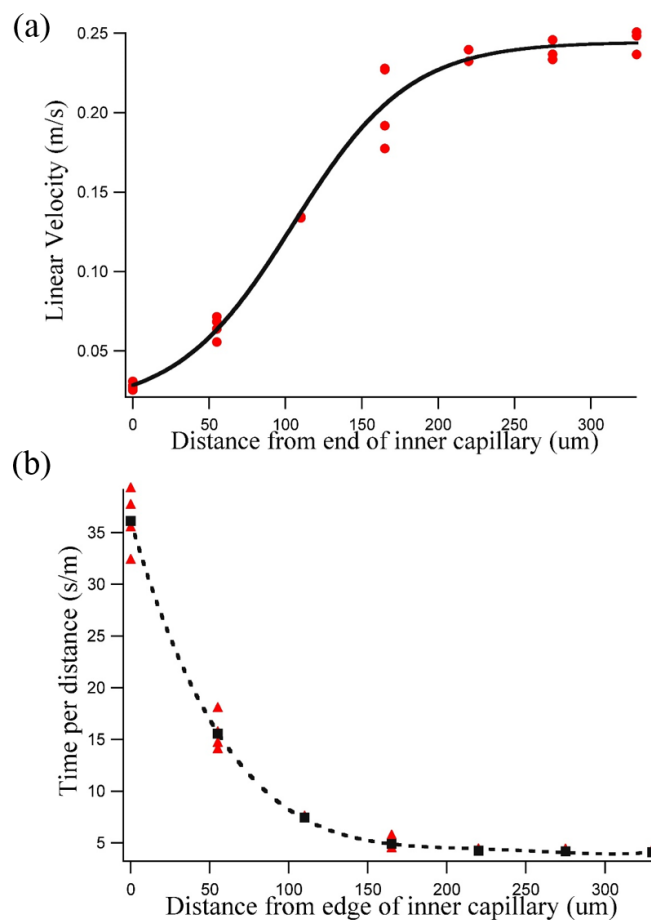


Figure 2.19: Calibration results for the new capillary mixer. (a) The distance (number of pixels) of Eu fluorescence and emission lifetime was used to calculate the linear velocity of the sample based on the distance from the square edge of the inner capillary. The red circles represent the data from all four calibrations and the solid black line is the sigmoid fit to the average of the four calibrations

The new inner capillary has been able to remedy the clogging problem associated with the pulled tip inner capillaries and in order to make it user ready was calibrated in the same way as described previously with the excitation of Eu beads as a tracer dye. The fluorescent Eu bead sample was excited with a 375 nm source that had been focused to a narrow line. The sample was excited as it flowed through the excitation source and then fluoresced with a known lifetime. A total of four calibrations were completed. In figure

2.19a the linear velocity of the sample stream is plotted versus the distance from the square edge of the inner capillary. Just as with the 2D mixer, the sheath solutions act to speed the sample solution up due to the drastic differences in volumetric flow rates between the two. The linear velocity (v) dependence on distance from the end of the inner capillary was then fit with a sigmoid function (eqn 2.4) to the average of the four calibrations (solid black trace in figure 2.19a).

$$v = 0.015 + \frac{0.23}{1 + \exp\left(\frac{105-D}{88}\right)} \quad (2.4)$$

where D represents the distance in microns from the edge of the inner capillary. Next, the amount time per unit distance (τ_{dis}) was plotted versus the distance from the square edge of the inner capillary. The average of the four calibrations was fit to a polynomial function (dashed black trace in figure 2.19b) and is shown below.

$$\tau_{dis} = 36.1 - 0.53D + 0.0033D^2 - 9.4 \times 10^{-6}D^3 + 9.8 \times 10^{-9}D^4 \quad (2.5)$$

With the completion of the calibration, the new capillary mixer is characterized and ready to use just as before.

Chapter 3. Development of an infrared imaging system to follow submillisecond mixing reactions

Section 3.1 Introduction

Fluorescence spectroscopy is the most common detection method in microfluidic mixing systems because of its simplicity and its single molecule detection sensitivity.^{13,17,34-40,42,47} Molecules that do not contain an intrinsic fluorophore (such as tryptophan in proteins), however, require labeling with extrinsic dyes for fluorescence detection. The introduction of these probes into various regions of the molecule risks perturbing both the structure and dynamics being studied, and in some instances it is not possible to probe the specific structural dynamics of interest.¹⁰⁶⁻¹⁰⁹ In contrast, infrared spectroscopy has the ability to follow intrinsic functional groups that serve as “labels” in the infrared region, such as backbone or side chain carbonyl and amide groups, thus providing a direct and broadly applicable detection method for microfluidic mixers. Most molecules exhibit absorbance in the mid-IR region and the inherent chemical specificity of infrared spectroscopy is useful for probing molecular structure, such as secondary structure of proteins.^{110,111} Infrared spectroscopy has been implemented as a detection method in microfluidic mixers in a variety of forms, including FTIR,^{2,19,46-50} attenuated total reflectance,¹¹²⁻¹¹⁴ and IR absorbance using a broadband synchrotron source.¹¹⁵ Nevertheless, the modest time-resolution and sensitivity of these approaches has limited the application of infrared spectroscopy as a probe of reaction kinetics in microfluidic mixers.

This chapter first describes the construction of the two-dimensional fast mixer. This is the standard mixer used in many of the flow studies described throughout this

paper. Although often overlooked in the literature, the method of construction of the mixer is a very important characteristic. Poor construction can have drastic effects on things like stability, sample consumption, reliability of the mixer. Because of its importance, it is discussed here. Next, the development of the imaging system that incorporates infrared spectroscopy as the probe is discussed in detail. Herein, includes the setup of the overall system with all optical components as well as how data is collected and analyzed. After the setup and building of the imaging system was complete, a biological application was performed in order to show the viability. A pH (or more correctly, a pD) jump was performed on adenosine monophosphate, which also acted to establish the mixing time for the mixer. Finally, modifications that were necessary throughout and after the building period are discussed. Most modifications were to aid in the decreasing of noise in the data.

Section 3.2 The sandwich-style mixer

A sandwich-style mixer was primarily used for all microfluidic flow studies discussed in this paper. This type of mixer differs from more commonly used mixers with respect to its method of production. Traditionally, microchannels are etched into a material like PDMS and then sealed with a coverslip to create isolated fluid channels.²⁰ Instead, the sandwich-style mixer achieves its fluid channels by creating a spacer that will define the design of the microchannels. The microchannels are established by the lack of material in the spacer. This could be done in one of two ways. A solid piece of spacer material could have the microchannel designs removed from it, say, with a laser cutter. The spacer could also be produced while purposely leaving out material in the regions of

the microchannels. This could be done with methods like 3D printing, as described previously. Whichever method is chosen, after the spacer is produced, transparent windows then sandwich the polymer spacer to establish the top and bottom boundaries of the channels. The outcome is a sealed fluid channel with a rectangular cross-section.

Other than the spacer itself, the other key feature of the sandwich-style mixer is the transparent windows that actually create the sandwich. Because of this design, only the transparency of the windows dictate what reaction probe can be used. This is in stark contrast to other mixer fabrication methods in the literature. The most common method to fabricate microfluidic mixers is to use soft lithography technology to fabricate ‘negative’ molds from a silicon wafer.^{84,116} A PDMS and curing agent mixture is laid over the mold and, once cured, is removed and usually permanently sealed with a glass cover slide, creating a closed mixer that is optically accessible. Not only can the mold be expensive, but also the finished PDMS mixer has optical transparency only from the near-UV to near IR regions. PDMS mixers are not compatible with vibrational spectroscopy as a reaction probe because PDMS has many strong absorption bands in the mid-IR region.^{117,118} Such mixers are also not suitable for use with native tryptophan fluorescence of proteins, since the UV excitation wavelength produces strong background fluorescence from the PDMS. Therefore, a mixer fabrication method like the sandwich-style, that is more versatile and incorporates multiple spectroscopic probes, could be very useful to the microfluidic research community.

The spacer that was mainly used in the infrared imaging system experiments was made from polychlorotrifluoroethylene, or PCTFE (CS Hyde, Lake Villa, IL). This polymer was chosen due to its chemical inertness in acidic and basic conditions, as well

as with its compatibility with biological samples. Additionally, PCTFE is a cheap material and is manufactured in very thin sheets. It is extremely flexible but holds its shape very well. At the time of production, the available method to produce the spacer was cutting material away from the solid spacer. The channels were cut from the PCTFE at the Invention Studio at the Georgia Institute of Technology (Atlanta, GA) with great help from an undergraduate engineering student, Matt Marchese. The Invention Studio had a Speedy 300 CO₂ laser engraver (Trotec Laser Inc., Canton, MI) to cut the channels. The laser was focused to a point approximately 100 μm in diameter at minimum. The laser cuts through (or more accurately, melts) the polymer when contact is made. Because of the melting and subsequent cooling and rehardening of the polymer, the channels are not completely uniform or straight edged throughout the entire channel design. Some sections ended up with a wavy pattern instead (figure 3.1).

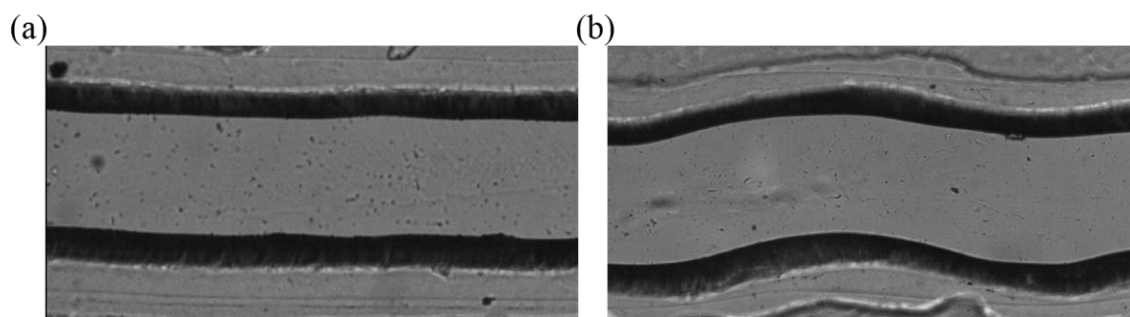


Figure 3.1: The differences in microchannel geometry due to the laser cutting method. (a) Uniformly cut channel with straight edges. (b) Wavy pattern that occurs in some sections of the microchannels.

The cut polymer spacer was then sandwiched in between two calcium fluoride windows to create the fluid channels. CaF₂ was an obvious first choice due to its optical transparency from the UV to mid-infrared region. The bottom window was a solid piece

of CaF_2 (1" diameter, 2 mm thick) while the top piece (same dimensions) had four 1 mm diameter holes drilled through it for sample delivery into the microchannels of the spacer. A custom-made stainless steel casing then fit around the mixer sandwich, in yet another sandwich formation. The two-piece case was held together with four screws (figure 3.2) to hold the mixer sandwich sealed. Fluid channels were drilled through the top piece of the metal casing, which fed the samples down into the mixer via the holes in the drilled CaF_2 window. Polyether ether ketone (PEEK) tubing was connected to the metal casing to transport the sample from syringes to the mixer itself. The fluid delivery system worked well and was reliable, however, it was found that at least 200 μL of sample was required in order to move through the metal casing channels before it arrived in the actual microfluidic mixer channels. This could be problematic when attempting to complete experiments involving very costly samples or when only a very small volume of sample can be obtained and consumed. Therefore, a change was eventually made to a new fluid delivery system. Nanoport assemblies (IDEX Health & Science, Oak Harbor, WA) were chosen due to the fact that they could be directly attached to the drilled CaF_2 window, alleviating the need to have samples travel through the metal casing, thus eliminating much of the dead volume of sample.

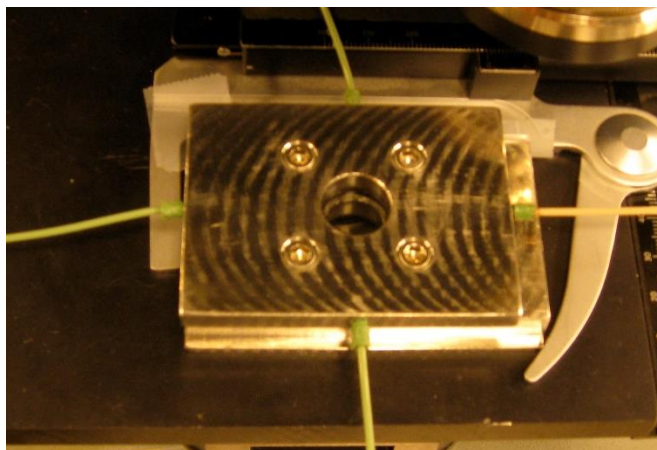


Figure 3.2: Fully assembled original microfluidic mixer. The mixer sandwich is held together with a custom-made stainless steel case in which PEEK tubing is directly connected for sample transport. The case is held together with four screws that keep the mixer sealed tightly.

Nanoports consist of two main parts, both made of PEEK polymer. A port base adheres to the CaF_2 window with a cured adhesive. Once adhered, the port can withstand pressures up to 1000 psi without leaking.¹¹⁹ The head of the Nanoport fits PEEK tubing through it and screws into the port base to hold the PEEK tubing tight and in place. But with the Nanoports being attached directly to the mixer sandwich, a new custom-made metal case was needed because the original case obstructed the area where the Nanoports were attached. The final outcome is shown in figure 3.3.

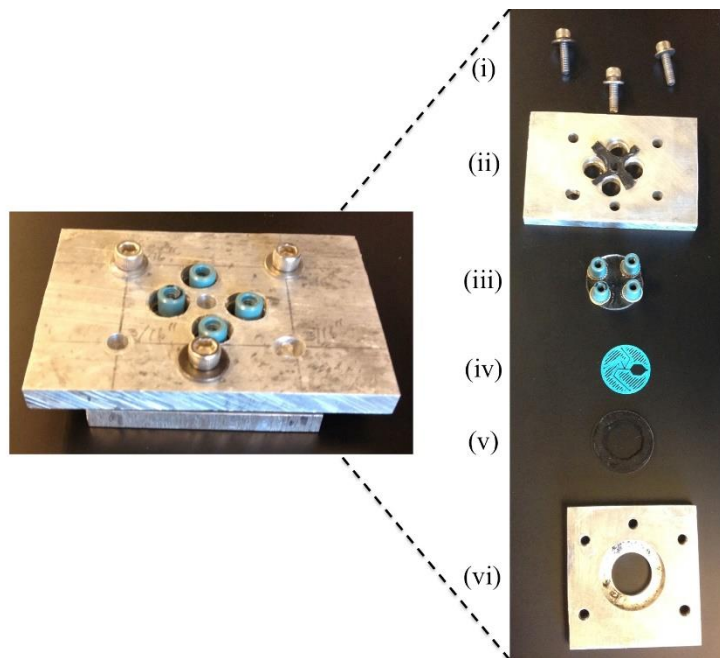


Figure 3.3: The left image is the assembled mixer without the tubing connected. In the right image, each part of the mixer assembly is shown individually. (i) Screws that hold the mixer together. (ii) Top aluminum casing piece along with a rubber protective cushion between the aluminum plate and top window. (iii) Top window with Nanoport

connections fastened permanently to the window, directly over the through holes drilled in the window for liquid transport. (iv) 3D printed mixer spacer that is sandwiched between the transparent windows. (v) Bottom transparent window along with a rubber cushion. (vi) Bottom aluminum plate with a counter-sunk hole to hold mixer in place.

Section 3.3 Development of Homemade Infrared Imaging System

An IR imaging system was specifically designed and optimized to implement vibrational spectroscopy as a probe of the flowing samples. The optical setup (figure 3.4) used a quantum cascade laser (QCL; Daylight Solutions, San Diego, CA) as the IR source, operating in continuous wave mode with a bandwidth of 0.1 cm^{-1} . The QCL has a mostly coherent and collimated output beam. A 500 mm focal length CaF_2 lens was placed before the beam reached the sample in order to aid in keeping the laser collimated. The beam then passed through a shutter for acquiring light and dark images. The laser globally illuminates the mixing region. The illumination is not completely uniform throughout the imaging region, however, with the acquisition of background images (discussed below), differences in illumination intensity should be accounted for. After passing through the sample, the transmitted laser beam was then magnified by a short focal length CaF_2 lens ($f=25.4 \text{ mm}$) and imaged onto an Hg:Cd:Te focal plane array (FPA) detector. The magnification of the beam could be controlled by altering the distance between then lens and detector. All components of the optical setup were housed in an airtight box being purged with dry air to minimize interference from water vapor absorbance.⁵⁰

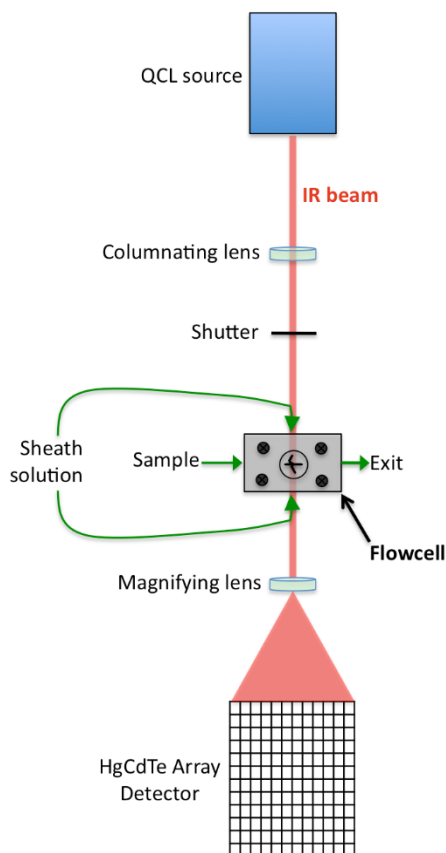


Figure 3.4: Schematic of the optical design of the infrared imaging system.

The FPA detector contains a grid of 128×128 pixels used to acquire an image of the transmitted IR intensity in the $2\text{--}12\ \mu\text{m}$ wavelength range. The detector had many parameters that could be altered in order to obtain the ideal image. Typical detector integration times were short ($\sim 40\ \mu\text{s}$) to minimize dark noise and noise from low frequency mechanical vibrations. The detector gain, bias and DC offset were adjusted to use the full dynamic range of the detector. If a range of wavelengths are needed to produce an absorbance spectrum, the laser was typically scanned in $1\ \text{cm}^{-1}$ steps and 1000 images were acquired at each probe frequency at the full 1 kHz FPA frame rate, then signal averaged to decrease the noise level. A hyperspectral absorbance image is produced by acquiring both a sample and a background image at each probe wavelength.

Absorbance is then computed by equation 3.1.

$$A = -\log\left(\frac{I_{sample}}{I_{background}}\right) \quad (3.1)$$

Sample and background images are acquired with and without the sample jet present, simply by turning the sample flow on and off, respectively. Since it takes some time to stabilize the sample jet, sample images are acquired at each probe wavelength first, and then the sample flow is turned off, the cell is equilibrated so that no sample is still flowing and then background images are acquired by repeating the probe wavelength scan. This procedure produces a hyperspectral absorbance image in which each pixel contains the absorbance spectrum over the full range scanned.

All data collection is done through an automated program created with LabVIEW software (National Instruments, Austin, TX). The user inputs the range of wavelengths for the QCL to scan, the increment in which to scan that range, the number of images to acquire and average at each wavelength, and a destination folder for the data to be stored. At each wavelength (for both the sample and background scans) a light and dark image is taken. The light image is taken as the laser travels through the sample and on to the detector. A dark image is taken with the shutter closed and no light reaching the sample or detector. The program takes all of the data, averages all images at a given wavelength, subtracts the dark image from the light image, creates a 128×128 matrix of the detector intensities, and drops the newly created file into the desired folder. This occurs for each wavelength scanned and for both the sample and background scans. Therefore, after data collection is complete, there is a minimum of two folders of data created, sample and background images. Once they have been created, all images are analyzed in a separate program. The analysis takes the images and computes the absorbance as described above

at each of the 16384 (128^2) pixels to provide an image of the absorbance values to evaluate in real time. The LabView analysis program was created to be able to observe the absorbance images as they are created in real time. It is very important to be able to preliminarily evaluate the absorbance images in real time due to the fact that few of them contain data worth evaluating further.

Multiple factors can contribute to poor data, the worst of which include unstable sample jets and high noise levels. Frequently, the mixer is not flowing optimally and will cause the sample jet to become unstable or disappear altogether. Sample stability issues can happen for a variety of reasons. The first issue is attributed to air bubbles that are slowly traveling or stuck in one or more of the microchannels. When the sample and sheath solutions are initially attached to the tubing of the mixer, a small gap of air is intentionally placed in the tubing between the old and new samples. This serves multiple important purposes. First, it is evident when the new sample reaches the mixing region because it always follows a stream of air bubbles. Secondly, it prohibits the old and new samples from mixing with each other in the tubing. Ideally, when the new sample reaches the mixing region a stream of air bubbles will pass through with the new sample immediately following. However, air bubbles can sometimes get caught in the channels and not flow through with the rest. This results in a “plug” in the channel. Samples can usually flow around the plug but only at a decreased volumetric flow rate. This inevitably affects the integrity of the flow conditions. If the plug is in one of the side channels, that side of the sheath will be flowing at a diminished flow rate and cause the sample to bend towards that side (figure 3.5). If the bubble is stuck in the center sample microchannel it may prohibit the sample from flowing at all and may not form a jet. Many times the plug

can be forced through the channels by applying short bursts of high flow rates to the specific channel where the plug is located. However, if that method proves unsuccessful, the next option is to take apart the mixer, clean it, and reassemble.

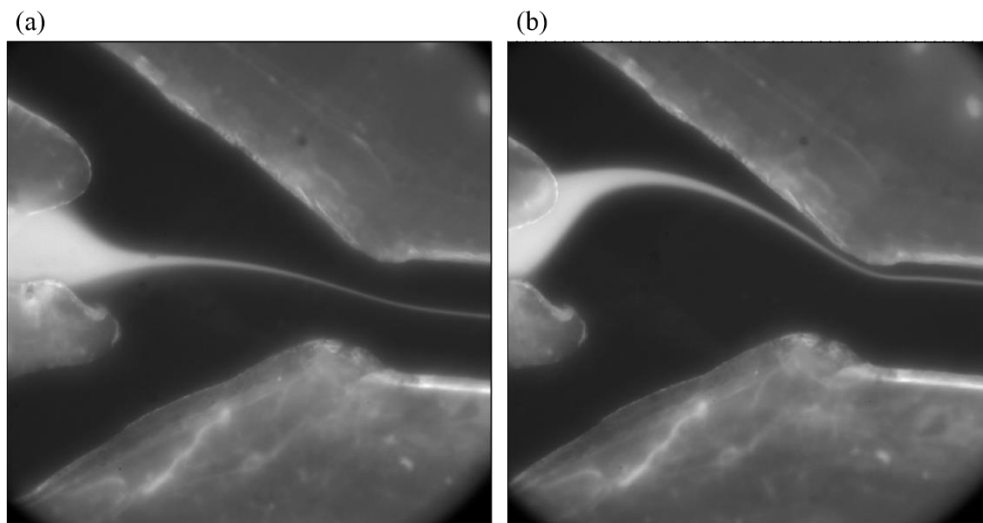


Figure 3.5: An example of what an ideal sample jet looks like versus a sample jet that can result from air bubbles trapped in the side channels. (a) A typical image of an ideal sample jet, flowing directly down the middle of the mixer due to the side channels flowing with equal pressure. (b) The result of an air bubble trapped in a side channel (the top channel in this image) which causes that particular side channel to flow with less pressure compared to the other side and the sample jet to be pushed to the side.

The second reason for flow instability is mixer leaks. Leaking is a problem that is not always immediately evident by observing the flow in real-time, and can be easily mistaken for other more minor complications. Leaking can also occur for a variety of reasons. The two-pieces of metal housing that hold the sandwich style mixer together are attached by screws extending from the top piece to bottom piece. Over time, the screws become very slightly loosened and are unable to keep the necessary pressure on the mixer sandwich to ensure a closed system. When this occurs, sample tends to start leaking out

of the channels and into the solid spacer region. The noticeable result is either diminished flow rates in certain channels or no flow whatsoever. When the metal casing loosens to a point where leaking occurs, the mixer needs to be disconnected from the sample solutions, taken apart, cleaned, and put back together. Another reason for leaking is when the spacer is not optimally aligned with the inlet holes of the CaF_2 window. If the alignment is only slightly off, much of the samples may be directed to the solid spacer region and not the microchannels. The only remedy for misalignment is taking the mixer apart and reassembling.

The third reason for flow instability is slight variations in flow rates of samples. This reason is the hardest to combat because it seemingly happens at random and without cause. Variations in flow rates are most common and easiest to identify when there is a difference between the two sheath (side) flow rates. This results in the focused sample jet being pushed slightly to one side of the mixer, as opposed to forcing a jet down the center. If data is taken with this type of jet, further problems arise during analysis, both when accounting for uneven advective mixing forces, as well as when converting pixels to time. This is due to the fact that the calibration of the mixer, as described elsewhere, was done with a stable and straight sample jet.

If the mixer was operating as desired during data collection, with all channels flowing at their correct flow rates and a focused sample jet flowing down the center of the mixing region, an even larger problem can still affect the data, and that is noise. Noise has always and continues to be a problem with the infrared imaging system. There are, again, multiple sources of noise that have been systematically addressed. The main sources of noise that have been addressed for the infrared imaging system are vibrational

noise, water vapor absorption, and etalon effects.

Both low and high frequency vibrations can be detrimental to an intensity image. Due to the sensitivity of the detector as well as the nature of the absorption calculation, even the slightest vibrations have a large effect on noise levels. The FPA detector is extremely sensitive to external vibrations from sources such as doors closing in the lab or people walking next to the lab table, and are inevitably detected. These vibrations are most observable when strong enough to unsteady the laser beam or shake the apparatus holding the mixer. In order to combat these vibrations, a floating table was installed for the imaging system to rest on. This was able to solve much of the external vibrational noise of the surroundings.

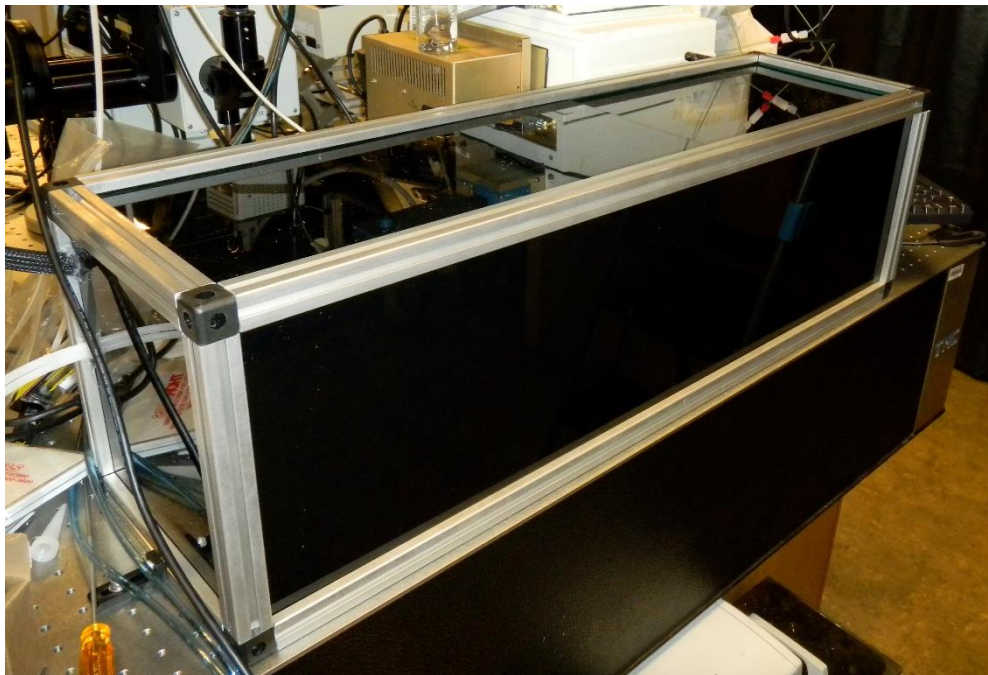


Figure 3.6: Custom-made optics box housing all optics for the infrared imaging system. The top panel slid open so optics and sample were accessible while tubing entered the far left panel to constantly deliver dry air.

The next noise source that has been addressed is artifacts due to the absorption of

water vapor. Water vapor absorbs very strongly in the mid-infrared region of interest for many biological samples ($1500\text{-}2000\text{ cm}^{-1}$)¹²⁰, which is of great importance to this system. Even though the entire building was climate controlled for both temperature and humidity, water vapor (especially during the summer months) was very prevalent in the lab. Therefore, all optical components of the infrared imaging system were housed in a sealed box that was being continuously purged with dry air (figure 3.6). The box was not completely air-tight, but was able to combat the sharp absorbance peaks associated with water vapor.

The last, and most difficult source of noise to combat in the imaging system was etalon effects in the images. In the case of the infrared imaging system, etalon interference occurred when light traveled through two reflecting surfaces and underwent multiple reflections before traveling on to the detector. The infrared light had to travel through one CaF_2 window, then the sample, then finally another CaF_2 before making its way to the detector. Even though CaF_2 has a very high transmission in the mid-IR region, even a few percent of the light intensity being reflected between the windows can cause the periodic interference pattern in the acquired images (figure 3.7). Etalon effects were not always present in the images collected but would occur seemingly at random. Therefore, when computing the absorbance between a sample and background image if one of the images had etalon interference while the other did not or had a different pattern, very large noise values resulted in the absorbance image.

Many tactics were used to combat the etalon effects with variable degrees of success. First, a germanium (Ge) window replaced the bottom, undrilled CaF_2 window in order to create large differences in refractive indices of the windows to interrupt the

reflection patterns. This change was able to diminish the etalon effect but not completely eliminate it. It seemed to decrease the frequency in occurrence of etalon patterns and therefore decrease the chance of pairing two differently patterned images together to calculate the absorbance image, but the magnitude of the etalon patterns did not seem to decrease.

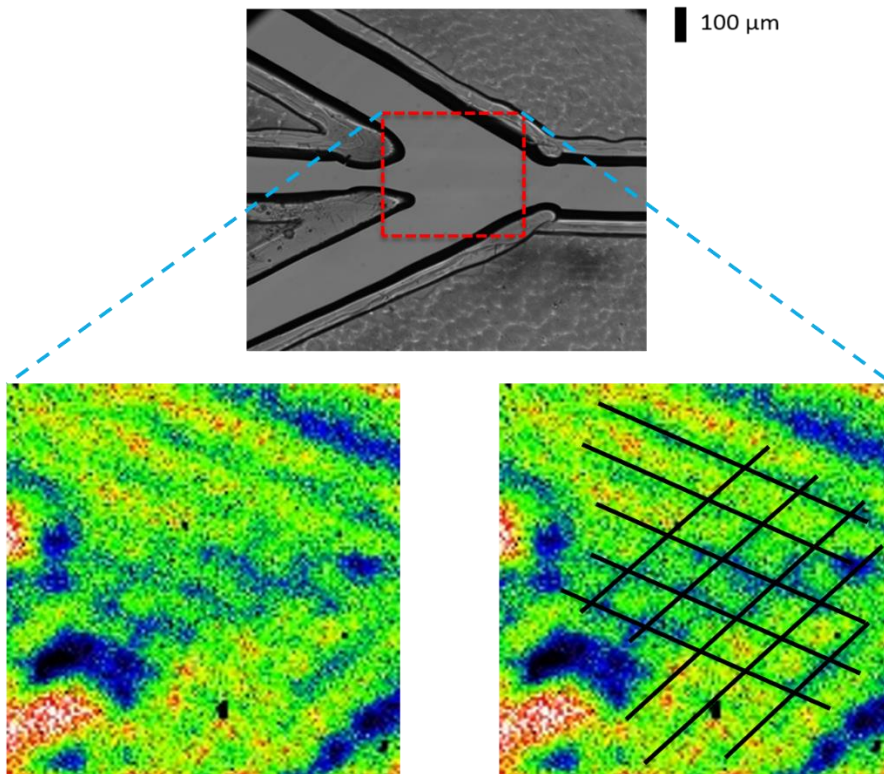


Figure 3.7: Images from the infrared array detector exemplifying the etalon effect plaguing acquired images. The top image is a brightfield image of the mixer with a box around the region imaged in the infrared array detector below. Both bottom images are identical except for the solid lines on the right image that were applied over the main etalon patterns through the middle of the mixer. A dark blue to black color represents areas of low transmittance. The mixer edges are well defined by low transmittance as well as the sample jet flowing left to right. Green to yellow to red colors represent areas of high transmittance and are mostly located in the sheath flow and outside the mixing region.

The next approach was developed based on the fact that etalon effects tend to be strongest when the light traveling through two reflecting surfaces is a coherent source. Diffusers are commonly used to eliminate coherence of a light source and are very common in the visible light region. However, mid-IR diffusers are less commonly developed. Both homemade and commercial diffusers were used in the imaging system with little success. In order to make the homemade diffusers, a CaF₂ window was polished with an alumina suspension that contained 1 μm alumina spheres. The commercial diffuser was a sandblasted CaF₂ window. Although these diffusers were successful in eliminating the coherence of the source, the main drawback was the amount of intensity lost when the beam traveled through the diffuser. The light enters the diffuser collimated but due to the nature of a diffuser, the output is extremely diffuse light. Even with a collimating optic placed immediately after the diffuser to collect all incoherent light, the amount of light that reached the detector was far less than without the diffuser. It was determined the cons outweighed the pros with the diffuser and was not permanently implemented. Because of this, the etalon effects continue to be a source of noise that has not been completely eliminated.

The next step after the development of the imaging system was complete, was to utilize the system in order to follow a reaction occurring with a biological sample. This would help prove the applicability of following enzymatic reactions with microfluidic mixing and infrared spectroscopy.

Section 3.4 Application of infrared imaging system

The characteristics and capabilities of the infrared imaging system were

demonstrated with both mixing experiments and computer simulations. The mixing experiments included a fast pH jump (since the experiment is conducted in D₂O with deuterated buffer, it is actually a “pD jump”) detected using a biologically relevant infrared “pD indicator”, adenosine monophosphate (AMP), and an H₂O/D₂O mixing experiment that follows the diffusion of water. The latter experiment allowed for direct comparison of the mixer performance to predictions from a simulation.

For the following experiments, adenosine monophosphate (AMP) was purchased from Sigma-Aldrich (St. Louis, MO) and dissolved in D₂O (Cambridge Isotopes, Tewksbury, MA) at a concentration of 25 mg mL⁻¹ for both equilibrium FTIR and IR mixing experiments. The pD of the AMP solution was adjusted with DCl solution (Sigma-Aldrich). Equilibrium FTIR data were acquired on a Varian 660-IR spectrometer. For mixing experiments, the pD of the AMP solution was adjusted to a starting point of 3.2. A sheath solution of 250 mM phosphate buffer at pD 6.9 was used to induce a pD jump. Data were collected with the AMP sample flowing at 0.60 μL min⁻¹ and each side flowing at 17 μL min⁻¹. Spectra were collected from 1600–1680 cm⁻¹, with detailed pD analysis occurring at 1624 and 1666 cm⁻¹, corresponding to intense IR absorbance peaks of AMP.

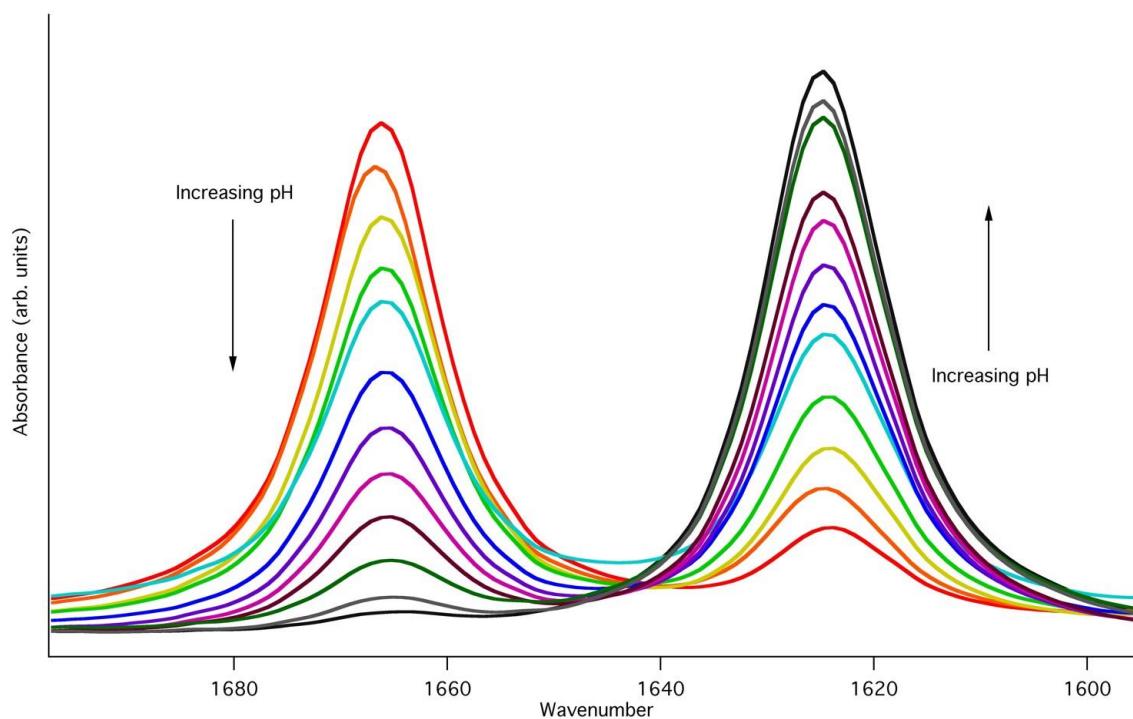


Figure 3.8: Equilibrium FTIR spectra of AMP. As the pH of AMP increases the peak at 1624 cm^{-1} grows in while the 1666 cm^{-1} peaks diminishes away.

The AMP pD jump experiment was successful in being able to both display a biological application of the infrared imaging system and also establish the mixing time for the mixer at the same time. The mixing time of the IR microfluidic system was characterized by measuring the time to achieve a pD jump of about 3 units, using AMP as an infrared pD indicator. Since protons or deuterons diffuse more rapidly than most molecules, a pD jump should represent a lower limit of the mixing time for the specific configuration of the system (sample and sheath flow rates and jet size). In addition, since many biomolecular reactions can be initiated by a change in pD (such as an enzyme reaction or protein folding), these experiments demonstrate the feasibility of this approach. The mixing is observed as an exponential decay of the deuterium concentration

in the focused region and therefore the total mixing time is reported as the 1/e time of the fit, plus the “dead time” represented by the pre-focused region (see below). AMP is an ideal infrared pD indicator, because it has an infrared spectrum that is strongly dependent on pD in a biologically relevant range. It has two strong and clearly resolved IR absorbance bands at 1666 and 1624 cm^{-1} , corresponding to the protonated and deprotonated states of the adenosine ring, respectively.⁹⁵ The pKa for this transition occurs at 3.8 (or 3.4 in pD units, as applicable in this study).¹²¹ The equilibrium FTIR spectra (figure 3.8) show the pD dependence of these modes. The 1624 cm^{-1} mode has previously been assigned to the ring C=N stretching vibration of neutral adenosine. At low pD, this band shifts to higher frequency as expected for protonation of the ring structure.^{95,122} Thus, the relative intensity of these two bands is an indicator of the solution pD; for the protonated (or deuterated) adenosine ring structure below pD 3.4, the absorbance at 1666 cm^{-1} dominates, but as the pD shifts up towards neutral, the 1624 cm^{-1} peak instead becomes dominant. A titration curve was created by measuring the FTIR spectrum of AMP in D₂O as a function of pD (figure 3.X1) and determining the ratio of the integrated absorbance of the 1666 and 1624 cm^{-1} peaks (figure 3.9). Using a ratiometric method removes the dependence of the absorbance on the total concentration of AMP, which is necessary because the AMP concentration is continuously changing in a mixing experiment, due to diffusion of AMP out of the sample stream. The normalized absorbance data are related to the pD and pKa by equation 3.2.

$$\frac{A_{1666\text{cm}^{-1}}}{A_{1624\text{cm}^{-1}}} = \frac{[D^+] + c_1 K_a}{c_2 [D^+] + c_3 K_a} \quad (3.2)$$

A pD jump is generated by flowing an AMP solution initially at pD 3.2 through a sheath buffer at neutral pD. The buffering capacity of the sheath solution (250 mM

phosphate) is more than sufficient to raise the small volume of the AMP sample stream to a final pD that equals the starting sheath buffer pD. The AMP is dissolved in pure D₂O (no buffer), to minimize the intrinsic buffering capacity of the sample. The rate of “deprotonation” (deuteron dissociation) of the acid form of AMP is fast compared to the rate of the pD jump (set by the diffusion-limited equilibration of the deuteron concentration in the sample stream with the surrounding sheath buffer, see below). Therefore, the lifetime of the AMP IR absorbance change is attributed solely to the mixing time of the system (the pD jump) rather than the “deprotonation” reaction itself.

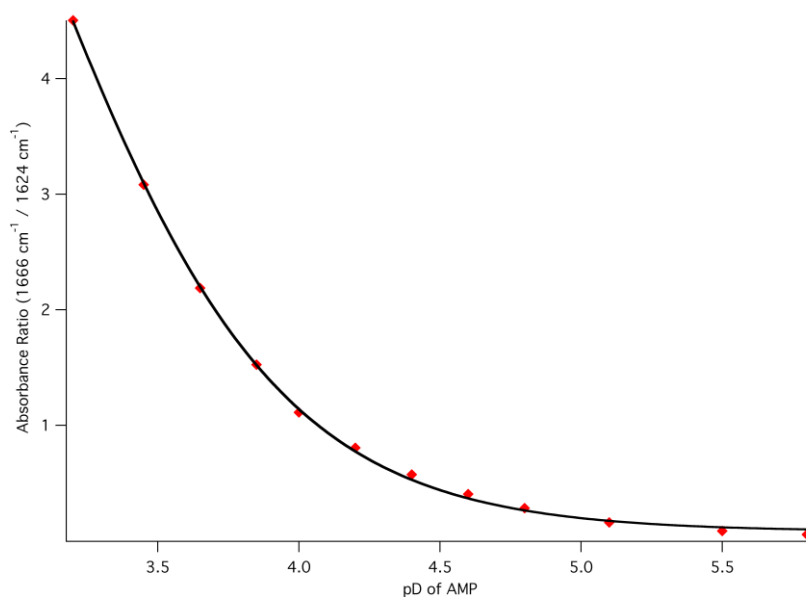


Figure 3.9: Experimental data of absorbance versus detector pixel number for images at 1666 cm⁻¹ (circles) and 1624 cm⁻¹ (squares). These show what was commonly obtained when completing the AMP pD jump experiment. The 1666 cm⁻¹ peak’s absorbance stays relatively constant during the pre-focused region, then decays very rapidly once the sample jet is hydrodynamically focused because of the pD jump in the experiment, as well as the natural decay of the concentration seen in every flow experiment. The 1624 cm⁻¹ peak’s absorbance stays relatively constant during the pre-focused region as well but then rapidly jumps up in absorbance as is expected with the pD increase in the sample. After the sharp increase, the absorbance appears to stay relatively constant because of the

increase in absorbance due to the pD jump being offset by the natural decay of absorbance (concentration) seen in every flow experiment.

Figure 3.10a shows the AMP IR absorbance spectra at three separate pixels located in the sample jet at various distances downstream from the merge point of the sample and side flows. A slow side flow rate of $13 \mu\text{L min}^{-1}$ was used for this acquisition to test the mixer performance at long times, resulting in a relatively slow pD jump. The top spectrum (diamonds) is from a pixel located in the pre-focused region at roughly 1 ms in time after the merge point of the three channels; since the peak at 1666 cm^{-1} is still dominant, not much mixing of the sample and sheath has occurred and the pD remains close to its starting point of 3.2. The middle spectrum (squares) is located in the focused region, over 3 ms from the merge point, at a pixel where mixing has started to occur. Mixing is evident from the shift in relative intensity of the two peaks, with the nearly equal intensity of the 1666 and 1624 cm^{-1} peaks indicating a jump past the pKa of AMP, to an approximate pD of 4. Lastly, the bottom spectrum (circles) corresponds to a time of over 5 ms from the merge point. The concentration of AMP has been diluted by diffusion of AMP out of the sample stream, causing the overall absorbance to decrease. Nevertheless, it is clear that the 1624 cm^{-1} peak is now the largest peak and the pD jump has progressed closer to neutral pD.

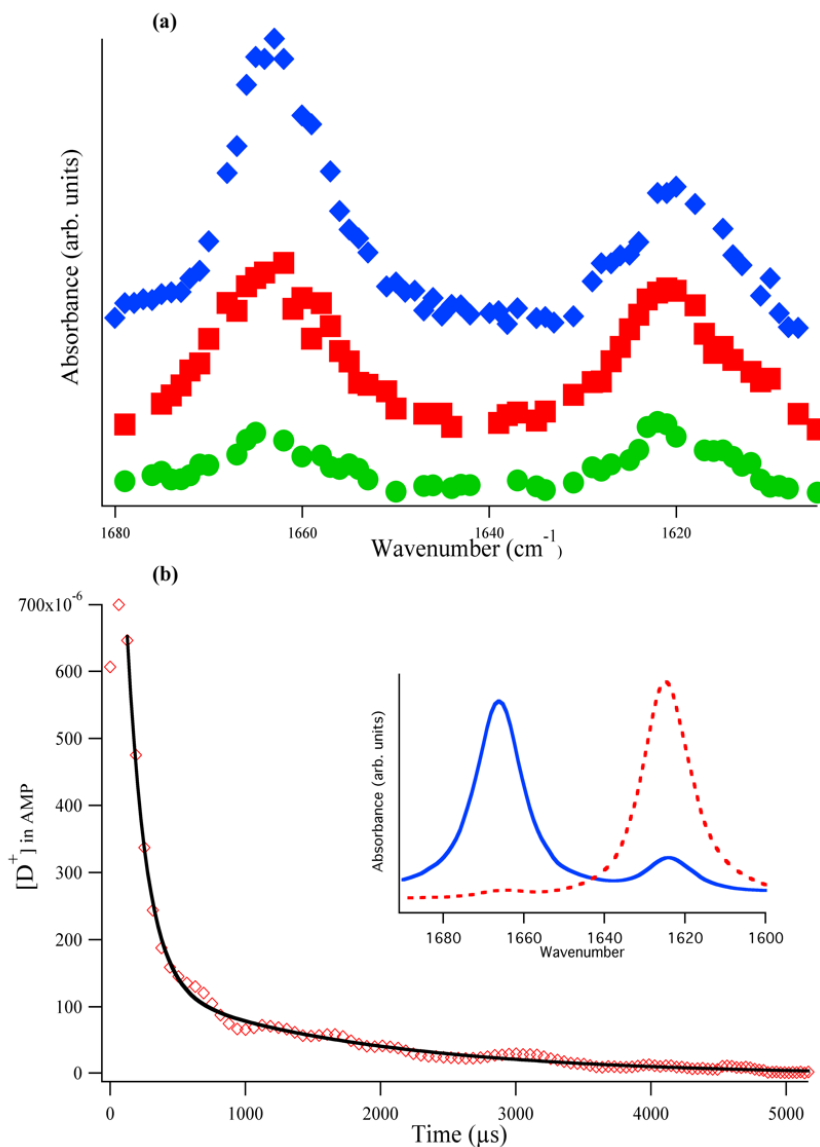


Figure 3.10: AMP pD jump experiment (pD 3.2 AMP sample solution and pD 6.9 250 mM phosphate sheath flow): (a) IR spectra of AMP at three different locations along the sample jet for a sample flow rate of $13 \mu\text{L min}^{-1}$ (offset vertically for clarity). The IR image of the jet is shown in the inset with the approximate location of the three spectral traces indicated by the respective symbols. In the pre-focusing region (diamond), little mixing has occurred because the 1666 cm^{-1} peak remains dominant. At the downstream positions, the relative peak amplitudes change, indicating the rise in pD. The overall absorbance also decreases, due to diffusion of AMP out of the sample stream. (b) AMP pD jump plotted as $[\text{D}^+]_{\text{in AMP}}$ versus time (diamonds; average of 20 separate jumps). The pre-focused region (first three points) represents the dead time ($127 \pm 6 \mu\text{s}$) of the mixer, with

very little mixing occurring in this region. Efficient mixing occurs in the focused region, evident by the sharp decrease in $[D^+]$, which is fit to a biexponential decay (see text). Inset: equilibrium FTIR spectra of AMP at pD 3.2 (solid trace) and at pD 5.8 (dashed trace).

The limit of the mixing time was measured by generating a pD jump using a fast sheath flow rate of $17 \mu\text{L min}^{-1}$, as shown in figure 3.10b (faster sheath flow rates are possible, but the small jet size produced makes it difficult to detect the AMP absorbance). The pD of the sample solution as a function of time is determined using a multi-step analysis of the data. After using Beer's law to determine the absorbance at each pixel in the IR image, an image line profile analysis is used to obtain the absorbance at each pixel along the sample jet. This analysis selects the sample path in the image plot, to follow the z-axis values (absorbance) versus either the x- or y-axis values (distance in pixels along the jet). This analysis is repeated for each probe frequency. Next, the ratio of the absorbance profiles at 1666 and 1624 cm^{-1} is computed and then converted to pD using the FTIR calibration. The outcome is the pD profile versus pixel number along the jet. Finally, pixel number is converted to time using the calibration described above, yielding the pD or $[D^+]$ versus time as shown in figure 3.10b.

There are two key features evident in the time dependence of $[D^+]$ for the pD jump shown in figure 3.10b. First, there is the region immediately after the three inlet channels meet at the merge point (time = 0), where the sheath solutions are acting to hydrodynamically focus the sample to a thin jet (pre-focused region). The sample is squeezed from its starting width of approximately $110 \mu\text{m}$ to less than $20 \mu\text{m}$ within the first few time points. As is evident in figure 3.10b, the deuteron concentration in the

AMP sample stays relatively constant for the first $127 \pm 6 \mu\text{s}$, indicating that little mixing occurs in the prefocused region. Since these early time points are measured at the center of the pre-focused sample flow, they do not account for any mixing that occurs at the sample/sheath flow interface. Therefore, these early time points represent the “dead-time” of the mixer. After the pre-focused region, the deuteron concentration decays rapidly; this decay was fit with a biexponential function with lifetimes of $142 \pm 16 \mu\text{s}$ (90%) and $1.6 \pm 0.1 \text{ ms}$ (10%). The primary ($142 \mu\text{s}$) phase is due to the dominance of the advection process at early times, as the sample and sheath flows come together, whereas the slower small amplitude phase is dominated by diffusion of deuterons out of the focused sample stream. Since 90% of the pD jump occurs in the first phase, we use its lifetime of $142 \mu\text{s}$ to characterize the mixing time. The pD is raised from its initial value of 3.2 to over 4.5 within this fast phase of the jump. The dead-time of $127 \mu\text{s}$ was added to the fast phase decay time to yield an overall mixing time of $269 \pm 16 \mu\text{s}$. The total error reported here originates from the calibrations of the time per pixel and the deuteron concentration, and is propagated through to the time domain. To our knowledge, this experimental mixing time is the shortest reported for any microfluidic mixer that utilizes IR spectroscopy to probe the reaction progress.

In addition to the AMP pD jump mixing experiment, the mixing of an H_2O sample into a D_2O sheath flow because it represents a simple mixing process in the absence of any chemical reaction. This mixing experiment serves as a model system for comparing experimental results with the predictions of a simulation using COMSOL Multiphysics software to model the mixing. As previously described, a laminar flow, stationary study using transport of dilute species was carried out in order to simulate how

a sample would mix with the sheath solution. Within the mixer, the flow velocity is dictated by the incompressible Navier–Stokes equation (equation 2.2) while the concentrations of each reactant is governed by Fick’s Law, described by the diffusion and convection equation (equation 2.3). This mixing experiment was chosen to be simulated instead of the pD jump experiment due to the fact that the molecular diffusion of water can be modeled in a straightforward way using Fick's law, whereas proton (or deuteron) diffusion is a more complex process that is still of research.¹²³ Simulations were carried out using the diffusion coefficient of water molecules, $D = 2.2 \times 10^{-9} \text{ m}^2\text{s}^{-1}$,¹²⁴ for direct comparison with the H₂O/D₂O mixing experiments. Other parameters used in simulation can be found in Table 3.1.

Table 3.1: Parameters for theoretical modeling in COMSOL for H₂O/D₂O mixing experiment

Parameter	Value/Setting
Diffusion Coefficient	$2.2 \times 10^{-9} \text{ m}^2/\text{s}$, isotropic
Sample flow velocity	0.0013 m s^{-1} (for $0.60 \text{ } \mu\text{L min}^{-1}$)
Sheath flow velocity	0.0270 m s^{-1} (for $17 \text{ } \mu\text{L min}^{-1}$)
Material	Water, liquid
Inflow sample concentration	100 mM
Inflow sheath concentration	0 mM

The H₂O/D₂O mixing experiment used a strongly absorbing H₂O sample flowed through a D₂O sheath solution at 0.60 and $17 \text{ } \mu\text{L min}^{-1}$, respectively. Since the water IR absorbance is strongly shifted by isotope substitution, a single probe frequency at 1636 cm^{-1} was sufficient to fully characterize the H₂O/D₂O mixing, even though the IR spectrum is broad and featureless in this region. The mixing of the H₂O sample stream

with the D₂O sheath is observed as an exponential decay of the H₂O IR absorbance as shown in figure 3.11a (diamonds, left axis). The COMSOL simulation of the mixing is overlaid on the experimental points (line, right axis). The simulation predicts the concentration of H₂O in the sample stream as a function of time, where the concentration is initially 100% before mixing with the side channels, but then decreases through the processes of diffusion and advection. The COMSOL simulation used the actual geometry and dimensions of the mixer (figure 3.11b) as well as the flow velocities calculated from the volumetric flow rates and other relevant simulation parameters (table 3.1). The simulation closely matches the experimentally observed mixing process. The same dead-time of about 550 μ s is observed for the pre-focused region in both the experiment and simulation. The exponential decay of the H₂O concentration in the focused region has a lifetime of $934 \pm 46 \mu$ s for the experiment, and $908 \pm 28 \mu$ s for the simulation, again in good agreement. Combining the dead-time and exponential decay time yields a total mixing time of approximately 1.5 ms. This mixing time is much slower than the AMP pD jump, in part due to the faster diffusion of deuterons compared to water, but also because the pD jump experiment used a higher sheath flow rate, resulting in stronger advective mixing and a tighter focus of the sample stream hence a shorter diffusion distance.

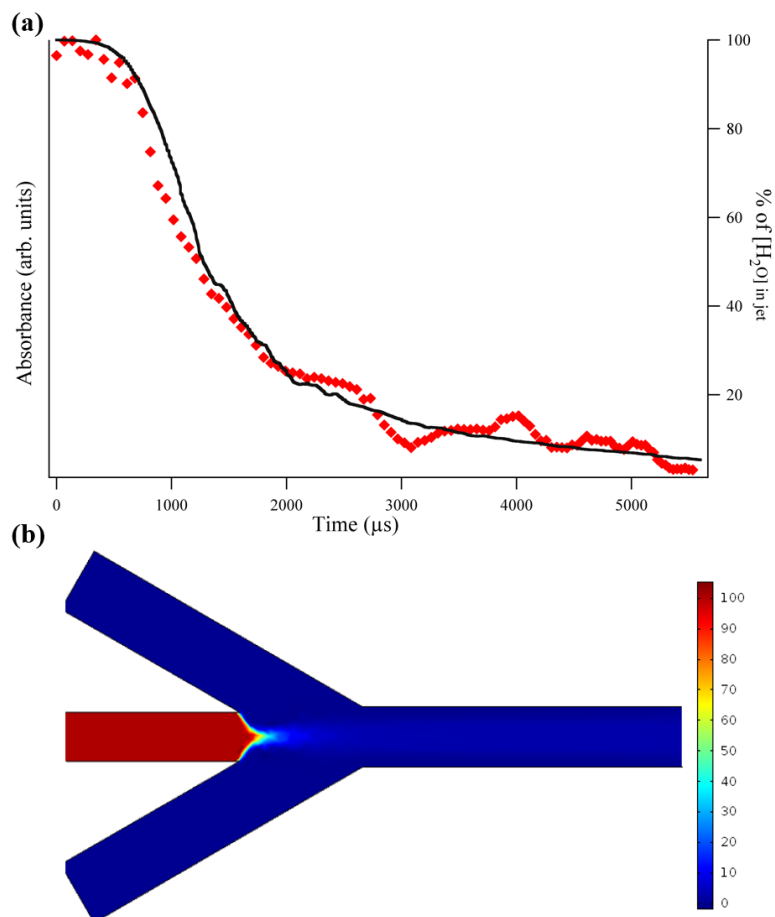


Figure 3.11: Comparison of experimental results and simulation of H₂O/D₂O mixing: (a) IR absorbance decay of H₂O sample mixing with D₂O sheath solution monitored at 1636 cm^{-1} (diamonds, left axis). The data are the average of four separate acquisitions. The solid line (right axis) is the COMSOL simulation of the mixing using mixer dimensions, flow rates, and diffusion coefficients that mirror the experimental conditions. (b) Surface plot from the COMSOL simulation showing the concentration of the H₂O sample. The H₂O is hydrodynamically focused into a jet and mixes by advection and diffusion with the D₂O sheath solution, evident by the drop in concentration of the H₂O in the sample stream.

A rapid decrease in the H₂O concentration in the sample jet is observed in both the experiment and simulation. The timescale for this decrease is too short to be simply a

consequence of diffusional mass transport and therefore must have a large contribution from advective forces acting on the jet.⁵⁴ This effect can be explained further with the advection–diffusion equation that describes the evolution of the concentration of a solute, c , as:

$$\partial_t c = -v \cdot \nabla c + D \nabla^2 c \quad (3.3)$$

where the solute with molecular diffusion constant is moving in a solvent with velocity, v . After this equation is made dimensionless, it is evident that for a fluid flow with a characteristic length of L and a velocity, V , the molecular diffusion term of equation 3.3, $D \nabla^2 c$, is dominant for systems with a small Peclet number ($Pe < 1$) where $Pe = VL/D$. On the other hand, when $Pe \gg 1$, the advection term becomes dominant. When applied to our mixer, even when the three channels initially merge and the velocity is at its lowest, the Peclet number is still much greater than one, putting it well into the advection-dominant regime.⁵⁴

The advection process has important consequences for microfluidic mixing experiments with proteins. Conceptually, these experiments rely on slow diffusion of a protein out of the sample stream compared to diffusion of a reacting substrate into it, such that the protein concentration in the sample stream remains high. In real mixers, however, advection complicates this process because it reduces the protein concentration in the sample stream. The concentration decreases more quickly as the sheath flow rate is increased and advection becomes stronger (figure 3.12). Therefore, a balance must be achieved between a high sheath flow rate, in order to decrease the mixing time, and a flow rate that is slow enough to maintain a sufficient concentration of the sample in the jet during the entire time course of the reaction. The latter depends on the initial

concentration and the detection limit of protein signal being monitored. This balance was the basis of choosing a sheath flow rate of $17 \mu\text{L min}^{-1}$ for the $\text{H}_2\text{O}/\text{D}_2\text{O}$ mixing experiment, rather than $25 \mu\text{L min}^{-1}$, even though in principle a faster mixing time is obtainable. Clearly, the ultimate limit will be determined by the sensitivity of the IR absorbance detection method, which has yet to be fully optimized.

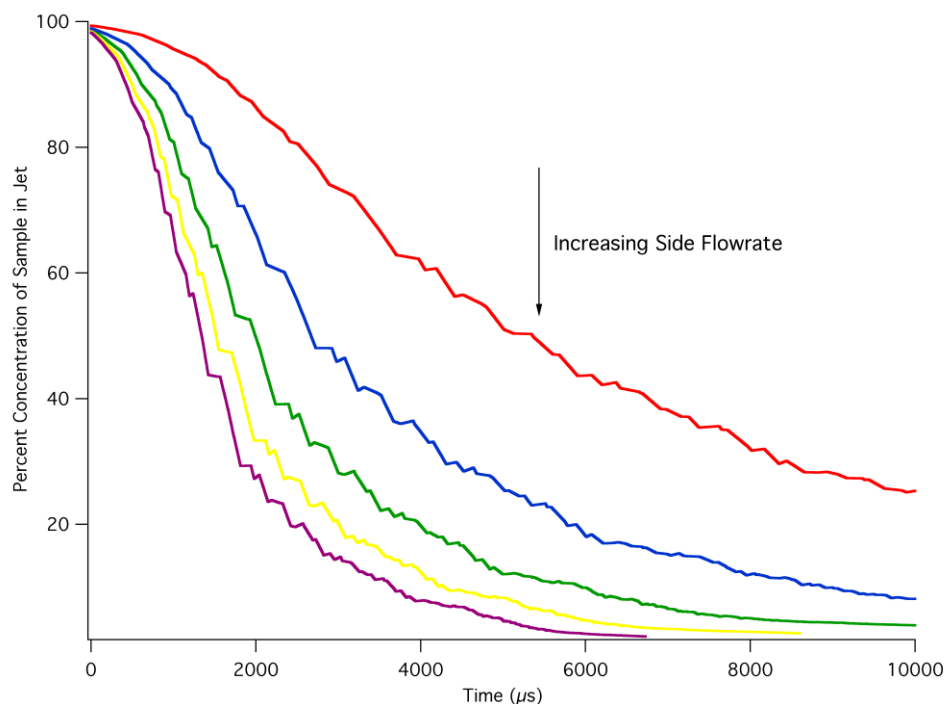


Figure 3.12: Simulated concentration decays versus time computed with COMSOL. The different traces correspond to different side flow rates where the red, blue, green, yellow, and purple traces correspond to 5, 10, 15, 20, and 25 $\mu\text{L min}^{-1}$ side flows, respectively. The slower the flow rate, the longer the sample stays in the jet but the fatter the jet and subsequently the longer the mixing time. Contrary, the faster the flow rate, the faster the sample and sheath solutions mix, but also the concentration decreases more rapidly.

A continuous-flow, microfluidic mixing system utilizing mid-IR hyperspectral absorbance imaging to monitor reaction progress, with a sub-millisecond mixing time was developed and characterized through the described experiments. The mixer uses a

simple sandwich configuration of a laser machined polymer spacer in between two IR transparent windows to create a laminar flow, hydrodynamically focused, closed channel mixer. The mixer and infrared imaging system were experimentally calibrated in order to establish a time per pixel based on flow rates and position within the mixer. The mixing time and feasibility of the mixer for studying biomolecular reactions were then established through an AMP pD jump experiment. An acidic AMP sample was mixed with a neutral phosphate buffer to induce a pD jump through the pKa value of AMP, while following two IR absorbance peaks in the 1600 cm^{-1} region corresponding to the two protonation states. Lastly, an $\text{H}_2\text{O}/\text{D}_2\text{O}$ mixing experiment was used to follow the absorption decay of the water at 1636 cm^{-1} and to model that decay with computational simulation. The simulation matched well with the experimentally obtained data.

The reported mixing time of $269 \pm 16\ \mu\text{s}$, is the fastest experimental mixing time to date of any microfluidic mixing system that uses IR spectroscopy for detection of the reaction progress. Using IR spectroscopy alleviates any need for fluorescence labeling, and so avoids the inherent problems of appending large reporter dyes to the biomolecules of interest. Infrared absorbance of a protein or its substrate or both can be followed through the time course of a reaction using this approach. The connection of IR spectra with specific structural features, such as the protein amide I vibration makes this approach widely applicable to biological reactions such as protein folding and enzymatic reactions.

Section 3.5 Modifications to infrared imaging system

Before designing the homemade infrared imaging system as described above, the

lab was already in possession of a Varian 600 Series FTIR microscope (Agilent Technologies, Inc., Santa Clara, CA). This microscope was used in the first attempt to implement microfluidic mixing with an infrared imaging system. The main drawback with this system was found to be the original objectives in the microscope. They were old and in less than fair condition, but mainly, their design did not allow for a small diameter laser beam, like that of the QCL, to be effectively magnified and directed towards the detector. Instead, there was a solid metal piece situated directly in the middle of the objective. The images collected with these objectives had the pattern of that solid metal piece directly in the middle of the image, rendering the image useless. At the time the microscope was being used, infrared objectives were not routinely produced so there was no option to simply purchase another objective that was more suited for our system. Therefore, the decision was made to build the homemade system.

There were, however, multiple structural shortcomings in the homemade system that needed to be fixed. Shortcomings like the ability to easily move the mixer in the x- and y- directions to obtain an image of the correct section of the mixer, as well as the z- direction to ensure the mixer was in focus. It was a very tedious process to get the short focal length lens in the exact spot to both keep the mixer in focus and direct the magnified image through towards the detector, as opposed to having a standard focusing knob like is found on any microscope. Furthermore, there was always the difficult task of keeping the mixer fasted securely so it would not shift positions from scan to scan. This is one of the most important tasks when taking data because of how the entire image is used to calculate absorbance values. If the mixer shifts position even a few microns in any direction between scans, the sample and background images will not align correctly

resulting in useless data.

At about the same time as these problems were being addressed on the home built system, a mid-IR objective was newly available, and so it was decided to convert back to using the infrared microscope. The objective (Edmund Optics Inc., Barrington, NJ) was made with ZnSe glass and was fully transmissive in the mid-IR. Other than a useful objective, the microscope already had all other necessary optics and mechanisms to use in the way that was desired. Therefore, with the addition of the new objective the microscope was more ideal to use than the previously built imaging system.

The optical setup for the infrared microscope with an external source is fairly simple. The QCL was set up outside of the microscope along with a mirror to direct the beam inside the back section of microscope as well as the shutter used for the same purpose as before. Once the beam was inside the microscope, a series of mirrors directed the beam down towards the base of the microscope and forward towards the front. Another mirror sent the beam up through the sample as a collimated beam. After the laser traveled through the sample it passed through the objective which effectively magnified the image the entire way until it reached the detector. The final image had a magnification of approximately 14x.

Using the infrared microscope vastly improved the stability of the mixer and thus the image, being that it now had a stage to sit on securely. Additionally, the xy-stage allowed for easy movement of the mixer and the focusing knob was a much easier way to focus the image. Modifications were made to the metal casing of the mixer in order to lower the objective as close to the mixer sandwich as possible due to the short working distance of the objective. The mixer also had to lay upside down on the stage in order to

keep the Nanoports and tubing out of the way of the objective. Reverting back to the IR microscope has proven to rectify many of the shortcomings of the homemade imaging system and continues to be the best option. There still is not, however, a good method to combat the etalon effect that is still visible randomly in acquired images. Further work would include solving the etalon interferences as well as applying an enzyme flow experiment to the imaging system.

Chapter 4: Application of microfluidic mixing to enzymatic reactions

Section 4.1: Introduction to biological kinetics methodology from micro- to milliseconds

Microfluidic mixing has a plethora of applications that are already well established and have been discussed previously. The main goal of developing microfluidic mixing capabilities in our lab was to ultimately study enzymatic reactions. A technique that could use multiple spectroscopic probes depending on whatever was necessary to follow specific processes on timescales ranging from hundreds of microseconds to a few milliseconds would greatly increase the capabilities of the lab.

Microfluidic mixing could have different benefits when compared to other established techniques known for their viability of studying enzymatic reactions on fast timescales. Two such techniques that are abundantly used in the literature are stopped-flow¹²⁵⁻¹²⁷ and relaxation methods, like laser-induced temperature-jump.¹²⁸⁻¹³⁰ The stopped-flow technique is a simple concept that has been used since the 1950s.¹³¹

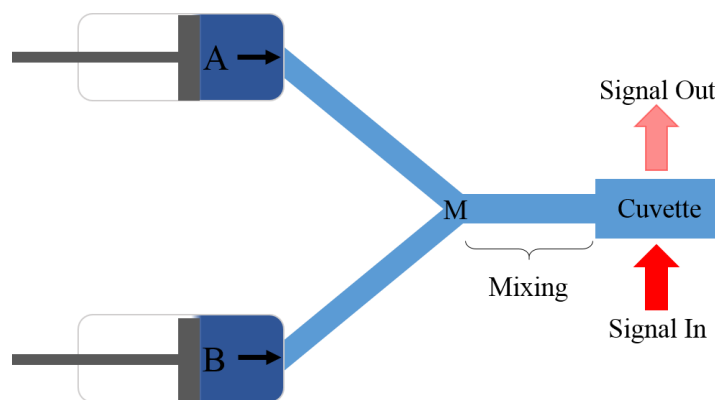


Figure 4.1: Schematic of a stopped-flow instrument. Two samples, A and B are injected by syringe into a mixing region, M, then flow into the cuvette where they are stopped abruptly and mixed. Once mixed, spectroscopic signals can follow kinetics.

Samples from syringes are injected into a small mixing chamber at high velocities. In that chamber the flow is abruptly stopped and turbulent mixing between the sample solutions occur, and only then can kinetics be studied (figure 4.1).¹³² Stopped-flow has been combined with a variety of spectroscopic signals to follow reaction kinetics like UV/visible absorbance, fluorescence emission, circular dichroism, infrared, and electron paramagnetic resonance. Any signal that can be measured through a cuvette is applicable to stopped-flow. The timescales on which chemical kinetics can be studied with stopped-flow depends solely on the dead-time of the instrument. That is, the amount of time the instrument requires to homogeneously mix the samples, which is analogous to the mixing time in microfluidics. Typically, dead times are on the order of a few milliseconds but have recently decreased to 1 ms or slightly less due to miniaturizing instrumental components.¹³³ Stopped-flow has the advantages of relatively small sample consumption, ease of use, and the ability to study reactions that start as reactants end as only products. However, even though stopped-flow consumes a small amount of sample compared to large scale reactors, instruments typically still require amounts on the milliliter volume scale, which can be costly for precious samples. Furthermore, the dead-time is a continual drawback that limits the applicability of these instruments to studying kinetics on very fast timescales.

Relaxation techniques, on the other hand, measure the response to a shift in equilibrium of a reversible reaction. This is contrary to methods like microfluidic mixing and stopped-flow which follow reactions from reactants all the way to products. One such technique to shift the equilibrium of a reaction utilizes jumping the temperature of a system, initiating a new thermodynamic equilibrium, called T-jump. A system is poised

at a certain equilibrium, then the environment of the system changes due to a form of perturbation (like the temperature increase) and finally relaxes to a new equilibrium. Typically, the equilibrium is only slightly changed from the initial state and therefore the kinetics observed are of systems in an equilibrated state similar to the initial equilibrium. The timescales on which relaxation methods can measure depends on the time it takes the perturbation to be created as well as the duration of the perturbation and can ideally range from 10^{-4} to 10^{-11} seconds.

Furthermore, the observed rates are a complex combination of the microscopic rate constants for both the forward and reverse processes involved in reestablishing equilibrium.¹³⁴ The kinetics produced can understandably be more complicated than other techniques due to the fact that both directions are occurring while the system is reestablishing equilibrium. The signal will ultimately contain a number of relaxation rates related to the number of reaction states in the entire equilibrated system. Though this can become quite complicated for branched and cyclical pathways, careful experimental conditions can force the kinetics to be dominated by a single rate constant.

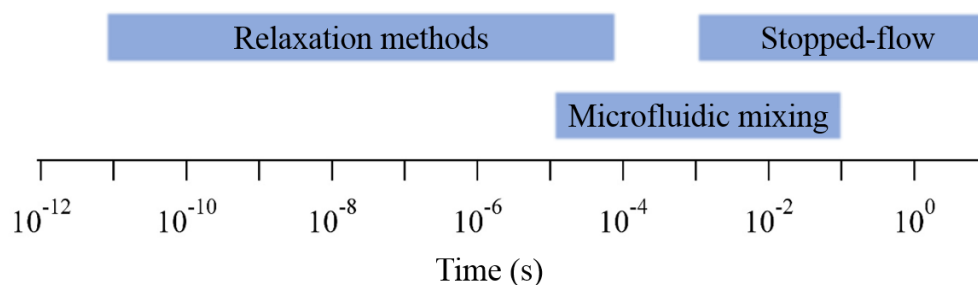


Figure 4.2: Accessible timescales for relaxation methods, stopped-flow, and microfluidic mixing, as described throughout this work.

Both stopped-flow and relaxation techniques have been used extensively to study the kinetics of enzymatic reactions. However, there is a void to fill in the timescales that are readily accessible to these techniques (figure 4.2). Microfluidics, as described extensively before, can provide the accessibility to those timescale gaps.

Section 4.2: Introduction to DHFR catalysis

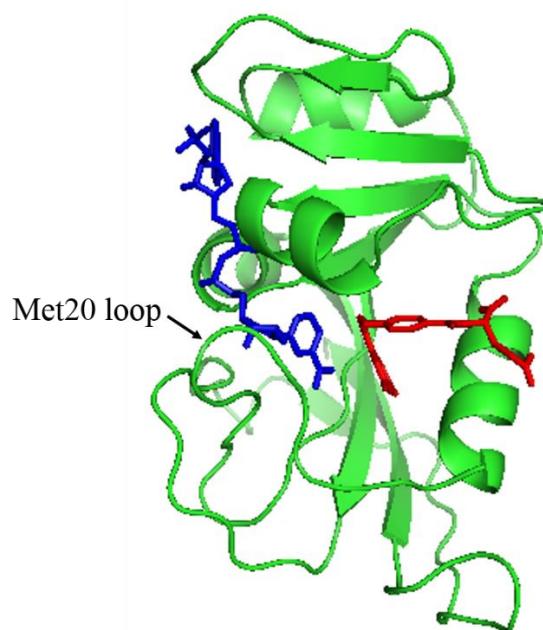


Figure 4.3: Crystal structure of DHFR. Cofactor NADPH is colored blue and one of the substrates, folate, is red. Also, the Met20 loop is labeled. The Met20 loop is in the closed confirmation in the ternary complex. PDB: 1RX2.

Dihydrofolate reductase (DHFR) (figure 4.3) catalyzes the stereospecific reaction of 7,8-dihydrofolate (DHF) to 5,6,7,8-tetrahydrofolate (THF) facilitated by the cofactor NADPH (figure 4.4). The DHFR catalyzed reaction is biologically important due to THF being a precursor for the biosynthesis of thymidylate, purine nucleotides, and some

amino acids, thereby making DHFR a cancer drug target.¹²⁵ Furthermore, and more important to the current research, DHFR has served as a model system to study the relationship between enzyme structure, catalysis, and dynamic processes that contribute to catalysis.¹³⁵⁻¹⁴⁵ During catalysis, DHFR transfers a hydride from NADPH to C6 of the pterin ring in DHF while a proton is transferred from either solvent or an adjacent residue to N5 position of the pterin ring.^{125,146} DHFR from *E. coli*, like the version studied here, contains a number of mobile loops that are involved in the catalytic cycle. Movements of the Met20 (residues 9-24), FG (residues 116-132) and GH (residues 142-149) loops cause DHFR to switch between closed and occluded conformations during catalysis.^{135,137} Upon binding of the substrate and cofactor, the Met20 loop closes over the active site (figure 4.3) by forming hydrogen bonds with the FG loop resulting in an optimal environment for hydride transfer.^{137,147} After catalysis, in which THF is produced, the Met20 loop opens to release the nicotinamide ring of the oxidized cofactor and also makes new hydrogen bonds with the GH loop. This allows the exchange of NADP^+ with NADPH and eventually for the rate-limiting step of product release (figure 4.5).¹³⁷

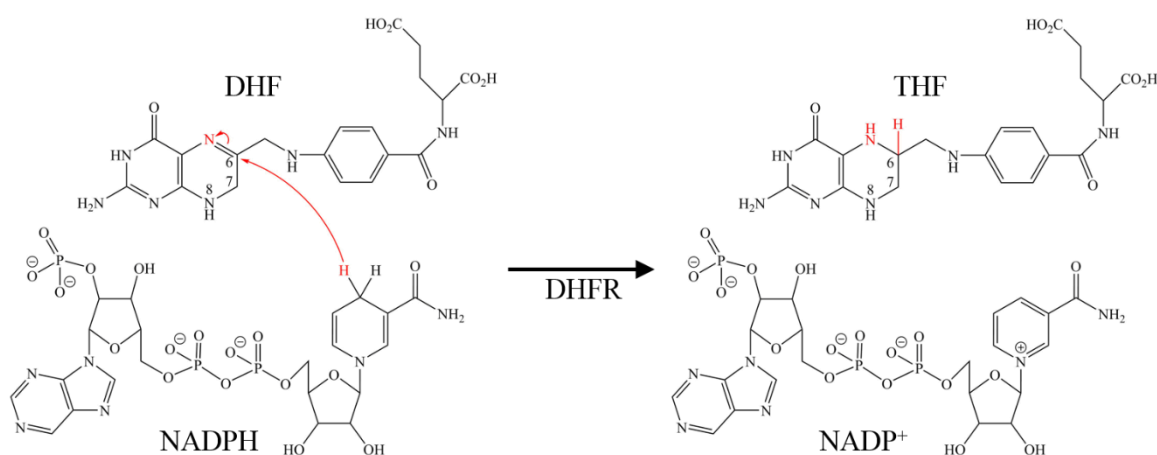


Figure 4.4: DHFR catalyzed reaction of DHF to THF with the cofactor NADPH.

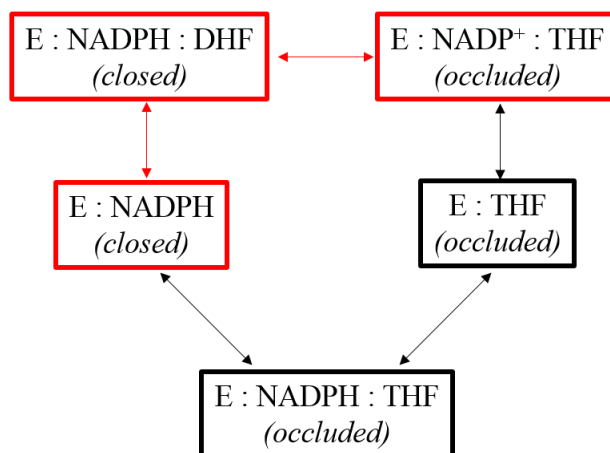


Figure 4.5: Catalytic cycle of DHFR where ‘E’ represents DHFR. The steps outlined in red are the focus of the microfluidic mixing studies described below. The starting complex is the binary complex, E:NADPH, then progressing with the substrate binding event and subsequent hydride transfer step. The orientation of the Met20 is also listed for each step.

Processes in the catalytic cycle can readily be studied with the spectroscopic activity of the cofactor. NADPH absorbs in the near UV at 340 nm and emits at 460 nm while NADP⁺ absorbs at 260 nm and has no fluorescence emission in the same region (figures 4.6). Because the two absorption peaks are separated enough not to interfere with each other, and the fact that NADP⁺ lacks an emission peak, NADPH creates a convenient fluorescent probe to follow kinetics of DHFR catalysis. As the hydride transfer occurs from the NADPH to DHF, the cofactor is oxidized and will thus eliminate any emission intensity. These kinetics have been studied previously,^{125,127} the first completed by Fierke *et al.* using the stopped-flow method.¹²⁵ Pre-steady state kinetics were used to establish rates for processes throughout the entire catalytic cycle. Since the following microfluidic mixing study deals with the kinetics of the hydride transfer step in the catalytic cycle, that step will be the focus from here on out. Fierke *et al.* used burst

phase kinetics to observe a pH dependent maximum rate of approximately 1000 s^{-1} , which was attributed to the hydride transfer rate at low pH. The pH dependence of the transfer was studied by Loveridge *et al.* and observed similar results at low pH.¹²⁷ There is also a temperature dependence on the same step at low pH, during which the product release is rate limiting, but then shifts to temperature independent as the hydride transfer rate becomes rate limiting itself at high pH.¹²⁷ The apparent pK_a of the pH dependent hydride transfer rate is 6.5 ± 0.1 .^{125,127}

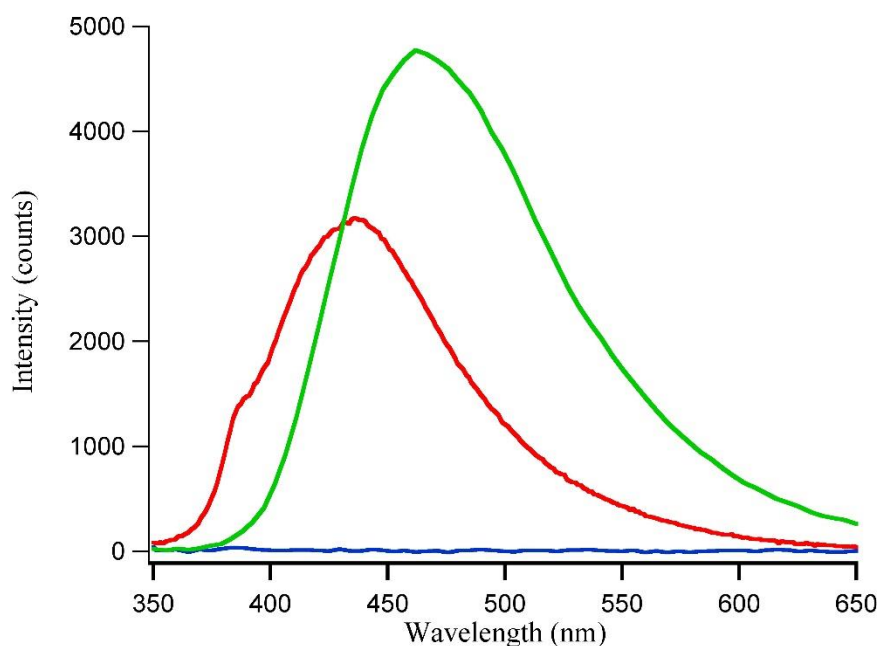


Figure 4.6: Equilibrium fluorescence spectra of DHFR cofactors and substrate. NADPH (green), NADP^+ (blue), and DHF (red) at pH 7.

There is reason, however, to question the kinetic results reported by these previous studies, both of which utilized the fluorescence emission of cofactor and substrate. The observed hydride transfer rates reported of nearly 1000 s^{-1} at low pH and single turnover concentrations implies this step was able to be measured with

fluorescence decays on the 1 ms timescale. The apparatus used for these studies were commercially available¹²⁷ or home-built¹²⁵ stopped-flow instruments with known dead times of at least 1 ms. This dead time represents the amount of time required to thoroughly mix the samples, analogous to the mixing time in microfluidic mixing. This begs the question of the reliability of reported rate that are the apparently the same or faster than the amount of time taken to simply mix the samples. Due to this fact, it is likely that the reported rates were obtained by an extrapolation of the data to a timescale before the actual mixing time of the stopped-flow instrument. Furthermore, these previous studies completely neglected conformational fluctuations and dynamics that are known to occur throughout the catalytic cycle. Substrate binding to the DHFR:NADPH binary complex, followed by hydride transfer from NADPH to DHF no longer sufficiently describes all processes that are happening in the enzyme-cofactor-substrate complex. Therefore, new studies and methodology are needed to tease out the other processes. The motivation behind the current mixing study was to resolve any additional dynamics on the micro- to millisecond timescale that may be closely coupled or perhaps uncoupled to the substrate binding and subsequent hydride transfer steps.

Section 4.3: DHFR microfluidic mixing experiments

Wild-type DHFR was expressed and purified similar to methods described previously.¹³⁰ After expression and purification, samples of DHFR were buffer exchanged using a HiPrep Desalting column (GE Healthcare) into separate MTEN buffers which had been pH adjusted to the designated pH values (4.5, 6.0, 7.0, and 9.0). A concentrated stock solution of NADPH (~6 mg/mL) was made by dissolving the

sodium salt in filtered deionized water. Concentrations of DHFR and NADPH were monitored through absorption peaks at 280 nm ($31100 \text{ M}^{-1}\text{cm}^{-1}$) and 340 nm ($6220 \text{ M}^{-1}\text{cm}^{-1}$), respectively. For mixing experiments, DHFR:NADPH complexes were made by diluting DHFR and NADPH stock solutions to final concentrations of 211 μM DHFR and 250 μM at each pH. The binary complexes were allowed to incubate at 20°C for at least 5 minutes before running the experiment. A 1 mM DHF solution was made by dissolving purified DHF in 5x diluted MTEN buffer pH 7.0 and spectroscopically confirmed at 282 nm with an extinction coefficient of $28000 \text{ M}^{-1} \text{ cm}^{-1}$.

For the following flow studies the same fluorescence microscope as described previously was utilized (Olympus IX81; Center Valley, PA). A 20x objective (Atlanta Microscope Service; Atlanta, GA) was used and microscope images were captured on a Hamamatsu (Bridgewater, NJ) C9100-14 ImageM-1k EM-CCD Camera. The microscope and camera were controlled by Slidebook 5.0 software (Imaging Innovations, Inc.; Denver, CO). The cofactor in the DHFR:NADPH complex was excited at $365 \pm 5 \text{ nm}$ using the filtered output of a HBO mercury short-arc lamp from Osram (Danvers, MA). Emission from the sample, which peaks at 460 nm was transmitted through a bandpass filter at $460 \pm 30 \text{ nm}$ and directed to the camera. For all images, the sample solution was flowed at a rate of $1.00 \mu\text{L min}^{-1}$ while each side flow rate was $20 \mu\text{L min}^{-1}$ at 20°C . The following fluorescence images were collected at least 6 times for each condition at each pH value, each with a 20 s integration time. Three separate types of images were necessary at each pH value in order to be able to analyze the hydride transfer step of DHFR catalysis effectively. The first was the DHFR:NADPH complex flowing in the sample channel with dilute MTEN buffer at pH 7.0 flowing in the sheath. This image was

to account for the natural decay in NADPH fluorescence not due to oxidation of the cofactor but rather the dilution of the sample as it mixes with the sheath solution. Next, the enzyme-cofactor complex is again flowed in the sample channel while DHF substrate is flowing in the sheath. This image accounts for the NADPH fluorescence decay attributed to the hydride transfer from NADPH to the DHF substrate resulting in oxidized NADP⁺. Lastly, an image with only MTEN buffer flowing as the sample and DHF in the sheath was required to account for the inherent DHF fluorescence in the same region as NADPH (figure 4.6). In all described experimental conditions, the DHF more readily diffuses into the sample stream as opposed to the DHFR:NADPH complex diffusing out into the sheath. This is simply due to the size differences of each sample. Because the DHF is in excess, DHF will inevitably diffuse into the sample stream and end up supplementing the fluorescence intensity. Therefore, this last image type helps remove the fluorescence contribution in the sample stream due to excess substrate.

In order to acquire the observed rates at each pH, the NADPH fluorescence transients were calculated using the following equation.

$$F_{hydride} = \frac{I_{hydride} - I_{DHF}}{I_{diffusion}} \quad (4.1)$$

In equation 5.1, $I_{hydride}$ represents the fluorescence intensity profile of the sample jet when the enzyme complex is flowing with DHF in the sheath. Examples of images used to obtain $I_{hydride}$ are figures 4.8a, 4.9a, and 4.10a for various pH values. I_{DHF} is the intensity of the sample jet when only MTEN buffer is flowing as the sample with DHF in the sheath. This is subtracted from $I_{hydride}$ in order to account for the supplemental intensity due to the fluorescent substrate diffusing into the sample jet. The resulting numerator follows the changes in fluorescence intensity of the conversion from NADPH to NADP⁺

by DHFR catalysis as well as the natural decay in intensity through dilution of the sample. Therefore, it is ratioed to $I_{diffusion}$ to eliminate the contribution of fluorescence decay by simple dilution. The resulting ratio, $F_{hydride}$, represents only the changes in NADPH fluorescence due to DHFR catalysis and can be analyzed directly for hydride transfer rates.

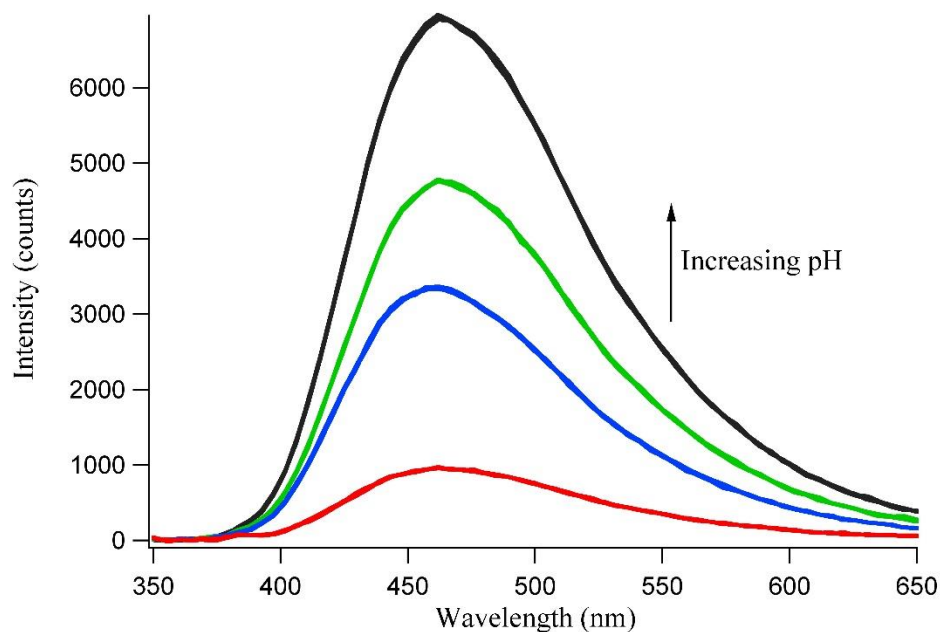


Figure 4.7: pH dependence of NADPH fluorescence in the DHFR:NADPH binary complex. The intrinsic fluorescence clearly increases with pH. Data shown is for complexes at pH 4.5 (red), 6.0 (blue), 7.0 (green), and 9.0 (black).

The intensity profiles for each type of image, as described above, are obtained by tracing the exact shape of the sample jet from images like those shown in figures 4.8, 4.9, and 4.10. The images are shown on a grayscale with white meaning high fluorescence intensity and black meaning no fluorescence. For each figure, the left-hand images are the DHFR:NADPH complex flowing in the sample channel and dilute MTEN buffer in the sheath. This image serves as the background image (and denominator of equation 4.1)

since no chemistry is occurring, only the natural decay in fluorescence signal due to dilution with the sheath solution. All images are taken with a 20 s integration time and as is evident even with the naked eye, the fluorescence intensity of NADPH bound to DHFR increases with pH. This is also clear in figure 4.7 which displays the equilibrium fluorescence intensity of the binary complex at different pH values. The right-hand images in figures 4.8, 4.9, and 4.10 all show the binary complex again flowing in the sample channel, but with DHF now flowing in the sheath. This is the condition in which hydride transfer occurs and the decrease of the 340 nm NADPH emission peak will be observed. Again, just by looking with the naked eye, it is evident that at low pH the fluorescence diminishes very quickly, while at higher pH NADPH fluorescence does not. This stark contrast clearly shows the differences in timescales of the chemistry step.

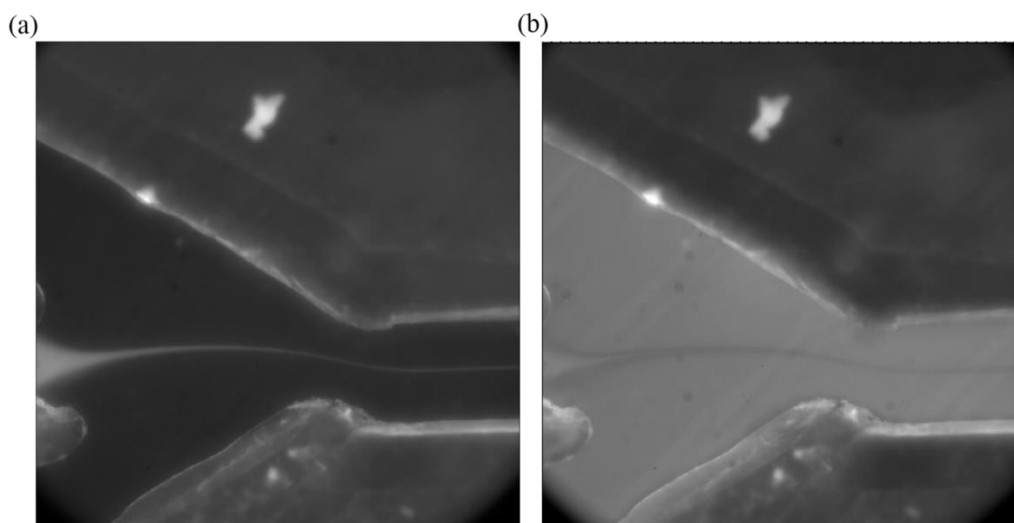


Figure 4.8: Background and sample images for DHFR flow studies at pH 4.5. (a) DHFR:NADPH complex flowing in the sample stream with MTEN buffer flowing in the sheath. This image serves as the background image because no turnover is occurring, however, the NADPH fluorescence decreases due to dilution. (b) DHFR:NADPH complex flowing in the sample stream with substrate DHF flowing in the sheath. This

image serves as the sample image because catalysis is occurring. The rapid decrease in NADPH fluorescence is quite evident even when comparing the images by eye.

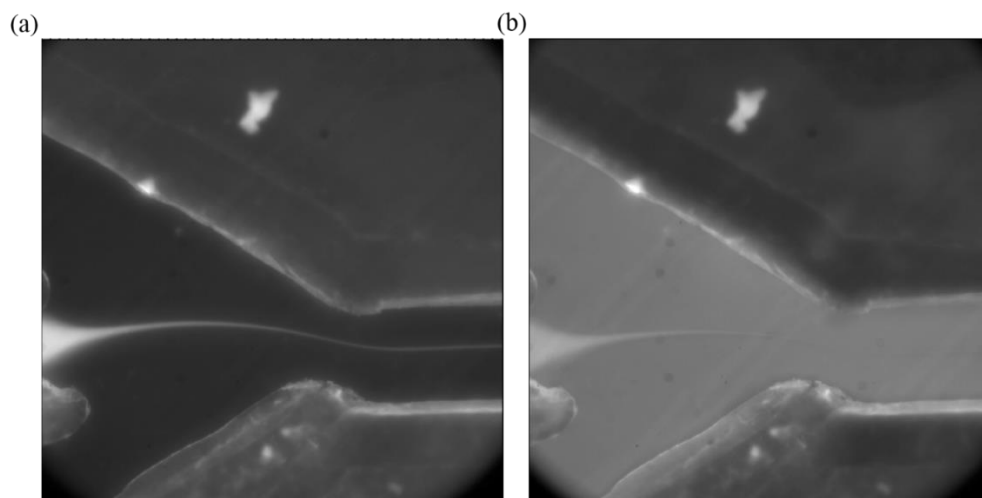


Figure 4.9: Background and sample images for DHFR flow studies at pH 7.0. (a) DHFR:NADPH complex flowing in the sample stream with MTEN buffer flowing in the sheath. This image serves as the background image because no turnover is occurring, however, the NADPH fluorescence decreases due to dilution. (b) DHFR:NADPH complex flowing in the sample stream with substrate DHF flowing in the sheath. This image serves as the sample image because catalysis is occurring. The decrease in the NADPH fluorescence is still evident when comparing the images by eye, however, it clearly does not decay as early as at pH 4.5.

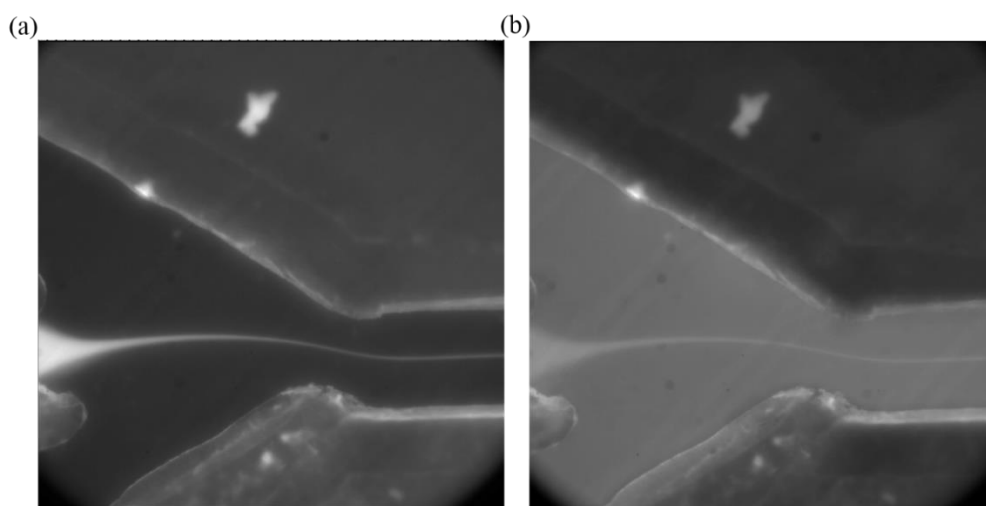


Figure 4.10: Background and sample images for DHFR flow studies at pH 9.0. (a) DHFR:NADPH complex flowing in the sample stream with MTEN buffer flowing in the sheath. This image serves as the background image because no turnover is occurring, however, the NADPH fluorescence decreases due to dilution. (b) DHFR:NADPH complex flowing in the sample stream with substrate DHF flowing in the sheath. This image serves as the sample image because catalysis is occurring. The decrease in the NADPH fluorescence is no longer evident when comparing the images by eye due to the much lower turnover rate at higher pH.

Once the sample jet analysis is complete on all images and ratioed as described above according to equation 4.1, the resulting fluorescence intensity is averaged among the multiple images taken with the same conditions, and normalized to the maximum intensity. The resulting transients are shown in figure 4.11. At low pH, like 4.5 (red) and 6.0 (blue) the fluorescence decay occurs on the fastest timescale, while slowest at high pH like 9.0 (black). The transient curves, however, do not fit well to a single exponential decay (fits not shown). However, the data do fit well to a biexponential function, suggesting there may in fact be other processes occurring on this timescale that are contributing to NADPH emission quenching other than hydride transfer. Therefore, the transients are fit with a double exponential function in order to resolve the other process. One of the decay rates in the biexponential fit was held constant at the literature values for the hydride transfer rates at each pH. They were previously reported at temperatures of 10 and 25°C.¹²⁷ The Arrhenius equation was then used to calculate what the hydride transfer rates should theoretically be at 20°C based on this data. The biexponential fits are laid overtop the data in figure 4.11.

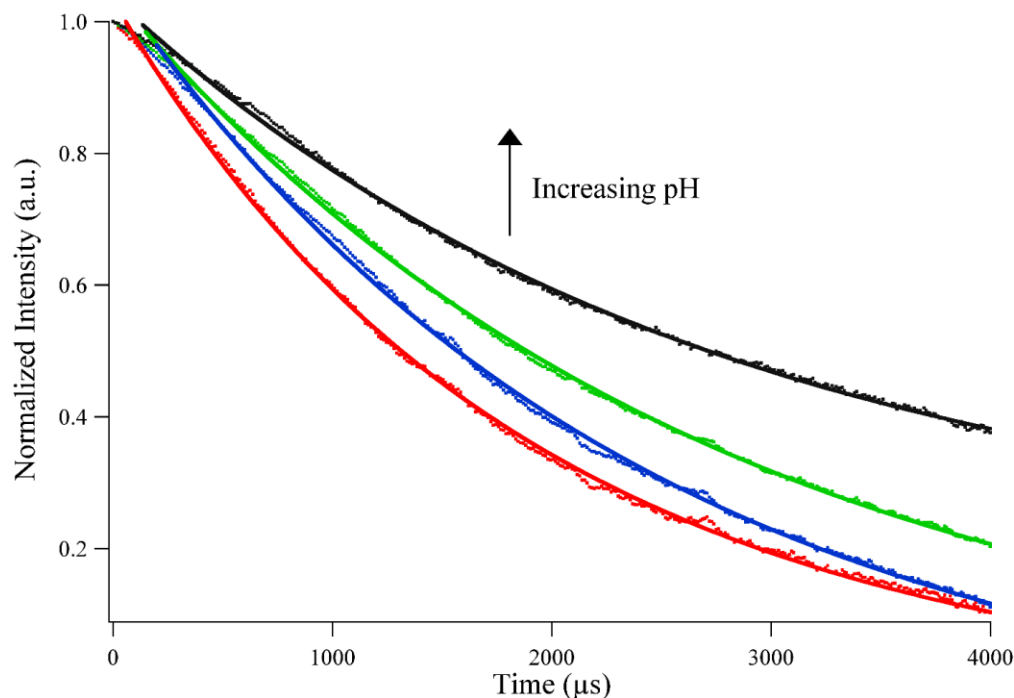


Figure 4.11: NADPH fluorescence decay transients and exponential fits for all pH values (red is pH 4.5, blue is pH 6.0, green is pH 7.0, and black is pH 9.0). The decay profiles are the result of the ratio of sample over background images. At low pH the decay is clearly much faster than at high pH. All transients are fit to a double exponential equation with one of the rates defined as the hydride transfer rate for the particular pH value.¹²⁷ The decay rates from the fit equation were in pixels and then transformed to the time regime using the calibration, described previously.

The data from the fit equations is displayed in table 4.1. The hydride transfer rate represented the literature values¹²⁷ for that step in the catalytic cycle at each pH, which were held constant during the fitting process. The hydride transfer rate is well known to be very pH dependent, occurring much faster at low pH values. The following discussion assumes that the literature values for the hydride transfer step are in fact reliable and the true rates. However, as discussed previously, there is cause for concern with these reported rates due to the experimental method used to obtain them. Therefore, it may be

that those rates should be ignored altogether and the fit equations just allowed to fit the data with no constraints. Nevertheless, for the time being, the literature values are still assumed to be correct.

The 'Fit Rate' in table 4.1 is the rate that was then free to make the best fit to the data. As is evident, the second rate stays relatively consistent for each pH value tested. Within the error of each reported value, they are essentially the same rate. This would suggest a second process is being resolved in the data that is pH independent in addition to the hydride transfer. The binary complex, DHFR:NADPH flowing through the sample channel first comes into contact with the DHF in the sheath solution and must bind prior to the hydride transfer step. Previous kinetic studies have resolved this substrate binding process^{125,130} and would be too fast to be resolved at the conditions currently described for mixing studies when the mixing time is taken into account. However, in the recent study by Reddish *et al.* laser-induced temperature-jump spectroscopy was utilized and was able to resolve another, slower rate, in addition to the much faster substrate binding event.¹³⁰ The slower phase was on the order of 300-400 s⁻¹, depending on the specific complex being studied. This slower rate would also be slow enough to be resolved in stopped-flow methods, previously used to establish the kinetic scheme of DHFR catalysis.¹²⁵ However, these studies were focused on establishing rates only for the processes known to occur based on an induced fit model, neglecting conformational dynamics now known to occur throughout the catalytic cycle.^{96,130,137,148-152} Therefore, even if this additional process was resolvable, previous studies were neglecting it.

Table 4.1: Kinetic data for pH biexponential fits of DHFR transients

pH	Hydride transfer (s ⁻¹) (held)	Contribution (%)	Fit rate (s ⁻¹)	Contribution (%)
4.5	730 ± 26	37	490 ± 120	63
6.0	550 ± 22	31	470 ± 100	69
7.0	170 ± 11	21	460 ± 90	79
9.0	2 ± 0.2	14	430 ± 90	86

The second rate in the exponential fits of the current data agree well with the previously resolved rates, and therefore are initially attributed to the same dynamic process. Since the substrate binding process is not resolvable with the current method, the process responsible for the second resolved rate must occur after substrate binding. It has been suggested this is possibly a conformational change coupled to the substrate binding process.¹³⁰ A conformational change associated with possible loop motions after substrate binding could act to quench NADPH emission before oxidation of the cofactor during hydride transfer completely eliminates fluorescence (figure 4.6). Whatever the conformational change exactly is, the current data suggest that it occurs on the same timescale at all pH values (figure 4.12). Even though the hydride transfer step is strongly pH dependent, the conformational changes that poise the complex ready for hydride transfer does not appear to be. Furthermore, it has been suggested the conformational change associated with the second observed rate corresponds to the fluctuations of the protein during its search for a favored conformation for hydride transfer.¹³⁰ These statements, however, cannot be proven definitively with the current results studying NADPH emission through substrate binding and subsequent hydride transfer.

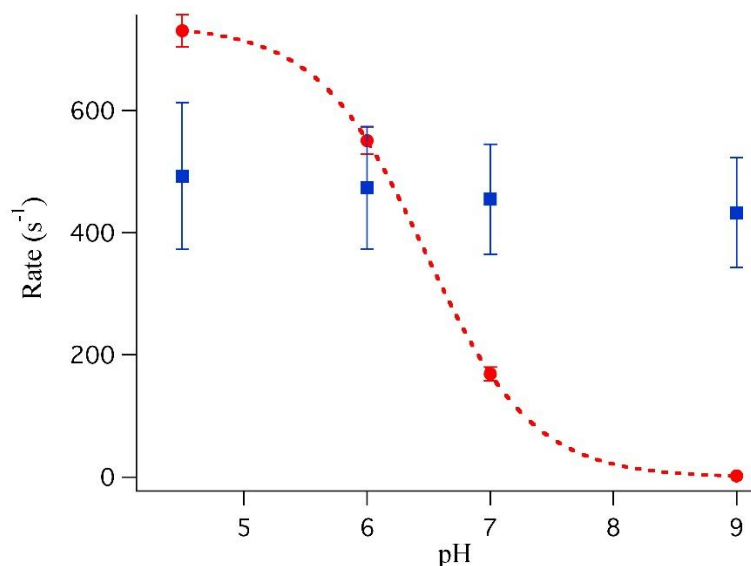


Figure 4.12: Resolved rates from the biexponential fit versus pH of complex. The rates associated with the hydride transfer step (red circles) are plotted and fit with a sigmoid curve (red dashed line) signifying the pK_a of the hydride step of 6.45. These data are clearly pH dependent while the second resolved rate (blue squares) stays essentially the same, independent of pH.

In fact, these results may prompt more questions than answers for the time being, with more experiments needed in the future to get the answers. Both stopped-flow studies and this microfluidic mixing study were resolving rates in burst phase kinetics. The fit rate resolved with the current study occurs in a few milliseconds and would therefore be accessible to previous techniques. Even though the previous stopped-flow studies were not specifically studying dynamic processes within the catalytic cycle, they still should have resolved this rate. So why was this rate missed with stopped-flow but now resolved with microfluidic techniques? In attempting to answer this question, two possible scenarios need to be considered. First, is that this resolved rate is unfortunately just some sort of instrument response that results in an apparent rate of approximately 400 s^{-1} .

Perhaps eliminating DHFR from the study and replicating the experimental conditions with only NADPH flowing in the sample channel when acquiring the $I_{hydride}$ and $I_{diffusion}$ images (equation 4.1) could test this scenario. Therefore, no hydride transfer should occur between the NADPH and DHF on the applicable timescale and if the same rate is still resolved, it must be due to the instrument. The second, and more biologically interesting scenario, would be that the resolved rate is in fact due to enzymatic dynamics either coupled or uncoupled to the hydride transfer step. Further studies to test this scenario could be to replace the substrate DHF with other substrates or inhibitors of DHFR, like folate that is reduced by DHFR albeit at much slower rates¹³⁵ or methotrexate, which binds to DHFR but completely inhibits catalysis.¹⁵³ Furthermore, there are known mutations in DHFR that can knock out the hydride transfer step altogether,¹⁵⁴ as well as site-specific labeled DHFR variants that could be used to study key regions of DHFR, like the Met20 loop,¹⁵⁵⁻¹⁵⁸ to determine the source of the rate. If the resolved rate of 400 s^{-1} is still present during experimental conditions like the ones just described, those methods may be able to more definitively attribute it to conformational changes in the enzyme. Whatever the case may be, it is clear that the current results are just a step in the process of deciphering dynamic processes occurring in DHFR and that further kinetic studies are quite necessary.

Nevertheless, as is evident from the previous study, studying enzymatic reactions on the timescale of hundreds of microseconds to a few milliseconds is viable in the sandwich-style fast microfluidic mixer. NADPH fluorescence emission was studied with fast mixing techniques, resulting in decay profiles fit to biexponential functions that were used to resolve the pH dependent hydride transfer rates in the DHFR catalytic cycle as

well as a previously observed rate on the order of 400-500 s⁻¹, which appears to be pH independent. The methods employed in the past to establish the currently accepted rates have seemingly missed important processes occurring in the catalytic cycle or may be wrong altogether. These processes can be studied and resolved with the reported microfluidic mixing methodology, furthering the capabilities in the field. It may even turn out that these microfluidic mixing techniques are much better developed to study kinetics on these timescales. The widely accepted rates for DHFR catalysis could quite possibly be incorrect due to the experimental methods employed to obtain them.

Chapter 5: Conclusions

This paper has discussed multiple aspects of the developments and improvements made to mixers and instruments utilized in the microfluidic mixing field. Extensive work has gone into the design and fabrication techniques of microfluidic mixers, specifically the sandwich-style mixer. New techniques to utilize fast microfluidic mixing with infrared spectroscopic probes have been developed and the successful application of the mixer and techniques to biomolecules like with the model enzyme, dihydrofolate reductase.

With regard to the design and fabrication techniques, the sandwich-style mixer was utilized in three unique designs and produced with a commercially available 3D printer. This study proved the utility of the fabrication technique with respect to multiple spectroscopic probes. The sandwich-style mixer created mixers with far wider applicability to different spectroscopic probes than previous techniques. Two optically transparent windows sandwich a spacer for the assembly of the mixer. In this case, the spacer was a 3D printed polymer with the microfluidic channels defined by lack of printed material and the only optically transparent requirement was the sandwiching windows. Serpentine, droplet, and cross-shaped mixers were printed and incorporated into the sandwich format mixer and used alongside three separate spectroscopic probes. Fluorescence, visible absorption, and IR absorption spectroscopies were the three types of spectroscopic probes used to exhibit the versatility of the sandwich-format mixer. In

addition to showing all three spectroscopic probes with different mixer designs, the same mixer was also implemented with the three probes as well, in order to prove its utility. Furthermore, the coupling of the sandwich-format mixer with 3D printed spacers helps to extend the versatility of the mixer, creating more of a custom microfluidic production platform. 3D printing provided an effective method to quickly and cheaply design and produce the spacers for the mixer, which completely determine the geometry of the microfluidic channels. The fabrication method can be applied to extending versatility within the microfluidic mixing community and ultimately make that community more appealing to new users. The 3D printing method did not prove to be viable in its original task of producing mixers with channel diameters on the order of 10s of microns, however, it did create a very applicable method to fabricate mixers very cheaply and quickly. This has implications for the microfluidic mixing community as a whole and especially for research groups that would otherwise be unable to break into the microfluidics field due to economic constraints. In addition to the 3D printing method of fabrication, there are currently two new types of mixers being tested in the lab that push the capabilities of our microfluidic mixers. The newest mixers include a laser cut spacer applicable to the sandwich-style mixer, but with much narrower channel diameters, as well as a quartz mixer that has microchannels etched in it with the same narrow diameters as the new spacer. With these developments, microfluidic mixing experiments will soon be able to study reactions on faster timescales than is currently accessible.

The sandwich-style mixer was also utilized in a mid-IR hyperspectral absorbance imaging system, capable of monitoring the progress of reactions with a sub-millisecond mixing time. The mixer and infrared imaging system were experimentally calibrated in

order to establish a time per pixel based on flow rates and position within the mixer. The applicability of the mixer for studying biomolecular reactions were then established through an AMP pD jump experiment. An acidic AMP sample was mixed with a neutral phosphate buffer to induce a pD jump through the pKa value of AMP, while following two IR absorbance peaks in the 1600 cm^{-1} region corresponding to the two protonation states. This pD jump experiment not only proved the utility of the imaging system but effectively reported the mixing time of the sandwich-style mixer with the laser cut spacer of $269 \pm 16\ \mu\text{s}$. The final study reported with the infrared imaging system was a $\text{H}_2\text{O}/\text{D}_2\text{O}$ mixing experiment was used to follow the absorption decay of the water at 1636 cm^{-1} and to model that decay with computational simulation. The simulation matched well with the experimentally obtained data. The reported mixing time was the fastest experimental mixing time to date of any microfluidic mixing system that uses IR spectroscopy for detection of the reaction progress. Using IR spectroscopy alleviates the requirement of intrinsic fluorescence or bulky fluorescence labels to biomolecules of interest. Infrared absorbance of a protein or its substrate or both can be followed through the time course of a reaction using this approach. The connection of IR spectra with specific structural features, such as the protein amide I vibration makes this approach widely applicable to biological reactions such as protein folding and enzymatic reactions. There are, however, still some obstacles that need to be overcome with the imaging system. Mainly, they lie with reducing signal-to-noise ratio primarily due to etalon interference patterns in acquired images.

Lastly, a microfluidic mixing experiment studying enzymatic reaction kinetics was performed on the model enzyme, dihydrofolate reductase. Previous kinetic studies

had been completed to follow steps throughout the catalytic cycle of DHFR, and were able to establish rates for many processes in the cycle using methods like stopped-flow and T-jump.^{125,127,130} One of the steps, the hydride transfer from NADPH to substrate DHF, is known to be pH dependent. Therefore, a mixing study was completed to follow the pH dependence of the hydride transfer. In doing so, a second process was observed in addition to the hydride transfer that has also been observed previously on the same timescale.¹³⁰ This process was observed at a rate of 400–500 s⁻¹ for each pH of DHFR studied with little deviation. According to the results and previous reports, the observed second process seems to be a pH independent conformational change DHFR goes through to ready itself for the hydride transfer step. This could be due to fluctuations in the mobile loops of DHFR, but in order to definitely assign the process, more kinetic studies are needed.

The progress outlined in this paper represents the beginning of the microfluidic mixing technique being utilized regularly in our lab to study enzymatic catalysis, and specifically, the dynamics that are coupled to catalysis. It is with great hope that the discussed developments can be used fruitfully and regularly in order to answer questions regarding how enzymes really work.

References

- (1) Hertzog, D. E.; Michalet, X.; Jager, M.; Kong, X.; Santiago, J. G.; Weiss, S.; Bakajin, O. Femtomole Mixer for Microsecond Kinetic Studies of Protein Folding. *Anal. Chem.* **2004**, *76*, 7169-7178.
- (2) Kauffmann, E.; Darnton, N. C.; Austin, R. H.; Batt, C.; Gerwert, K. Lifetimes of intermediates in the β -sheet to α -helix transition of β -lactoglobulin by using a diffusional IR mixer. *Proc. Natl. Acad. Sci. U.S.A.* **2001**, *98*, 6646-6649.
- (3) Li, Y.; Liu, C.; Feng, X.; Xu, Y.; Liu, B.-F. Ultrafast Microfluidic Mixer for Tracking the Early Folding Kinetics of Human Telomere G-Quadruplex. *Anal. Chem.* **2014**.
- (4) Abate, A. R.; Hung, T.; Sperling, R. A.; Mary, P.; Rotem, A.; Agresti, J. J.; Weiner, M. A.; Weitz, D. A. DNA sequence analysis with droplet-based microfluidics. *Lab Chip* **2013**, *13*, 4864-4869.
- (5) Tan, S. J.; Phan, H.; Gerry, B. M.; Kuhn, A.; Hong, L. Z.; Min Ong, Y.; Poon, P. S. Y.; Unger, M. A.; Jones, R. C.; Quake, S. R.; Burkholder, W. F. A Microfluidic Device for Preparing Next Generation DNA Sequencing Libraries and for Automating Other Laboratory Protocols That Require One or More Column Chromatography Steps. *PLoS ONE* **2013**, *8*, e64084.
- (6) Lagally, E. T.; Simpson, P. C.; Mathies, R. A. Monolithic integrated microfluidic DNA amplification and capillary electrophoresis analysis system. *Sensors and Actuators B: Chemical* **2000**, *63*, 138-146.

- (7) Hoscic, S.; Murthy, S. K.; Koppes, A. N. Microfluidic Sample Preparation for Single Cell Analysis. *Anal. Chem.* **2016**, *88*, 354-380.
- (8) Yin, H.; Marshall, D. Microfluidics for single cell analysis. *Curr. Opin. Biotechnol.* **2012**, *23*, 110-119.
- (9) Lecault, V.; White, A. K.; Singhal, A.; Hansen, C. L. Microfluidic single cell analysis: from promise to practice. *Curr. Opin. Chem. Biol.* **2012**, *16*, 381-390.
- (10) Duncanson, W. J.; Lin, T.; Abate, A. R.; Seiffert, S.; Shah, R. K.; Weitz, D. A. Microfluidic synthesis of advanced microparticles for encapsulation and controlled release. *Lab Chip* **2012**, *12*, 2135-2145.
- (11) Li, W.; Greener, J.; Voicu, D.; Kumacheva, E. Multiple modular microfluidic (M3) reactors for the synthesis of polymer particles. *Lab Chip* **2009**, *9*, 2715-2721.
- (12) Nightingale, A. M.; de Mello, J. C. Microscale synthesis of quantum dots. *J. Mater. Chem.* **2010**, *20*, 8454-8463.
- (13) Buchegger, W.; Haller, A.; van den Driesche, S.; Kraft, M.; Lendl, B.; Vellekoop, M. Studying enzymatic bioreactions in a millisecond microfluidic flow mixer. *Biomicrofluidics* **2012**, *6*, 012803-012809.
- (14) Chan, K. L. A.; Kazarian, S. G. Label-Free Chemical Detection in Microfabricated Devices Using FT-IR Spectroscopic Imaging. *Spectroscopy* **2012**, *27*, 22-+.
- (15) Humana, T.: *Protein-ligand interactions- methods and applications*, 2005.

- (16) Kern, S.; Riester, D.; Hildmann, C.; Schwienhorst, A.; Meyer-Almes, F.-J. Inhibitor-mediated stabilization of the conformational structure of a histone deacetylase-like amidohydrolase. *FEBS Journal* **2007**, *274*, 3578-3588.
- (17) Li, Y.; Zhang, D.; Feng, X.; Xu, Y.; Liu, B.-F. A microsecond microfluidic mixer for characterizing fast biochemical reactions. *Talanta* **2012**, *88*, 175-180.
- (18) McMullen, J. P.; Jensen, K. F.: Integrated Microreactors for Reaction Automation: New Approaches to Reaction Development. In *Annual Review of Analytical Chemistry, Vol 3*; Yeung, E. S., Zare, R. N., Eds.; Annual Review of Analytical Chemistry, 2010; Vol. 3; pp 19-42.
- (19) Schleegeer, M.; Wagner, C.; Vellekoop, M.; Lendl, B.; Heberle, J. Time-resolved flow-flash FT-IR difference spectroscopy: the kinetics of CO photodissociation from myoglobin revisited. *Anal. Bioanal. Chem.* **2009**, *394*, 1869-1877.
- (20) Nguyen, N.-T.; Wu, Z. Micromixers—a review. *Journal of Micromechanics and Microengineering* **2005**, *15*, R1.
- (21) Wolfenden, R.; Snider, M. J. The Depth of Chemical Time and the Power of Enzymes as Catalysts. *Acc. Chem. Res.* **2001**, *34*, 938-945.
- (22) Siegel, J. B.; Zanghellini, A.; Lovick, H. M.; Kiss, G.; Lambert, A. R.; St.Clair, J. L.; Gallaher, J. L.; Hilvert, D.; Gelb, M. H.; Stoddard, B. L.; Houk, K. N.; Michael, F. E.; Baker, D. Computational Design of an Enzyme Catalyst for a Stereoselective Bimolecular Diels-Alder Reaction. *Science* **2010**, *329*, 309-313.

- (23) Eiben, C. B.; Siegel, J. B.; Bale, J. B.; Cooper, S.; Khatib, F.; Shen, B. W.; Players, F.; Stoddard, B. L.; Popovic, Z.; Baker, D. Increased Diels-Alderase activity through backbone remodeling guided by Foldit players. *Nat Biotech* **2012**, *30*, 190-192.
- (24) Preiswerk, N.; Beck, T.; Schulz, J. D.; Milovnik, P.; Mayer, C.; Siegel, J. B.; Baker, D.; Hilvert, D. Impact of scaffold rigidity on the design and evolution of an artificial Diels-Alderase. *Proc. Natl. Acad. Sci. U.S.A.* **2014**, *111*, 8013-8018.
- (25) Bar-Even, A.; Noor, E.; Savir, Y.; Liebermeister, W.; Davidi, D.; Tawfik, D. S.; Milo, R. The Moderately Efficient Enzyme: Evolutionary and Physicochemical Trends Shaping Enzyme Parameters. *Biochemistry* **2011**, *50*, 4402-4410.
- (26) Austin, R. H.; Beeson, K. W.; Eisenstein, L.; Frauenfelder, H.; Gunsalus, I. C. Dynamics of ligand binding to myoglobin. *Biochemistry* **1975**, *14*, 5355-5373.
- (27) Boehr, D. D.; Dyson, H. J.; Wright, P. E. An NMR Perspective on Enzyme Dynamics. *Chem. Rev.* **2006**, *106*, 3055-3079.
- (28) Henzler-Wildman, K. A.; Lei, M.; Thai, V.; Kerns, S. J.; Karplus, M.; Kern, D. A hierarchy of timescales in protein dynamics is linked to enzyme catalysis. *Nature* **2007**, *450*, 913-916.
- (29) Wolf-Watz, M.; Thai, V.; Henzler-Wildman, K.; Hadjipavlou, G.; Eisenmesser, E. Z.; Kern, D. Linkage between dynamics and catalysis in a thermophilic-mesophilic enzyme pair. *Nat Struct Mol Biol* **2004**, *11*, 945-949.
- (30) Muhandiram, D. R.; Yamazaki, T.; Sykes, B. D.; Kay, L. E. Measurement of ^2H T1 and T1.ρ. Relaxation Times in Uniformly ^{13}C -Labeled and Fractionally ^2H -Labeled Proteins in Solution. *JACS* **1995**, *117*, 11536-11544.

- (31) Nicholson, L. K.; Kay, L. E.; Baldisseri, D. M.; Arango, J.; Young, P. E.; Bax, A.; Torchia, D. A. Dynamics of methyl groups in proteins as studied by proton-detected carbon-13 NMR spectroscopy. Application to the leucine residues of staphylococcal nuclease. *Biochemistry* **1992**, *31*, 5253-5263.
- (32) Rozovsky, S.; Jogl, G.; Tong, L.; McDermott, A. E. Solution-state NMR investigations of triosephosphate isomerase active site loop motion: ligand release in relation to active site loop dynamics1. *J. Mol. Biol.* **2001**, *310*, 271-280.
- (33) Seifert, M. H. J.; Breitenlechner, C. B.; Bossemeyer, D.; Huber, R.; Holak, T. A.; Engh, R. A. Phosphorylation and Flexibility of Cyclic-AMP-Dependent Protein Kinase (PKA) Using ³¹P NMR Spectroscopy†. *Biochemistry* **2002**, *41*, 5968-5977.
- (34) Burke, K. S.; Parul, D.; Reddish, M. J.; Dyer, R. B. A simple three-dimensional-focusing, continuous-flow mixer for the study of fast protein dynamics. *Lab Chip* **2013**, *13*, 2912-2921.
- (35) Gambin, Y.; Simonnet, C.; VanDelinder, V.; Deniz, A.; Groisman, A. Ultrafast microfluidic mixer with three-dimensional flow focusing for studies of biochemical kinetics. *Lab Chip* **2010**, *10*, 598-609.
- (36) Hertzog, D. E.; Ivorra, B.; Mohammadi, B.; Bakajin, O.; Santiago, J. G. Optimization of a Microfluidic Mixer for Studying Protein Folding Kinetics. *Anal. Chem.* **2006**, *78*, 4299-4306.
- (37) Knight, J. B.; Vishwanath, A.; Brody, J. P.; Austin, R. H. Hydrodynamic Focusing on a Silicon Chip: Mixing Nanoliters in Microseconds. *Phys. Rev. Lett.* **1998**, *80*, 3863-3866.

(38) Pabit, S. A.; Hagen, S. J. Laminar-Flow Fluid Mixer for Fast Fluorescence Kinetics Studies. *Biophys. J.* **2002**, *83*, 2872-2878.

(39) Park, H. Y.; Kim, S. A.; Korlach, J.; Rhoades, E.; Kwok, L. W.; Zipfel, W. R.; Waxham, M. N.; Webb, W. W.; Pollack, L. Conformational changes of calmodulin upon Ca²⁺ binding studied with a microfluidic mixer. *Proc. Natl. Acad. Sci. U.S.A.* **2008**, *105*, 542-547.

(40) Shastry, M. C. R.; Luck, S. D.; Roder, H. A Continuous-Flow Capillary Mixing Method to Monitor Reactions on the Microsecond Time Scale. *Biophys. J.* **1998**, *74*, 2714-2721.

(41) Teilum, K.; Maki, K.; Kragelund, B. B.; Poulsen, F. M.; Roder, H. Early kinetic intermediate in the folding of acyl-CoA binding protein detected by fluorescence labeling and ultrarapid mixing. *Proc. Natl. Acad. Sci. U.S.A.* **2002**, *99*, 9807-9812.

(42) Zhu, L.; Ghosh, K.; King, M.; Cellmer, T.; Bakajin, O.; Lapidus, L. J. Evidence of Multiple Folding Pathways for the Villin Headpiece Subdomain. *J. Phys. Chem. B* **2011**, *115*, 12632-12637.

(43) Barnes, S. E.; Cygan, Z. T.; Yates, J. K.; Beers, K. L.; Amis, E. J. Raman spectroscopic monitoring of droplet polymerization in a microfluidic device. *Analyst* **2006**, *131*, 1027-1033.

(44) Masten, D. A.; Foy, B. R.; Harradine, D. M.; Dyer, R. B. In situ Raman spectroscopy of reactions in supercritical water. *The Journal of Physical Chemistry* **1993**, *97*, 8557-8559.

(45) Ro, K. W.; Lim, K.; Shim, B. C.; Hahn, J. H. Integrated Light Collimating System for Extended Optical-Path-Length Absorbance Detection in Microchip-Based Capillary Electrophoresis. *Anal. Chem.* **2005**, *77*, 5160-5166.

(46) Floyd, T. M.; Schmidt, M. A.; Jensen, K. F. Silicon Micromixers with Infrared Detection for Studies of Liquid-Phase Reactions. *Ind. Eng. Chem. Res.* **2004**, *44*, 2351-2358.

(47) Kakuta, M.; Hinsmann, P.; Manz, A.; Lendl, B. Time-resolved Fourier transform infrared spectrometry using a microfabricated continuous flow mixer: application to protein conformation study using the example of ubiquitin. *Lab Chip* **2003**, *3*, 82-85.

(48) Herzig-Marx, R.; Queeney, K. T.; Jackman, R. J.; Schmidt, M. A.; Jensen, K. F. Infrared spectroscopy for chemically specific sensing in silicon-based microreactors. *Anal. Chem.* **2004**, *76*, 6476-6483.

(49) Pan, T.; Kelly, R. T.; Asplund, M. C.; Woolley, A. T. Fabrication of calcium fluoride capillary electrophoresis microdevices for on-chip infrared detection. *J. Chromatogr. A* **2004**, *1027*, 231-235.

(50) Wagner, C.; Buchegger, W.; Vellekoop, M.; Kraft, M.; Lendl, B. Time-resolved mid-IR spectroscopy of (bio)chemical reactions in solution utilizing a new generation of continuous-flow micro-mixers. *Anal. Bioanal. Chem.* **2011**, *400*, 2487-2497.

(51) Chan, K. L. A.; Kazarian, S. G. FT-IR Spectroscopic Imaging of Reactions in Multiphase Flow in Microfluidic Channels. *Anal. Chem.* **2012**, *84*, 4052-4056.

- (52) Bart, J.; Kolkman, A. J.; Oosthoek-de Vries, A. J.; Koch, K.; Nieuwland, P. J.; Janssen, H.; van Bentum, J.; Ampt, K. A. M.; Rutjes, F. P. J. T.; Wijmenga, S. S.; Gardeniers, H.; Kentgens, A. P. M. A Microfluidic High-Resolution NMR Flow Probe. *JACS* **2009**, *131*, 5014-5015.
- (53) Kane, A. S.; Hoffmann, A.; Baumgärtel, P.; Seckler, R.; Reichardt, G.; Horsley, D. A.; Schuler, B.; Bakajin, O. Microfluidic Mixers for the Investigation of Rapid Protein Folding Kinetics Using Synchrotron Radiation Circular Dichroism Spectroscopy. *Anal. Chem.* **2008**, *80*, 9534-9541.
- (54) Grigoriev, R.; Schuster, H. G.: *Transport and Mixing in Laminar Flows: From Microfluidics to Oceanic Currents*; Wiley, 2012.
- (55) Kamholz, A. E.; Weigl, B. H.; Finlayson, B. A.; Yager, P. Quantitative Analysis of Molecular Interaction in a Microfluidic Channel: The T-Sensor. *Anal. Chem.* **1999**, *71*, 5340-5347.
- (56) Ismagilov, R. F.; Stroock, A. D.; Kenis, P. J. A.; Whitesides, G.; Stone, H. A. Experimental and theoretical scaling laws for transverse diffusive broadening in two-phase laminar flows in microchannels. *Appl. Phys. Lett.* **2000**, *76*, 2376-2378.
- (57) Hinsmann, P.; Frank, J.; Svasek, P.; Harasek, M.; Lendl, B. Design, simulation and application of a new micromixing device for time resolved infrared spectroscopy of chemical reactions in solution. *Lab Chip* **2001**, *1*, 16-21.
- (58) Walker, G. M.; Ozers, M. S.; Beebe, D. J. Cell infection within a microfluidic device using virus gradients. *Sensors and Actuators B: Chemical* **2004**, *98*, 347-355.

- (59) Park, H. Y.; Qiu, X.; Rhoades, E.; Korlach, J.; Kwok, L. W.; Zipfel, W. R.; Webb, W. W.; Pollack, L. Achieving Uniform Mixing in a Microfluidic Device: Hydrodynamic Focusing Prior to Mixing. *Anal. Chem.* **2006**, *78*, 4465-4473.
- (60) Hengzi, W.; Pio, I.; Erol, H.; Syed, M. Optimizing layout of obstacles for enhanced mixing in microchannels. *Smart Mater. Struct.* **2002**, *11*, 662.
- (61) Wong, S. H.; Bryant, P.; Ward, M.; Wharton, C. Investigation of mixing in a cross-shaped micromixer with static mixing elements for reaction kinetics studies. *Sensors and Actuators B: Chemical* **2003**, *95*, 414-424.
- (62) Lin, Y.; Gerfen, G. J.; Rousseau, D. L.; Yeh, S.-R. Ultrafast Microfluidic Mixer and Freeze-Quenching Device. *Anal. Chem.* **2003**, *75*, 5381-5386.
- (63) Mengeaud, V.; Josserand, J.; Girault, H. H. Mixing Processes in a Zigzag Microchannel: Finite Element Simulations and Optical Study. *Anal. Chem.* **2002**, *74*, 4279-4286.
- (64) Liu, R. H.; Stremler, M. A.; Sharp, K. V.; Olsen, M. G.; Santiago, J. G.; Adrian, R. J.; Aref, H.; Beebe, D. J. Passive mixing in a three-dimensional serpentine microchannel. *Microelectromechanical Systems, Journal of* **2000**, *9*, 190-197.
- (65) Vijayendran, R. A.; Motsegood, K. M.; Beebe, D. J.; Leckband, D. E. Evaluation of a Three-Dimensional Micromixer in a Surface-Based Biosensor†. *Langmuir* **2003**, *19*, 1824-1828.
- (66) Sung-Jin, P.; Jung Kyung, K.; Junha, P.; Seok, C.; Chanil, C.; Jun Keun, C. Rapid three-dimensional passive rotation micromixer using the breakup process. *Journal of Micromechanics and Microengineering* **2004**, *14*, 6.

- (67) Jen, C.-P.; Wu, C.-Y.; Lin, Y.-C.; Wu, C.-Y. Design and simulation of the micromixer with chaotic advection in twisted microchannels. *Lab Chip* **2003**, *3*, 77-81.
- (68) Johnson, T. J.; Ross, D.; Locascio, L. E. Rapid Microfluidic Mixing. *Anal. Chem.* **2002**, *74*, 45-51.
- (69) Stroock, A. D.; Dertinger, S. K. W.; Ajdari, A.; Mezić, I.; Stone, H. A.; Whitesides, G. M. Chaotic Mixer for Microchannels. *Science* **2002**, *295*, 647-651.
- (70) Okkels, F.; Tabeling, P. Spatiotemporal Resonances in Mixing of Open Viscous Fluids. *Phys. Rev. Lett.* **2004**, *92*, 038301.
- (71) Oddy, M. H.; Santiago, J. G.; Mikkelsen, J. C. Electrokinetic Instability Micromixing. *Anal. Chem.* **2001**, *73*, 5822-5832.
- (72) Zhongliang, T.; Seungbae, H.; Djordje, D.; Vijay, M.; Alan, C. W.; James, Y.; Richard, M. O. Electrokinetic flow control for composition modulation in a microchannel. *Journal of Micromechanics and Microengineering* **2002**, *12*, 870.
- (73) Liu, R. H.; Yang, J.; Pindera, M. Z.; Athavale, M.; Grodzinski, P. Bubble-induced acoustic micromixing. *Lab Chip* **2002**, *2*, 151-157.
- (74) Yaralioglu, G. G.; Wygant, I. O.; Marentis, T. C.; Khuri-Yakub, B. T. Ultrasonic Mixing in Microfluidic Channels Using Integrated Transducers. *Anal. Chem.* **2004**, *76*, 3694-3698.
- (75) Norbert, S.; Thomas, F.; Helmut, W. A modular microfluid system with an integrated micromixer. *Journal of Micromechanics and Microengineering* **1996**, *6*, 99.
- (76) Koch, M.; Chatelain, D.; Evans, A. G. R.; Brunnschweiler, A. Two simple micromixers based on silicon. *Journal of Micromechanics and Microengineering* **1998**, *8*, 123.

- (77) Wong, S. H.; Ward, M. C. L.; Wharton, C. W. Micro T-mixer as a rapid mixing micromixer. *Sensors and Actuators B: Chemical* **2004**, *100*, 359-379.
- (78) Veenstra, T. T.; Lammerink, T. S. J.; Elwenspoek, M. C.; Berg, A. v. d. Characterization method for a new diffusion mixer applicable in micro flow injection analysis systems. *Journal of Micromechanics and Microengineering* **1999**, *9*, 199.
- (79) G. Bessoth, F.; J. deMello, A.; Manz, A. Microstructure for efficient continuous flow mixing. *Anal. Commun.* **1999**, *36*, 213-215.
- (80) Xia, Y.; Kim, E.; Zhao, X.-M.; Rogers, J. A.; Prentiss, M.; Whitesides, G. M. Complex Optical Surfaces Formed by Replica Molding Against Elastomeric Masters. *Science* **1996**, *273*, 347-349.
- (81) Duffy, D. C.; McDonald, J. C.; Schueller, O. J. A.; Whitesides, G. M. Rapid Prototyping of Microfluidic Systems in Poly(dimethylsiloxane). *Anal. Chem.* **1998**, *70*, 4974-4984.
- (82) McDonald, J. C.; Whitesides, G. M. Poly(dimethylsiloxane) as a Material for Fabricating Microfluidic Devices. *Acc. Chem. Res.* **2002**, *35*, 491-499.
- (83) Delamarche, E.; Bernard, A.; Schmid, H.; Bietsch, A.; Michel, B.; Biebuyck, H. Microfluidic Networks for Chemical Patterning of Substrates: Design and Application to Bioassays. *JACS* **1998**, *120*, 500-508.
- (84) Wunderlich, B.; Nettels, D.; Benke, S.; Clark, J.; Weidner, S.; Hofmann, H.; Pfeil, S. H.; Schuler, B. Microfluidic mixer designed for performing single-molecule kinetics with confocal detection on timescales from milliseconds to minutes. *Nat. Protocols* **2013**, *8*, 1459-1474.

- (85) Kise, D. P.; Magana, D.; Reddish, M. J.; Dyer, R. B. Submillisecond mixing in a continuous-flow, microfluidic mixer utilizing mid-infrared hyperspectral imaging detection. *Lab Chip* **2014**, *14*, 584-591.
- (86) Comina, G.; Suska, A.; Filippini, D. Low cost lab-on-a-chip prototyping with a consumer grade 3D printer. *Lab Chip* **2014**, *14*, 2978-2982.
- (87) Erkal, J. L.; Selimovic, A.; Gross, B. C.; Lockwood, S. Y.; Walton, E. L.; McNamara, S.; Martin, R. S.; Spence, D. M. 3D printed microfluidic devices with integrated versatile and reusable electrodes. *Lab Chip* **2014**, *14*, 2023-2032.
- (88) Kitson, P. J.; Rosnes, M. H.; Sans, V.; Dragone, V.; Cronin, L. Configurable 3D-Printed millifluidic and microfluidic 'lab on a chip' reactionware devices. *Lab Chip* **2012**, *12*, 3267-3271.
- (89) Martino, C.; Berger, S.; Wootton, R. C. R.; deMello, A. J. A 3D-printed microcapillary assembly for facile double emulsion generation. *Lab Chip* **2014**.
- (90) O'Neill, P. F.; Ben Azouz, A.; Vázquez, M.; Liu, J.; Marczak, S.; Slouka, Z.; Chang, H. C.; Diamond, D.; Brabazon, D. Advances in three-dimensional rapid prototyping of microfluidic devices for biological applications. *Biomicrofluidics* **2014**, *8*, -.
- (91) Rogers, C. I.; Qaderi, K.; Woolley, A. T.; Nordin, G. P. 3D printed microfluidic devices with integrated valves. *Biomicrofluidics* **2015**, *9*, 016501.
- (92) Shallan, A. I.; Smejkal, P.; Corban, M.; Guijt, R. M.; Breadmore, M. C. Cost-Effective Three-Dimensional Printing of Visibly Transparent Microchips within Minutes. *Anal. Chem.* **2014**, *86*, 3124-3130.

- (93) Tseng, P.; Murray, C.; Kim, D.; Di Carlo, D. Research highlights: printing the future of microfabrication. *Lab Chip* **2014**, *14*, 1491-1495.
- (94) Kise, D. P.; Reddish, M. J.; Dyer, R. B. Sandwich-format 3D printed microfluidic mixers: a flexible platform for multi-probe analysis. *Journal of Micromechanics and Microengineering* **2015**, *25*, 124002.
- (95) Tsuboi, M.; Kyogoku, Y.; Shimanouchi, T. Infrared absorption spectra of protonated and deprotonated nucleosides. *Biochim. Biophys. Acta* **1962**, *55*, 1-12.
- (96) Tehei, M.; Smith, J. C.; Monk, C.; Ollivier, J.; Oetl, M.; Kurkal, V.; Finney, J. L.; Daniel, R. M. Dynamics of Immobilized and Native Escherichia coli Dihydrofolate Reductase by Quasielastic Neutron Scattering. *Biophys. J.* **2006**, *90*, 1090-1097.
- (97) Rodriguez Schmidt, R.; Hernandez Cifre, J. G.; Garcia de la Torre, J. Translational diffusion coefficients of macromolecules. *The European physical journal. E, Soft matter* **2012**, *35*, 9806.
- (98) Chick, H.; Lubrzynska, E. The Viscosity of Some Protein Solutions. *Biochem. J* **1914**, *8*, 59-69.
- (99) Baroud, C. N.; Gallaire, F.; Dangla, R. Dynamics of microfluidic droplets. *Lab Chip* **2010**, *10*, 2032-2045.
- (100) Bringer, M. R.; Gerdts, C. J.; Song, H.; Tice, J. D.; Ismagilov, R. F. Microfluidic systems for chemical kinetics that rely on chaotic mixing in droplets. *Philos. Trans. R. Soc. London, A* **2004**, *362*, 1087-1104.

(101) Tice, J. D.; Song, H.; Lyon, A. D.; Ismagilov, R. F. Formation of Droplets and Mixing in Multiphase Microfluidics at Low Values of the Reynolds and the Capillary Numbers. *Langmuir* **2003**, *19*, 9127-9133.

(102) Fuerstman, M. J.; Garstecki, P.; Whitesides, G. M. Coding/Decoding and Reversibility of Droplet Trains in Microfluidic Networks. *Science* **2007**, *315*, 828-832.

(103) Prakash, M.; Gershenfeld, N. Microfluidic Bubble Logic. *Science* **2007**, *315*, 832-835.

(104) Kobayashi, I.; Uemura, K.; Nakajima, M. Formulation of monodisperse emulsions using submicron-channel arrays. *Colloids and Surfaces A: Physicochemical and Engineering Aspects* **2007**, *296*, 285-289.

(105) Schuler, B.; Hofmann, H. Single-molecule spectroscopy of protein folding dynamics—expanding scope and timescales. *Current Opinion in Structural Biology* **2013**, *23*, 36-47.

(106) Leung, S.-A.; Winkle, R. F.; Wootton, R. C. R.; deMello, A. J. A method for rapid reaction optimisation in continuous-flow microfluidic reactors using online Raman spectroscopic detection. *Analyst* **2005**, *130*, 46-51.

(107) Nagarajan, S.; Taskent-Sezgin, H.; Parul, D.; Carrico, I.; Raleigh, D. P.; Dyer, R. B. Differential Ordering of the Protein Backbone and Side Chains during Protein Folding Revealed by Site-Specific Recombinant Infrared Probes. *JACS* **2011**, *133*, 20335-20340.

(108) Salmon, J.-B.; Ajdari, A.; Tabeling, P.; Servant, L.; Talaga, D.; Joanicot, M. In situ Raman imaging of interdiffusion in a microchannel. *Appl. Phys. Lett.* **2005**, *86*, 094106-094103.

- (109) Schwarz, M. A.; Hauser, P. C. Recent developments in detection methods for microfabricated analytical devices. *Lab Chip* **2001**, *1*, 1-6.
- (110) Dyer, R. B.; Gai, F.; Woodruff, W. H.; Gilmanshin, R.; Callender, R. H. Infrared Studies of Fast Events in Protein Folding. *Acc. Chem. Res.* **1998**, *31*, 709-716.
- (111) Gallignani, M.; Brunetto, M. d. R. Infrared detection in flow analysis — developments and trends (review). *Talanta* **2004**, *64*, 1127-1146.
- (112) Chan, K. L. A.; Gulati, S.; Edel, J. B.; de Mello, A. J.; Kazarian, S. G. Chemical imaging of microfluidic flows using ATR-FTIR spectroscopy. *Lab Chip* **2009**, *9*, 2909-2913.
- (113) Greener, J.; Abbasi, B.; Kumacheva, E. Attenuated total reflection Fourier transform infrared spectroscopy for on-chip monitoring of solute concentrations. *Lab Chip* **2010**, *10*, 1561-1566.
- (114) Greener, J.; Tumarkin, E.; Debono, M.; Kwan, C. H.; Abolhasani, M.; Guenther, A.; Kumacheva, E. Development and applications of a microfluidic reactor with multiple analytical probes. *Analyst* **2012**, *137*, 444-450.
- (115) Kaun, N.; Kulka, S.; Frank, J.; Schade, U.; Vellekoop, M. J.; Harasek, M.; Lendl, B. Towards biochemical reaction monitoring using FT-IR synchrotron radiation. *Analyst* **2006**, *131*, 489-494.
- (116) Yao, S.; Bakajin, O. Improvements in Mixing Time and Mixing Uniformity in Devices Designed for Studies of Protein Folding Kinetics. *Anal. Chem.* **2007**, *79*, 5753-5759.

- (117) Cai, D. K.; Neyer, A.; Kuckuk, R.; Heise, H. M. Optical absorption in transparent PDMS materials applied for multimode waveguides fabrication. *Opt. Mater.* **2008**, *30*, 1157-1161.
- (118) Mata, A.; Fleischman, A.; Roy, S. Characterization of Polydimethylsiloxane (PDMS) Properties for Biomedical Micro/Nanosystems. *Biomed. Microdevices* **2005**, *7*, 281-293.
- (119) Nanoport Assemblies. <https://www.idex-hs.com/fluidic-connections/connectors-1/nanoport-assemblies.html> (accessed January 21 2016).
- (120) Bernath, P. F. The spectroscopy of water vapour: Experiment, theory and applications. *PCCP* **2002**, *4*, 1501-1509.
- (121) Nakanishi, K.; Hashimoto, A.; Pan, T.; Kanou, M.; Kameoka, T. Mid-infrared Spectroscopic Measurement of Ionic Dissociative Materials in the Metabolic Pathway. *Appl. Spectrosc.* **2003**, *57*, 1510-1516.
- (122) Lanucara, F.; Crestoni, M. E.; Chiavarino, B.; Fornarini, S.; Hernandez, O.; Scuderi, D.; Maitre, P. Infrared spectroscopy of nucleotides in the gas phase 2. The protonated cyclic 3[prime or minute],5[prime or minute]-adenosine monophosphate. *RSC Advances* **2013**, *3*, 12711-12720.
- (123) Ryding, M.; Andersson, P.; Zatula, A.; Uggerud, E. Proton mobility in water clusters. *Eur. J. Mass Spectrom.* **2012**, *18*, 215-222.
- (124) Jones, J. R.; Rowlands, D. L. G.; Monk, C. B. Diffusion coefficient of water in water and in some alkaline earth chloride solutions at 25[degree]C. *T. Faraday Soc.* **1965**, *61*, 1384-1388.

(125) Fierke, C. A.; Johnson, K. A.; Benkovic, S. J. Construction and evaluation of the kinetic scheme associated with dihydrofolate reductase from *Escherichia coli*.

Biochemistry **1987**, *26*, 4085-4092.

(126) Hoeltzli, S. D.; Frieden, C. Real-Time Refolding Studies of 6-19F-Tryptophan Labeled *Escherichia coli* Dihydrofolate Reductase Using Stopped-Flow NMR Spectroscopy†. *Biochemistry* **1996**, *35*, 16843-16851.

(127) Loveridge, E. J.; Allemann, R. K. Effect of pH on Hydride Transfer by *Escherichia coli* Dihydrofolate Reductase. *ChemBioChem* **2011**, *12*, 1258-1262.

(128) Callender, R.; Dyer, R. B. Probing protein dynamics using temperature jump relaxation spectroscopy. *Current Opinion in Structural Biology* **2002**, *12*, 628-633.

(129) Ke, S.; Ho, M.-C.; Zhadin, N.; Deng, H.; Callender, R. Investigation of Catalytic Loop Structure, Dynamics, and Function Relationship of *Yersinia* Protein Tyrosine Phosphatase by Temperature-Jump Relaxation Spectroscopy and X-ray Structural Determination. *J. Phys. Chem. B* **2012**, *116*, 6166-6176.

(130) Reddish, M. J.; Vaughn, M. B.; Fu, R.; Dyer, R. B. Ligand-Dependent Conformational Dynamics of Dihydrofolate Reductase. *Biochemistry* **2016**.

(131) Gibson, Q. H. Stopped-flow apparatus for the study of rapid reactions. *Farad. Discuss.* **1954**, *17*, 137-139.

(132) *Protein-Ligand Interactions*; Humana Press, 2005.

(133) *Technical Datasheet: SX20 Stopped-Flow Spectrometer*; 2016.

(134) Callender, R.; Dyer, R. B. Advances in Time-Resolved Approaches To Characterize the Dynamical Nature of Enzymatic Catalysis. *Chem. Rev.* **2006**, *106*, 3031-3042.

- (135) Boehr, D. D.; McElheny, D.; Dyson, H. J.; Wright, P. E. The Dynamic Energy Landscape of Dihydrofolate Reductase Catalysis. *Science* **2006**, *313*, 1638-1642.
- (136) Liu, H.; Warshel, A. The Catalytic Effect of Dihydrofolate Reductase and Its Mutants Is Determined by Reorganization Energies†. *Biochemistry* **2007**, *46*, 6011-6025.
- (137) Sawaya, M. R.; Kraut, J. Loop and Subdomain Movements in the Mechanism of Escherichia coli Dihydrofolate Reductase: Crystallographic Evidence†,‡. *Biochemistry* **1997**, *36*, 586-603.
- (138) Thielges, M. C.; Case, D. A.; Romesberg, F. E. Carbon–Deuterium Bonds as Probes of Dihydrofolate Reductase. *JACS* **2008**, *130*, 6597-6603.
- (139) Sikorski, R. S.; Wang, L.; Markham, K. A.; Rajagopalan, P. T. R.; Benkovic, S. J.; Kohen, A. Tunneling and Coupled Motion in the Escherichia coli Dihydrofolate Reductase Catalysis. *JACS* **2004**, *126*, 4778-4779.
- (140) Thorpe, I. F.; Brooks, C. L. Conformational Substates Modulate Hydride Transfer in Dihydrofolate Reductase. *JACS* **2005**, *127*, 12997-13006.
- (141) Iwakura, M.; Maki, K.; Takahashi, H.; Takenawa, T.; Yokota, A.; Katayanagi, K.; Kamiyama, T.; Gekko, K. Evolutional Design of a Hyperactive Cysteine- and Methionine-free Mutant of Escherichia coli Dihydrofolate Reductase. *J. Biol. Chem.* **2006**, *281*, 13234-13246.
- (142) Murakami, C.; Ohmae, E.; Tate, S.-i.; Gekko, K.; Nakasone, K.; Kato, C. Cloning and characterization of dihydrofolate reductases from deep-sea bacteria. *J. Biochem.* **2010**, *147*, 591-599.

- (143) Swanwick, Richard S.; Maglia, G.; Tey, L.-h.; Allemann, Rudolf K. Coupling of protein motions and hydrogen transfer during catalysis by *Escherichia coli* dihydrofolate reductase. *Biochem. J* **2006**, *394*, 259-265.
- (144) Kim, H. S.; Damo, S. M.; Lee, S.-Y.; Wemmer, D.; Klinman, J. P. Structure and Hydride Transfer Mechanism of a Moderate Thermophilic Dihydrofolate Reductase from *Bacillus stearothermophilus* and Comparison to Its Mesophilic and Hyperthermophilic Homologues. *Biochemistry* **2005**, *44*, 11428-11439.
- (145) Wong, K. F.; Watney, J. B.; Hammes-Schiffer, S. Analysis of Electrostatics and Correlated Motions for Hydride Transfer in Dihydrofolate Reductase. *J. Phys. Chem. B* **2004**, *108*, 12231-12241.
- (146) Luk, L. Y. P.; Loveridge, E. J.; Allemann, R. K. Protein motions and dynamic effects in enzyme catalysis. *PCCP* **2015**, *17*, 30817-30827.
- (147) Loveridge, E. J.; Behiry, E. M.; Guo, J.; Allemann, R. K. Evidence that a 'dynamic knockout' in *Escherichia coli* dihydrofolate reductase does not affect the chemical step of catalysis. *Nat Chem* **2012**, *4*, 292-297.
- (148) Dametto, M.; Antoniou, D.; Schwartz, S. D. Barrier crossing in dihydrofolate reductase does not involve a rate-promoting vibration. *Mol. Phys.* **2012**, *110*, 531-536.
- (149) Fenwick, R. B.; van den Bedem, H.; Fraser, J. S.; Wright, P. E. Integrated description of protein dynamics from room-temperature X-ray crystallography and NMR. *Proc. Natl. Acad. Sci. U.S.A.* **2014**, *111*, E445-E454.
- (150) Nashine, V. C.; Hammes-Schiffer, S.; Benkovic, S. J. Coupled motions in enzyme catalysis. *Curr. Opin. Chem. Biol.* **2010**, *14*, 644-651.

- (151) Ruiz-Pernia, J. J.; Luk, L. Y. P.; García-Meseguer, R.; Martí, S.; Loveridge, E. J.; Tuñón, I.; Moliner, V.; Allemann, R. K. Increased Dynamic Effects in a Catalytically Compromised Variant of Escherichia coli Dihydrofolate Reductase. *JACS* **2013**, *135*, 18689-18696.
- (152) Singh, P.; Sen, A.; Francis, K.; Kohen, A. Extension and Limits of the Network of Coupled Motions Correlated to Hydride Transfer in Dihydrofolate Reductase. *JACS* **2014**.
- (153) Rajagopalan, P. T. R.; Zhang, Z.; McCourt, L.; Dwyer, M.; Benkovic, S. J.; Hammes, G. G. Interaction of dihydrofolate reductase with methotrexate: Ensemble and single-molecule kinetics. *Proc. Natl. Acad. Sci. U.S.A.* **2002**, *99*, 13481-13486.
- (154) Bhabha, G.; Lee, J.; Ekiert, D. C.; Gam, J.; Wilson, I. A.; Dyson, H. J.; Benkovic, S. J.; Wright, P. E. A Dynamic Knockout Reveals That Conformational Fluctuations Influence the Chemical Step of Enzyme Catalysis. *Science* **2011**, *332*, 234-238.
- (155) Antikainen, N. M.; Smiley, R. D.; Benkovic, S. J.; Hammes, G. G. Conformation Coupled Enzyme Catalysis: Single-Molecule and Transient Kinetics Investigation of Dihydrofolate Reductase. *Biochemistry* **2005**, *44*, 16835-16843.
- (156) Chen, S.; Fahmi, N. E.; Wang, L.; Bhattacharya, C.; Benkovic, S. J.; Hecht, S. M. Detection of Dihydrofolate Reductase Conformational Change by FRET Using Two Fluorescent Amino Acids. *JACS* **2013**, *135*, 12924-12927.
- (157) Chen, S.; Wang, L.; Fahmi, N. E.; Benkovic, S. J.; Hecht, S. M. Two Pyrenylalanines in Dihydrofolate Reductase Form an Excimer Enabling the Study of Protein Dynamics. *JACS* **2012**, *134*, 18883-18885.

(158) Liu, C. T.; Layfield, J. P.; Stewart, R. J.; French, J. B.; Hanoian, P.; Asbury, J. B.; Hammes-Schiffer, S.; Benkovic, S. J. Probing the Electrostatics of Active Site Microenvironments along the Catalytic Cycle for Escherichia coli Dihydrofolate Reductase. *JACS* **2014**, *136*, 10349-10360.